Investigation of Failure Behaviour of a Glass-Fibre Reinforced Thermoplastic Composite

Jiaai Liang

December 2017

A thesis submitted for the degree of Master of Philosophy of

The Australian National University

Declaration

This thesis is an account of research undertaken between May 2015 and December 2017 at The Research School of Engineering, College of Engineering and Computer Science, Australian National University, Canberra, Australia.

Except where acknowledged in the customary manner, the material presented in this thesis is, to the best of my knowledge, original and has not been submitted in whole or part for a degree in any university.

Jiaai Liang

December 2017

Publications

1. J. Liang and S. Kalyanasundaram, "Failure behavior of a glass-fiber reinforced thermoplastic composite," in *AIP Conference Proceedings*, 2017

2. J. Liang and S. Kalyanasundaram, "Effect of fiber orientation on the failure behavior of a glass-fiber reinforced thermoplastic composite," in *AIP Conference Proceedings*, 2017

3. S. Kalyanasundaram, N.A. Zanjani, J. Liang, D. Rahiminejad and W. Wang, "Failure Behavior of Thermoplastic Composites," in *9th Australian Congress on Applied Mechanics (ACAM 9)*, Sydney, 2017

4. J. Liang and S. Kalyanasundaram, "Failure analysis of a woven glass-fibre reinforced thermoplastic composite," *Composites Science and Technology*, in preparation for submission

5. J. Liang and S. Kalyanasundaram, "Finite Element Analysis of failure analysis of a woven glass-fibre reinforced thermoplastic composite," *Journal of Reinforced Plastics and Composites*, in preparation for submission

Acknowledgements

Firstly, I would like to thank A/Prof. Shankar Kalyanasundaram, chair of my superviser panel, for the guidance throughout my research. I would also like to thank my advisers, Dr. Adrain Lowe and Prof. Qinghua Qin for their support in providing the relevant equipment.

I would also like to thank the Australian Government for the Australian Government Research Training Program Fee Offset Scholarship.

This project would not have been successful without the help, knowledge and advice from my colleges, Wentian Wang, Nima Akhavan Zanjani, Jae, Davood and Lu Chen. I want to thank them for helping me get familiar with this project, especially regarding the use of the software and the equipment.

I also want to thank my mother (Xianghong Chen) for her support throughout my study. I want to thank her for making the tough decision to send me far away from her and always encouraging me during every tough moment.

Finally, I want to thank my partner Hanchi Chen, for always being there and listening to my troubles.

Abstract

This work focuses on the fibre dominated failure of the woven thermoplastic fibre-reinforced composite. The novel experimental methodology induced failures in different deformation modes for the Glass Fibre Reinforced Polypropylene (GFRP) composite studied. Hence the path dependency effect on the failure of this material system can be studied experimentally through the three-dimensional (3D) Digital Image Correlation (DIC) system. A novel failure metric based on the strains experienced by the fibre bundles is developed. From the experimental results, this failure metric is found to be able to eliminate path dependency effect and is independent of fibre orientations. In Finite Element Analysis (FEA), this failure metric is incorporated with the simulations as a virtual tool to predict failures of the GFRP material.

From the experimental results, failure envelopes with the failure metric based on the principal strain and fibre strain are developed respectively. Both failure envelopes are implemented in the FEA simulation. The simulations incorporated with the failure metric in principal strain cannot accurately predict failure for the GFRP material system. The simulations incorporated with the failure metric in fibre strain, on the contrary, are found to be able to provide predictions that have a better agreement with the experimental results.

Table of Contents

List of Figures

List of Tables

Glossary of Terms

GFRP	Glass-Fibre Reinforced Polypropylene
3D	Three-dimensional
DIC	Digital Image Correlation
FEA	Finite Element Analysis
CO_2	Carbon Dioxide
WWFE	World Wide Failure Exercise
2D	Two-dimensional
UD	Unidirectional
NCF	Non-Crimp Fabrics
PA6	Polyamide 6
SEM	Scanning Electron Microscope
PPS	Polyphenylene Sulfide
GF	Glass Fibre
PEI	Polyetherimide
PP	Polypropylene
Tg	Glass Transition Temperature
AE	Acoustic Emission

FLC	Forming Limit Curve
PEEK	Polyetheretherketone
VOC	Volatile Organic Compounds
NCI	National Computational Infrastructure
E	Modulus
v	Poisson's ratio
σ	Stress
τ	Shear Stress
ρ	Density
β	Strain Ratio
ε_1	Major Principal Strain
ε_2	Minor Principal Strain
ε_x	Strain along the x direction
ε_y	Strain along the y direction
$\Delta\varepsilon_x$	Incremental strain along the x direction
$\Delta\varepsilon_y$	Incremental strain along the y direction
ε_{fibre}	Amount of strain acting on the fibres

Chapter 1 Introduction

1.1 BACKGROUND

Historically, the main application of advanced fibre reinforced composites has been in the aerospace industry. This need was driven by high strength and light weight requirements. Currently, fibre reinforced composite materials are widely used in various industries, including transport, construction, electronic and sports/leisure industries. In the early stages of the usage of composite materials, the matrix material was based on thermoset polymers, typically epoxy. Recently, fibre reinforced composites based on thermoplastic matrix are increasingly used in various industries [1]. The Lucintel market research [2] predicts that the global thermoplastic composites market will be worth approximately $16.4 billion by 2021 with a compound annual growth rate of 4.8% from 2016 to 2021. The rise in the usage of thermoplastic composite is mainly attributed to the advanced processing techniques, which enabled high volume production and lower cost in finished components.

Thermoplastic fibre-reinforced composites have the potential to be used in a wide range of applications. In the construction industry, they can be used in window and door frames, cladding, ducting and roof constructions [3]. In the automotive industry, their typical applications include door and head liners, interior panels, shelves and tyre covers. In the sports and leisure sector, thermoplastic composite can be manufactured to hockey sticks, boat paddle and horse saddles [4]. Among all the applications, the largest sector is transportation, which includes automobile and aerospace industries. As an example, this sector consumes more than 30% of the total production of carbon fibre

composites and generates more than 50% of carbon fibre revenue globally [1]. The main market driver in the automotive sector is the regulations in carbon dioxide (CO_2) emission, which requires lightweight construction solutions [5-8].

In the aerospace industry, thermoplastic fibre-reinforced composites are increasingly used in high-performance applications. The Airbus A340-600 and A380, which entered into service in 2002 and 2007 respectively, utilized some of the largest structural thermoplastic components on the market [9]. These thermoplastic components include thermoplastic skins reinforced with welded ribs, angle brackets and panels. The usage of these thermoplastic components results in weight savings between 20% and 50%, compared to their aluminium and titanium alternatives. Thermoplastic floor panel has become the trend in business jets and military aircrafts. Gulfstream's G650 is an example of the airplanes using this floor panel [10]. This aircraft also features a first-of-its-kind welded thermoplastic composite rubber and elevator rail section, which weighed 10% lighter than the preceding thermoset based composite material system. In addition to the usage of structural components, thermoplastic composite also exhibit potential to be used in the aircraft interiors market. The usage of thermoplastic composites has increased by approximately 400 percent from 2005 to 2014 in the aerospace industry [9].

In some cases, extensive use of composite material only resulted in minimal reduction in total weight. According to the Boeing Company, the wings of Boeing 787 consists of up to 50% composite material by weight and 80% composite material by volume [11-13]. In this aircraft, 50% of the primary structure, including fuselage and wings, is

manufactured by fibre reinforced composites [12]. However, it is found that only 3 percent of weight reduction in the Boeing 787 is achieved with the use of composites [14]. The reason behind this phenomenon is the overdesign of the structure. The designers used an excessive amount of composite material to guarantee safety for the aircraft. This emphasizes the importance in developing a good understanding of failure of composite materials to effectively use this material system.

1.2 RESEARCH OBJECTIVES

Failures in composites occur at a number of length scales, from the microscopic, barely observable fibre-matrix debonding, to macroscopic matrix cracking and delamination. In fibre reinforced composites, strain concentration occurs in the matrix at the fibre-matrix interface due to different mechanical properties of fibre and matrix. For thermoset fibre-reinforced composite materials, this strain concentration can cause fibre-matrix debonding. Further loading leads to the development of matrix cracks. These matrix cracks are usually precursors to the catastrophic failure events, such as delamination [15]. On the contrary, thermoplastic composites have completely different failure mechanism. This difference in failure mechanism, compared to the thermoset fibre-reinforced composites, can be attributed to the high strain to failure property of the thermoplastic matrix. The failure behaviours of the thermoplastic fibre-reinforced composites are caused by matrix dominated failure, fibre dominated failure or interphase dominated failure.

The research objective of this thesis is to focus on the fibre dominated failure of the woven thermoplastic fibre-reinforced composite.

In this thesis, a novel experimental approach is used to obtain the failure of the Glass Fibre Reinforced Polypropylene (GFRP) composite. Different geometries with a range of sectional widths are employed to induce failures under different deformation modes. The history of deformation and strains experienced by the failed and unfailed regions are captured by a digital image correlation system. These experimental results are used for developing a failure model in the principal strain space. This failure model has been found to be inadequate for the woven thermoplastic fibre-reinforced material used in this study. A novel failure model based on fibre strain experienced during different deformation modes will be presented to account for path dependency in this work. Both failure models are implemented in the finite element model to provide a simulative tool for predicting failure of this class of material system.

1.3 THESIS STRUCTURE

Chapter 1 gives an introduction of the background and objective of this work. Chapter 2 reviews existing failure analysis in fibre reinforced composite materials. In this chapter, different failure mechanisms in thermoset and thermoplastic composites are elucidated with the focus on woven fibre-reinforced composite materials. Following the review, Chapter 3 describes the GFRP material and the methodology used in this study. Experimental designs are discussed, including the specimen design, experimental set-up and measurement system. Simulation parameters and modelling are also detailed. Chapter 4 presents all the results and discussion. From the experimental results, failure envelops are developed for the GFRP material. They are then implemented in the FEA simulation. Finally, Chapter 5 concludes this work and provides recommendations for future work.

Chapter 2 Literature Review

2.1 INTRODUCTION

This chapter reviews the failure analysis of fibre reinforced composite materials related to this study. First, failure analysis for thermoset composite is reviewed, including the well-known World Wide Failure Exercise. This is followed by the discussion of failure and damage progression of woven thermoset composites. Then failure analyses for thermoplastic composites are outlined. The focus of the review is mainly on woven structured thermoplastic composite. Methods used in studying the failure behaviour and factors influencing the failures of the thermoplastic composites are discussed. This includes discussions of several failure criterions along with their applicability and limitation.

2.2 THERMOSET FIBRE-REINFORCED COMPOSITE

Typically, failures in fibre-reinforced composite material systems can start in different constituents and at the interface between these constituents. For a unidirectional lamina, if a load is applied perpendicular to the fibre direction, strain concentration will arise at fibre matrix interface due to the difference in Young's moduli between the two constituents [16]. For epoxy, the most widely used thermoset matrix, strain to failure can vary from 1% to 6% [17]. Failures in the thermoset based lamina usually start from debonding between fibre and matrix. This event is followed by the occurrence of matrix crack in the composite material system. Figure 2.1 (a) illustrates debonding of fibre and matrix in a unidirectional lamina under transverse loading. Figure 2.1 (b) shows matrix crack in a composite material caused by coalescence of the fibre-matrix debondings.

When the loading direction is parallel to the fibre orientation, debonding will also occur at free fibre ends and will lead to matrix crack around the debonding locations [18]. In laminated thermoset composites, delamination is a common catastrophic failure event and generally has a precursor of matrix cracks [15].

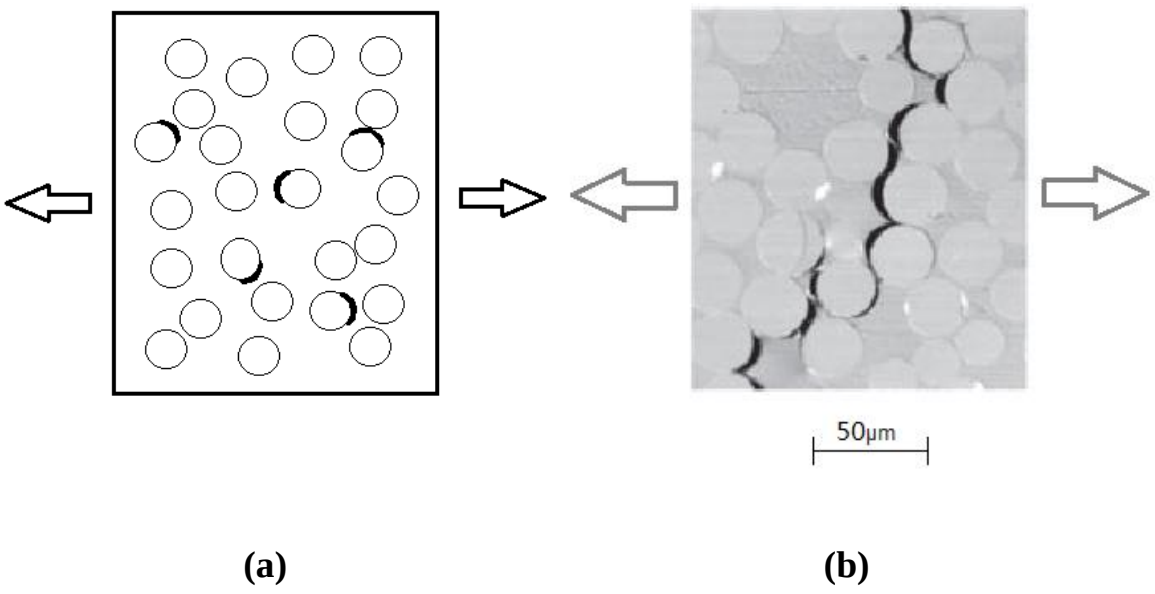

Figure 2.1 (a) Schematic of debonding between fibre and matrix in a unidirectional lamina; (b) Example of matrix crack caused by interface failure [19]

A number of failure theories have been proposed for thermoset composites. But none of them have been proved to be able to accurately predict failure for different materials and loading conditions [20]. There is also no agreement as to which theory works best.

2.2.1 Failure of Laminated Thermoset Composites

One of the earliest composite failure theories was proposed by Tsai and Wu [21]. They developed a failure criterion for anisotropic materials based on stress components. This failure theory can be expressed as a function of two strength tensors. In this theory, the interactions among stress components are independent from material properties, making it invariant from coordinate transformations. This failure theory also takes into account the difference in strength due to positive and negative stresses, but it cannot distinguish failure events in different constituents such as fibre failure, matrix failure and interface failure.

Hashin [22] developed a stress based failure criteria for unidirectional fibre composites for different failure modes. Four distinct failure modes were mathematically modelled based on the tensile and compressive behaviours of fibre and matrix. For each model, the failure criterion in terms of quadratic stress polynomials is established separately. Combining these failure criteria creates a piecewise smooth failure surface in stress space. This failure criteria was validated by comparing the prediction of failure and test data obtained from boron-epoxy off-axis specimens and glass/epoxy off-axis specimens [23, 24]. It was found that the failure surface provided a reasonable agreement with the test data for both material systems. This work highlighted the need for identifying the failure mode in developing a failure model.

To compare the maturity of the exiting failure theories, a study called ‘World Wide Failure Exercise’ (WWFE) was organized by Hinton, Soden and Kaddour. Currently, there are three exercises, WWFE-I, II and III. A series of articles were published

regarding the procedures and outcomes of the exercises [25-38]. The purpose of these exercises is to benchmark the status, accuracy and bounds of validity of the existing failure theories [28]. In each exercise, participants propose failure theories 'blindly' (without experimental data) and then their theories are compared with other participants' theories and experimental results provided by the organizers. From the second WWFE, participants are also offered opportunities to refine their theories after they receive the experimental results provided by the organizers [37]. The effects of these modifications are also studied and summarized at the end of the exercise by the organizers [32].

In WWFE-I (carried out between 1996 and 2004), 19 theoretical approaches were assessed for prediction of failure of polymer composite laminates under two-dimensional (2D) stress field [27]. It was found that only a few theories can give acceptable correlation with test data. The significance of the first WWFE is that it revealed the strengths and weaknesses of the existing failure theories and demonstrated the discrepancy between theoretical prediction and experimental results [29]. From this exercise, several areas that the first exercise did not consider were found. One of these areas is the behaviour of material under three-dimensional (3D) stress state. WWFE-II was conducted to address the issue in this area. Another overlooked area is damage development and initiation of delamination. This area is considered in the third WWFE. Other areas that all the three WWFE did not consider include woven structure and thermoplastic based composite materials.

The second WWFE was organized by Hinton and Kaddour and was conducted from 2007 to 2013. This exercise extended the assessment of failure theories from 2D to 3D state of stress. In this exercise, the performances of 12 failure theories were assessed based on the experimental results for 12 test cases, all involving 3D stress states. These test cases cover a range of materials, lay-ups and various 3D stress states [32]. The material systems employed in these test cases include isotropic polymeric matrix material, unidirectional (UD) fibre-reinforced lamina and multidirectional laminates. In Part A of this exercise, 'blind' predictions of the participated 12 theories were compared with the experimental results of the test cases. In Part B of this exercise, 75% of the predictions were modified with the available experimental results. These modifications were varied, including an entirely new theory and post recalibration of parameters. A good fit between the theoretical predictions and experiments were produced by these modifications, although doubts of the fidelity of these theories remained.

WWFE-III is currently under way and is organized by Kaddour, Hinton, Smith and Li. The focus of this exercise is to identify the degree of maturity of existing failure theories in damage development and ultimate failure. In this exercise, 12 failure theories were used to provide predictions of damage evolution and failure of 13 test cases [35]. The materials used in these test cases are all epoxy based composite materials. Compared to the first two exercises, the loading conditions in these test cases are extended to include stress concentration and thermal loading. In Part A of WWFE-III exercise, it was found that the participated failure theories varied in complexity, maturity and treatment of final failure. It was noted that four failure theories did not provide a clear definition of final failure of a laminate. For an isolated lamina under

combined shear and transverse loading, none of the failure models were able to predict the evolution of damage. In Part A of the failure exercise, no comparison between the theoretical predictions and the experimental results was carried out. In Part B of the exercise, this comparison will be carried out. The results of Part B have not yet been published.

From the current results of the three WWFE, several observations can be summarized [29, 35, 38]. First, most of the failure theories are based on the failure of a single layer and hence their accuracy drops dramatically in multilayered composite materials. Effects of ply thickness and lay-up sequence need to be studied, as well as interaction between cracks in differently oriented adjacent layers. Secondly, most existing failure theories did not consider the effects of unloading and reloading conditions. Another observation is that it is crucial to consider residual stresses created during the manufacturing of composite materials. Micromechanical analysis is also found to be critical in the prediction of composite failure. In addition to the above observations, it was also found important to integrate failure theories into finite element analysis and other forms of structural analysis. Further investigation is needed for other classes of composite materials that were not included in the WWFE, for example, woven composites and thermoplastic composites. Finally, it can be concluded that although some failure theories showed better predictions than others, none of the current theories examined in the WWFE are capable of accurate prediction of composite failure under complicated loading conditions.

Recently, Hart Smith highlighted the need for failure theories to distinguish between matrix dominated and fibre dominated failures [39, 40]. The main observation by Hart Smith was that most of the existing failure theories homogenise distinct fibre and matrix constituents into an 'equivalent' anisotropic solid [39]. This approach ignores the residual thermal stress developed in the matrix and leads to major inconsistencies in predicting matrix dominated failure. In Part 2 of this paper [40], detailed examples are given for non-catastrophic matrix failures preceding fibre failures. These examples indicate that the discrete fibre and matrix constituents contained in the fibre-polymer composites might not fail at the same time. These constituents have different failure mechanisms and should be treated separately.

Recently, Tsai and Melo [41] proposed a new failure theory using an invariant-based approach to describe properties and failure of composite plies and laminates. In this failure theory, the trace of the plane stress stiffness matrix, which is invariant from coordinate transformation, is used to describe the mechanical response of the composite material system. The trace of carbon/polymer composites is defined for a master ply, using the median values of ten different carbon fibre composite materials. Then multi-directional laminates are studied to generate the geometric factor. Based on the trace for the master ply and the geometric factor, failure envelope is established for each ply in the carbon/epoxy composites. By superimposing the failure envelopes of all plies, the minimum inner failure envelope can be found for a given laminate [42]. The advantage of the Omni strain failure envelope lies in its inclusion of many processing variables and defects. This failure envelope is also able to describe the failure of a laminate by considering a large number of fibre orientations.

In further development of this invariant-based approach [41], a strain normalized unit circle envelope is proposed for any carbon fibre reinforced polymer laminate [43]. This failure theory is inspired by the interactive Tsai-Wu theory and non-interactive maximum strain theory. Both theories use tensile failure strain and compressive failure strain as the fundamental building block. The new theory forms a more conservative failure envelope. The improvement of the unit circle failure theory is that it significantly reduces the number and complexity of tests required. From the longitudinal tensile and compressive failure tests of a single unidirectional ply, a failure envelope can be generated for the given laminate. This failure theory is beneficial for the industry, because it can save time and cost in characterizing material failures and provide more confidence in the material performance.

2.2.2 Failure of Textile Thermoset Composites

Compared to unidirectional (UD) cross-ply laminates, textile reinforced composites offer improved damage tolerance and is becoming an increasingly important class of high-performance materials [15]. Since the textile composites have the same local morphology as their UD cross-ply counterparts, their failure initiation and development have certain similarities. However, new patterns of failures are also found in the textile composites due to their distinct structural features.

A typical sequence of damage events in the cross-ply thermoset composites was also observed in a woven glass fibre reinforced thermoset laminate [44]. By correlating acoustic emission results and optical observations, failure initiation in a glass/epoxy woven laminate under tensile loading was determined. It was found that the increase of

loading led to development of transverse matrix cracks, followed by longitudinal crack and delamination. In the early stage of loading, transverse matrix cracks initiated inside the yarns and also at the boundaries of the yarns. Upon further load increase, the existing transverse matrix cracks grew and new transverse matrix cracks appeared. The saturation of transverse matrix cracks led to the development of longitudinal matrix cracks. Further increase of loading led to the development of new longitudinal matrix cracks and growth of the existing longitudinal matrix cracks. This was then followed by the occurrence of delaminations, growth of these delaminations and the ultimate failure. This mechanism of crack development in the woven composite material system is similar to its UD cross-ply counterparts.

For the natural fibre reinforced thermoset composites, fibres and matrix have similar mechanical stiffness. The ultimate failure can occur after the onset of matrix cracks and even before the occurrence of matrix cracks under bias loading (when the composite material is loaded at 45° to the fibre direction). These phenomena were observed in a woven flax/epoxy composite [45]. Due to the small difference of stiffness of flax fibre and epoxy matrix, strain concentration in the matrix at the fibre-matrix interface is low compared to other composite materials like glass- and carbon- reinforced thermoset composites. Therefore, fibre-matrix debonds and matrix cracks are no longer the precursors of failure. In these natural fibre reinforced composites, the damage process in flax fibres is an important feature in the ultimate failure of the material system.

A feature in the textile composite is the presence of yarns. The locations of transverse matrix cracks can be controlled by the architecture of the textile reinforcement. In a

woven structured composite, it is possible to observe fibre-matrix debonds on yarn boundaries earlier than debonds inside yarns. De Greef *et al*. [46] studied failure of a carbon fibre/epoxy composite and observed this phenomenon. From the quasi-static tensile loading tests and acoustic emission investigation, it was found that fibre-matrix debonds at the yarn boundaries occurred first in this composite material, but remained as individual debonds without developing into a large crack. The same phenomenon was observed in a carbon-epoxy 3D woven orthogonal non-crimp composite as well [47]. Fibre-matrix debonds at yarn boundaries can also be found under bias loading [48]. In the case of bias loading, damage development is similar to the process under longitudinal loading. It was found that the composite material system would exhibit fracture caused by high shear deformation in the matrix.

Yarn crimp is a special structure in textile composites and it has important influence on the damage initiation and development in the textile composites. This influence is mostly attributed to the complicated stress state the yarns experience locally due to the textile structure. Normally this complicated stress state has a non-negligible shear component introduced by the presence of the yarn crimp, even when the yarns are oriented at the same direction with loading [15]. A comparative study is performed on non-crimp 3D orthogonal weave and 2D plain weave glass/epoxy composites through tensile loading tests [49, 50]. The composite material systems examined in these studies have the same E-glass reinforcements and the same fibre volume fraction. The main difference between these two types of composite materials is the yarn crimp. The 2D composite is reinforced with four plies of conventional plain weave and has substantial crimps. The 3D orthogonal weave composites, on the other hand, have negligible crimp.

From the comparative study, it was found that the non-crimp 3D woven composites have considerably higher in-plane strengths and ultimate failure strains than their 2D laminated counterpart. When the composite materials were loaded in fibre direction, the 3D composites showed higher damage initiation threshold than the 2D weave composite. When the loading is in the 45° bias direction, however, the damage initiation threshold is lower in the 3D composites. In the 2D weave laminate with substantial crimps, the dominant failure was extensive delamination caused by transverse cracks. In the 3D non-crimp composites, the growth of transverse cracks was delayed and these transverse cracks were less prone to a yarn-matrix interfacial crack formation and propagation.

In the textile composites, the geometric characteristics of matrix cracks can also be affected by the yarn crimps. At early stage of loading, cracks can occur in different locations and the crack length is usually limited by the crimp intervals of yarns. With further loading, the cracks propagate with the structure of yarns and often lead to catastrophic failure events such as delamination. Ivanov *et al*. [51] studied crack development in a triaxial braided carbon-epoxy. This braided composite has high crimp and intensive interlacing of yarns. It was found that matrix cracks occurred in multiple locations, but were confined inside unit cells of the textile composite in the early stage of loading. For a glass/epoxy composite with fewer interlacing of yarns, cracks initiated at different locations and were confined in the unit cell as well, but propagated quickly through the specimen width and caused the entire failure of the composite material system [44]. The matrix cracks can also initiate at different locations over a yarn based on the textile structure with different yarn interactions [52-54]. In general, yarn crimp in

a composite material system affects stress distribution in different positions around yarns, and hence creates different types of failures in the composite material system.

Some textile composites have through-the-thickness reinforcements and these reinforcements play an important role in the composite failure. In Non-Crimp Fabrics (NCF) composites, individual plies are kept together by stitching yarns. Koissin *et al*. [55] studied the influence of stitching on NCF composites composed of carbon fibre and epoxy resin. This influence was analysed by comparison of structurally stitched NCF laminates and the unstitched ones through tests including loading conditions of in-plane tension, out-plane compression and 3-point bending. Results of these tests indicate that the structural stitching creates fibre-free zones, which can be called ‘openings’, on the surface of the stitched composite. It was found that these ‘openings’ had negligible influence on the stiffness, but they created stress/strain concentrations which led to earlier damage initiation. Although the damages were triggered at an earlier stage, it was found that stitching can significantly reduce the inter-ply delamination and increase the ultimate tensile load.

2.3 THERMOPLASTIC COMPOSITE

Thermoplastic composites are gaining increasing attention as advanced materials in high-performance applications [56, 57]. This class of material systems provides the advantages of lower costs in production and service. Compared to thermoset fibre-reinforced composites, thermoplastic composites can also offer longer shelf life, better impact resistance and recyclability.

The current fibre-reinforced composite applications are still dominated by thermoset fibre-reinforced materials due to their thermal stability and comparatively mature processing technology. To effectively use the thermoplastic composites, it is crucial to understand their failure behaviour for the safe operation of products made by using these materials. Failures in thermoplastic composites can be quite different from the thermoset composites due to their distinct mechanical properties of the polymer matrix. Compared to thermoset matrix, thermoplastic materials usually have much larger strain to failure [56]. In thermoset composites, the main precursor to failure is the development of matrix cracks. But in thermoplastic composites, due to the high strain to failure of the matrix component, matrix cracks are generally not the precursors to failure.

2.3.1 Failure Analysis of Thermoplastic Composites

Ma *et al*. [58] studied the failure behaviour of unidirectional fibre reinforced thermosetting and thermoplastic composites. The thermoset and thermoplastic based composite materials studied are UD carbon fibre reinforced epoxy resin and polyamide 6 (PA6) laminates respectively. The failure behaviour of these two material systems was investigated through tensile tests. From the experimental results and Scanning Electron Microscope (SEM) observation, it was found that the thermoplastic laminate had weak interface between fibre and matrix and failed mainly due to interfacial fracture caused by adhesive failure. On the other hand, the thermoset laminate had stronger bonding between fibre and matrix and exhibited splitting failure (splitting between fibres and layers) caused by matrix fracture.

The technique of Acoustic Emission (AE) can be used in studying failure behaviour of thermoplastic composite materials. Albouy and Vieille [59] used this technique as well as microscopic examination to determine the failure behaviour of the woven carbon-fibre reinforced Polyphenylene Sulfide (PPS) laminates. Gradual load and unload tensile tests were performed on the [±45°] carbon/PPS laminates at a temperature higher than the glass transition temperature of PPS. The purpose of these tests was to study the damage propagation and failure behaviour of this material system under severe environmental conditions. By matching the AE events and microscopic observation, it was found that the failure of this material system is dominated by the highly ductile behaviour of matrix. At early stage of loading, the rotation of warp or weft fibres occurred and led to cracks at the crimps of these rotations. With further loading, splitting between fibre bundles appeared on free surface, followed by the onset of intralaminar cracking. It was found that the initiation of delamination was delayed by the local plastic deformation in matrix-rich areas.

Hou and Friedrich [60] designed a hemispherical mould (punch and die) and employed it in the stamp forming tests of a glass fibre reinforced thermoplastic composite. The material system used in this study is laminate made from continuous glass fibre (GF) reinforced polyetherimide (PEI). The effects of different parameters in stamp forming were studied, including stamping temperature, velocity and hold-down pressure. Die geometries and laminate dimensions were also found to have influence on the material's formability. The major failures found in the material system are fibre buckling and ultimate fibre breakage. An instability phenomenon of 'shear-buckling' was also found in this material system. It refers to wrinkling of the material caused by intraply shear.

During forming, internal forces were generated in all directions. These internal loads can introduce stretching and shearing forces in the plane of the laminate and result in intraply shear within the laminate. When the cross-over angle between warp and weft fibre bundles reaches its limit, 'shear-buckling' occurs in the material system. This buckling can be prevented by applying a suitable hold-down pressure on the laminate. Finally, thickness distribution in the formed hemispherical parts was investigated and was found to be symmetric and dependent on the stamping pressure.

Lee *et al*. [61] performed stretch forming experiments on the composite materials with randomly orientated glass fibres and polypropylene matrix at temperatures ranging from 75°C to 150°C. Glass content in the tested material systems has weight fractions of 20%, 35% and 40% respectively. Strain distributions of these composite parts were recorded with grid method and used for obtaining strains at failure. Viscoelastic material models for these composite material systems were developed in the finite element analysis simulation under different temperatures. This simulation model can give predictions on the onset of failure (localized necking), based on Marciniak's imperfection theory. These prediction results were compared with the limiting strains obtained from the experiments. The trends of these limiting strain values were found to be in a good agreement between the simulation and experimental results. It was found that a discrepancy existed for the onset of localized necking between the simulation and experimental results. This discrepancy was attributed to the model's inability to simulate the materials' sensitivity to temperature, strain rate and strain ratio.

The effect of fibre orientation on the composite materials' formability and failure behaviour was studied for a woven self-reinforced composite [62]. Both uniaxial extension and stretch forming experiments were conducted on two sets of specimens with different fibre orientations. In each set of specimens, geometries with different aspect ratios were employed to induce different deformation modes. During the experiments, strain evolution information was captured by a Digital Image Correlation (DIC) strain measurement system. It was found that the specimens with different fibre orientations present different forming limits. For [0°/ 90°] specimens, the failure of the composite material studied can be predicted by the maximum strains found in uniaxial extension and biaxial stretch tests. The maximum strains were similar in these two tests. However, for [±45°] specimens, the maximum strains were different among specimens with different geometries. This indicates that strain limits can be different for different deformation modes. The dominant failure mechanism found in the [±45°] specimens was interlaminar shear between plies of the composite material. It was also found that the shear deformation significantly increased the formability of this self-reinforced polypropylene composite.

By comparing the forming behaviours of two pre-consolidated woven thermoplastic composites, it was found that the mechanical properties of the constituents play important roles in the material's failure behaviour [63]. The two material systems studied have the same polypropylene matrix and different fibres. One is self-reinforced, which means the fibres and matrix are both made of the same material. The other one is glass fibre reinforced polypropylene (PP) composite. By conducting the same forming experiments on these two material systems, different forming behaviours and failure

mechanisms were observed. The optical microscopy examinations revealed that the dominant failure in the glass/PP composite was fibre fracture while the failure morphologies in the self-reinforced composite were a complex combination of different failure mechanisms. In narrow specimens, the major deformation mode observed in both material systems was uniaxial extension. In wide specimens, it was found that the recordable areas of the self-reinforced specimen were experiencing biaxial stretching deformation mode. The glass fibre reinforced specimen, on the other hand, showed localized shearing deformation. These results indicate that the woven structure had more influence on the glass fibre reinforced polypropylene composite than the self-reinforced polypropylene composite.

Chemical treatment can influence composite materials' forming behaviour [64]. Wang *et al*. [65] studied the effect of chemical treatments on flax fibre reinforced thermoplastic composites. The material systems studied include polypropylene based composites reinforced with chopped random and continuous woven flax fibres. This work focused on various aqueous treatments including water treatment and cloudy ammonia treatment. Two sets of tensile tests were performed to examine the changes in the materials' mechanical properties caused by the aqueous treatments. One set of the test was performed on the specimens in wet conditions and the other set was performed on specimens that were completely dried after the aqueous treatments. From the experiments performed in wet conditions, it was found that both material systems exhibited a significantly increased elongation-to-failure when saturated with the aqueous treatments. This observation was attributed to a temporary plasticization effect in the interface region between fibre and matrix. From the experiments performed on

the dried specimens, it was found that the aqueous treatments reduced the material stiffness permanently for both material systems. This reduction in stiffness is less dominant for the continuous woven material system than the chopped random fibre material system. The major contribution of this study is that, for the flax fibre reinforced composites, aqueous treatments were found to be more effective than conventional preheating treatment for enhancing formability of this material system.

Temperature is also a common factor which can influence composite material's failure behaviour. Hufenbach *et al*. [66] studied the mechanical properties and failure behaviour of multi-axially reinforced textile composites under different thermomechanical loading conditions. The employed glass/PP composite material systems have different reinforcement structures including a 3D textile composite with weft-knitted reinforcement and a woven reinforcement structure. Uniaxial tension and compression tests were performed on the two material systems with temperatures ranging from -40°C to 80°C. From the experimental results, it was found that both material systems have temperature related mechanical properties and strengths. The shear properties and compressive strength are largely dependent on the temperature. The fibre dominated properties, such as tensile Young's modulus, are less influenced by the temperature. The Glass Transition Temperature (Tg) plays an important role on the temperature-dependent mechanical behaviours of both material systems. Below the glass transition temperature, the materials became brittle. An increase of the crack formation and a simultaneous decrease of the voids growth were observed. Above the glass transition temperature, the materials became ductile and less matrix cracks were found.

Izer *et al*. [67] studied the effect of processing variables on the failure behaviour of self-reinforced polypropylene composites by using the Acoustic Emission (AE) technique. The experimental sheets were produced by film-stacking method and were consolidated in the compression mould by applying a constant pressure to hold these sheets. Effect of different processing temperatures in the consolidation process is studied. During the tensile testing of the specimens, AE events were recorded to help assess the failure behaviour of these materials. It was found that consolidations at higher temperatures (20°C and 35°C higher than the matrix melting temperature) can enhance the adhesion between layers. For these specimens with good adhesion between layers, AE events were decreased and they occurred in the later stage of the experiments. Fibre breakage was found to be the dominant failure mechanism in these sheets consolidated at high temperatures. For the sheets consolidated at a lower temperature (5°C higher than the matrix melting temperature), a large number of AE events were observed and they were attributed to the debonding of the fibre-matrix interface, which includes both inter-laminar and intra-laminar interfaces.

2.3.2 Failure Theories for Thermoplastic Composites

Recently, a probabilistically based damage model was developed for textile reinforced thermoplastic composites [68]. Experimental and numerical studies were carried to test the validity of this model [69]. The approach for developing this model is based on continuum damage mechanics models where damage is defined as the degradation of material stiffness [70]. In a conventional UD laminate, the damage progression can be described by the progression of discrete damage events. Typically, this sequential damage event starts with the occurrence of matrix cracking, which can be quantified by

the crack density measurement. This is followed by delaminations, which can be quantified by the delamination length or the delamination area. In composites with woven or braided reinforcement, different damage mechanisms can happen simultaneously, making it impossible to separate and quantify all the different damage mechanisms. In order to deal with this complex damage phenomenon in the woven or braided reinforced composites, the probability approach is utilised to provide failure curves associated with failure probabilities. For the textile reinforced composites studied, the failure behaviours were characterised by different failure modes [71]. Then the interaction between these failure modes were represented by a summation of the particular probability functions. Thus, instead of one single failure envelope, different failure prediction curves associated with their failure probabilities form the theoretical failure probability plot to predict the damage of the textile reinforced composites. This model considers non-linear material behaviour and stiffness degradation associated with different damage models.

Bohm *et al*. [72] developed a phenomenologically based damage model to predict failures in the textile composite materials with woven or braided reinforcements. The validity of this model is tested for glass fibre reinforced woven thermoplastic composites. In the phenomenologically based model, damage is defined as the change of stiffness and the initiation of damage is defined by using a modified failure criterion developed by Baste [73] and Cuntze [74]. Criteria for the initiation of damage and the ultimate failure were established separately. By comparing the failure predictions with experimental data of glass/PP composites, this failure model was found valid under

certain loading conditions. This failure model can be implemented in numerical simulations as well.

In the work conducted by Zanjani *et al*. [75], a novel history/path dependent failure criterion was proposed for a woven thermoplastic composite. In this work, rectangular specimens with different aspect ratios (ratio of width to length) were formed to failure at room temperature. During the experiments, the surface strains on one side of the specimens were recorded by an in-situ 3D photogrammetric measurement system. By analysing the obtained principal strains, different deformation modes were found and this was attributed to specimen geometries with different aspect ratios. The proposed failure criterion is based on the Forming Limit Curve (FLC) method, which consists of both principal strains and is conventionally used for metals. For the self-reinforced thermoplastic composite employed in this study, the FLCs were defined separately for two regions. Region I was defined for deformation modes between uniaxial extension and biaxial extension. In this region, the major principal strain limit was found almost constant regardless of the minor principal strain. The second region was defined for shear deformation. A linear FLC with relatively higher strain limit in the pure shear region was developed. The path dependency of this failure criterion lies in that it defines failure limit in regards to different deformation modes. In this way, failure can be predicted by tracking strain evolution history.

Wang *et al*. [76] developed a new failure envelope for a flax fibre reinforced polypropylene composite. This failure theory is developed based on an understanding of the failure mechanism of the natural fibre composites. It was found that the dominant

failure in the flax fibre composite was fibre fracture [77]. A failure envelope was developed based on the strains experienced by the fibres. This approach tracked the evolution of fibre movement during loading and the fibre strain was obtained through strain transformation from global coordinate to fibre coordinates. Since this approach was developed for woven composite materials, fibres strains on both directions can be determined at any given point. The larger fibre strain in these two directions was used as the failure limit for the flax fibre in the proposed failure theory. In order to develop the new failure envelope for the flax fibre reinforced composites, hourglass shaped specimens were employed to induce failures in a wide range of deformation modes. During the experiments, strain evolution on the specimen surfaces was recorded during the loading history by a 3D DIC strain measurement system. Then the algorithm to calculate the fibre strain was implemented in this strain measurement system. From the experimental results of different hourglass shaped specimens, a new failure envelope was developed based on the fibre strain limit for different deformation modes. After implementing this failure envelope in the finite element analysis, it was found that the predicted failure initiation regions were in agreement with the experimental results.

2.4 SUMMARY

This chapter summarizes literatures related to the failure behaviour of fibre-reinforced polymer composites. Firstly, it reviews the development of failure theories for thermoset fibre-reinforced composites, including UD cross-ply and textile reinforced composites. The structural feature in the textile thermoset composites introduced different types of failure mechanisms in this class of material system. Then failure analyses for thermoplastic composites are reviewed with the focus on woven fibre-

reinforced composite materials. Compared with thermoset fibre-reinforced composites, different failure behaviours are found for the thermoplastic composites.

In conclusion, it can be stated that some of the failure models for the fibre-reinforced composites are developed in principal strain space. For the woven thermoplastic composite materials, there is a need for failure theory to distinguish between fibre-dominated failures and matrix-dominated failures. *The main focus of this work will be to develop a failure theory for a glass fibre reinforced woven thermoplastic composite that is dominated by fibre failures.*

Chapter 3 Material and Methodology

3.1 INTRODUCTION

This chapter discusses the material and methodology engaged in this study. Firstly, an introduction of the Glass Fibre Reinforced Polypropylene (GFRP) composite material studied is given, including its characteristics, manufacturing methods and its applications. Then the experimental plan for the specimens is detailed and the specimen preparations are discussed. Following the discussions of the specimens, experimental approach is introduced with the experimental set-up and the measurement system. Finally, simulation method using Finite Element Analysis (FEA) is elucidated.

3.2 GLASS-FIBRE REINFORCED POLYPROPYLENE COMPOSITE

The material studied in this research is a GFRP composite material (TWINTEX®). It is produced by Owens Corning Ltd. and is made of commingled E-glass and polypropylene filaments [78]. The E-glass fibre makes up 60% of the weight and 35% of the volume. The specimens are cut from the TWINTEX® sheets, which are sheets with 1mm thickness. In these TWINTEX® sheets, fibres are woven in a 2/2 twill pattern in orthogonal directions.

E-glass is a commonly used material as fibres due to its high strength and relatively low cost. In 2014, over 95% of the total volume of composites other than carbon fibre composite in Europe is reinforced with glass fibres [1]. Compared with carbon fibre, glass fibre has lower stiffness, but is less expensive.

Polypropylene (PP) is a common matrix material. It is widely used in various applications due to its ability to adapt to various fabrication techniques. PP has high strain to failure and is found to have an elongation at yield of up to 350% and an elongation to break as large as 900% [79-81]. PP has other advantages, such as good chemical resistance, long shelf life and high impact strength. PP has a relatively low melting temperature compared to other thermoplastic materials, such as polyetheretherketone (PEEK) and polyetherimide (PEI), making it easier to recycle. But this property of low melting temperature limits its usage in high temperature applications. In CNC machining process, PP starts to deform under the heat of the cutter, making it very difficult to obtain a smooth finished surface [82].

Based on the size of the products, possible manufacturing processes for TWINTEX® include vacuum moulding, diaphragm and calendaring forming [83]. The TWINTEX® sheet utilized in this study is produced by filament winding and consolidation processes [83]. During the winding process, E-glass filaments and polypropylene filaments are winded into commingled yarns, as shown in Figure 3.1 [84]. After the winding, the material is consolidated by heating above the melting temperature of polypropylene (PP), which is around 180°C. At the time of consolidation and also during cooling, a low pressure between 1 to 30 bars is applied. These processes have a fast cycle time. During these processes, there is no Volatile Organic Compounds (VOC) emission.

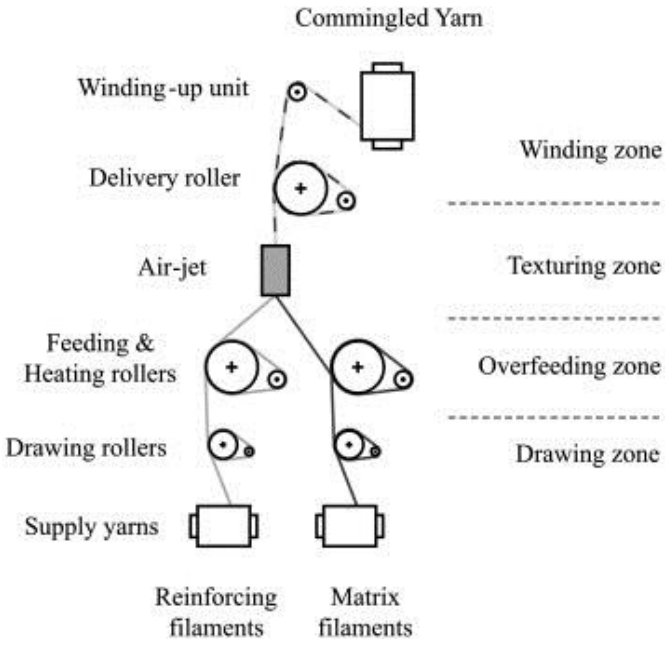

Figure 3.1 Schematic of filament winding process [84]

The TWINTEX® sheets are manufactured to have a woven structure with a 2/2 twill pattern, as shown in Figure 3.2 (b) [85]. Woven structure can prevent sudden occurrence of catastrophic failure by the undulation of fibres. It is common to find accumulated local damages before the final failure of this class of materials. There are different weave patterns used in the modern design. The most common weaves are plain weaves, twill weaves and satin weaves [86]. The plain weave pattern is easy to manufacture and can provide balanced properties in the fabric plane. Plain weave composites are suitable for flat applications where drape and conformability are not required. Twill weave has a pattern of diagonal parallel ribs and can be identified by looking at the presence of pronounced diagonal lines that run along the width of the fabric. It has higher resistance to tearing than a plain weave because it has fewer yarns interlacing per area, therefore a greater degree of internal mobility. The satin weaves are normally more flexible than

plain weaves or twill weaves. They are pliable and can be draped around curved surfaces.

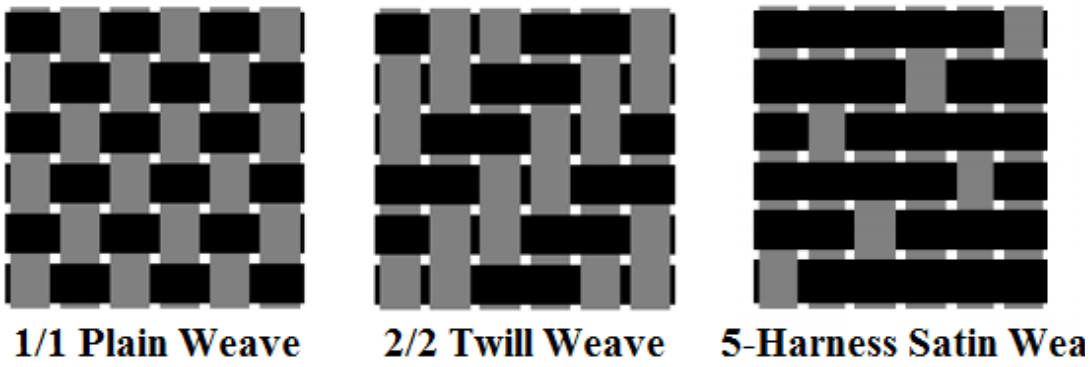

(a) **(b)** **(c)**

Figure 3.2 Common woven patterns [85]: (a) 1/1 Plain Weave; (b) 2/2 Twill Weave; (c) 5-Harness Satin Weave.

GFRP composite materials are used in a wide range of applications. They are mainly used for automotive, marine, sports/leisure and building/construction. One example of the GFRP application is for canoe body. In this application, this material allowed the boat builder to achieve a light weight, high stiffness, abrasive and impact resistant structure that was not subject to part shrinkage during processing [87].

3.3 SPECIMEN DESIGN AND PREPARATION

This section introduces the design of specimens, including geometries and fibre orientations. The preparation processes for the specimens are also discussed. There are two rounds of experiments conducted and the results are found to be similar to each other.

3.3.1 Specimen geometries

As shown in Figure 3.3, specimens were cut to hourglass shapes with different widths in the middle section. These hourglass shapes are widely used in conventional sheet metal forming, for the purpose of inducing different deformation modes to elucidate the failure of the material during forming. In metal sheet forming, the wide specimens, especially the full circular shaped specimen, normally experience biaxial stretch deformation. When the middle sectional width gets narrower, the deformation mode will change from biaxial stretching to deformation modes, such as uniaxial stretching and shear deformation. A schematic indicating the effect of the hourglass shapes on the deformation mode is shown in Figure 3.4. For the GFRP material system, it is found that the hourglass geometries can also help induce failures in different deformation modes. Since the material is orthotropic and the fibres are woven together, the induced deformation modes cover mostly between uniaxial tension and biaxial tension. The details of the deformation modes induced by the geometries for the GFRP material are discussed in Chapter 4.

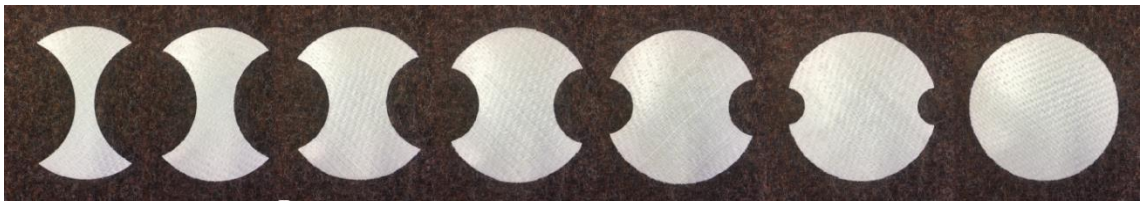

Figure 3.3 Hourglass shaped specimens and full circular specimen

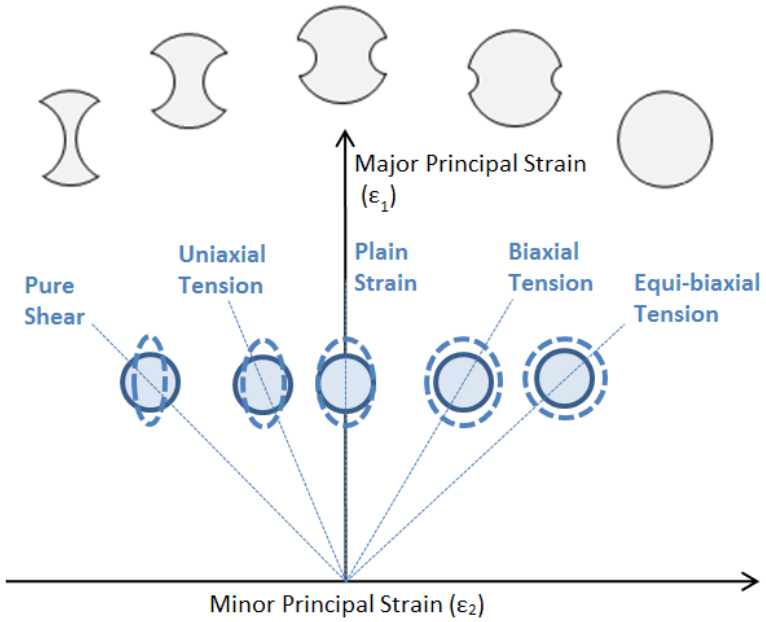

Figure 3.4 Schematic of the effect of the hourglass shapes on the deformation mode

The hourglass shapes are cut from a circle with a diameter of 200mm. The sectional widths in the middle have a range from 25mm to 150mm, with an interval of 25mm. This results in six different hourglass geometries and a total of seven geometries including the full circular one. The schematic of the specimen geometries is shown in Figure 3.5. Since the GFRP in this study is an orthotropic material, the orientation of the fibres should be considered in the specimen design. In this study, two types of fibre orientations are examined. One is the [0°/90°] orientation, which is called the fibre orientation. The other one is the [+45°/-45°] orientation and is named as the off-fibre orientation. The two fibre orientations are shown in Figure 3.6. Based on different shapes of the specimens and two fibre orientations, the naming of all the specimens are listed below in Table 3.1. Both the geometry and the fibre orientation of the specimens help induce failures in different deformation modes.

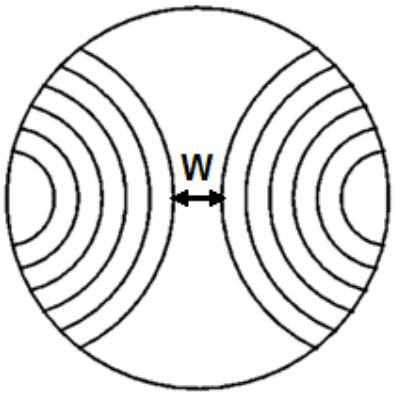

Figure 3.5 Schematic of specimen geometries

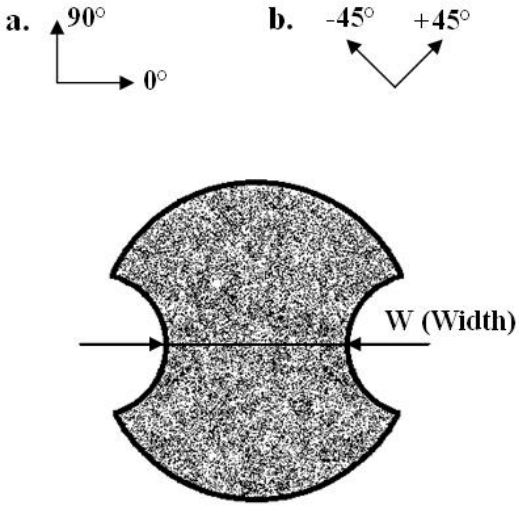

Figure 3.6 Schematic of a specimen with an hour-glass shape and a stochastic pattern (a. Fibre Orientation b. Off-fibre Orientation)

Table 3.1 Naming of specimens employed in the study

Sectional Width [mm]	25	50	75	100	125	150	200
Fibre Orientation	F25	F50	F75	F100	F125	F150	F200
Off-fibre Orientation	O25	O50	O75	O100	O125	O150	O200

3.3.2 Specimen Preparation

After the specimens were cut to the designed geometries, the GFRP specimens were prepared for the experiments. Firstly, they were cleaned with isopropanol solution, which is a common cleaning substance for polymers. Special tissues were used for the cleaning process to avoid leaving paper scrapes on the specimen surface. After the specimens were cleaned on both sides, they were put aside for at least 15 minutes for complete evaporation of chemicals.

When the surfaces of the specimens were cleaned and dried, tabs were glued onto the outer region of the specimens, as shown in Figure 3.7. This application of tabs is a special treatment to avoid failure at the edge of the specimen caused by the lock ring region. The details of the lock ring design are discussed in Section 3.4. The application of the lock ring design in the experiment introduces localized deformation around the edge of the specimens. This localized deformation could initiate failures at the edge of the specimen earlier than the failures in the desired (centre) region. After exploring possible solutions in the simulations, tabs were found to be an effective way to solve this problem. Since the specimen geometries are hourglass shapes, the corresponding curved tabs are applied. The tabs were cut from 0.4 mm thick steel sheets. They were cleaned using acetone and then glued to the specimen surface by using Lottie 406 superglue.

Figure 3.7 Specimen with tabs attached

After the above processes, paints were applied on one side of the specimens. The purpose of the painting process is to create a stochastic pattern on the specimen surface for calculation of strain information, which is required by the 3-dimensional Digital Image Correlation (DIC) system ARAMIS®. During painting, coverage by film was applied so that the painting only performed in the centre region which is recordable by the DIC system. This coverage method can also avoid contamination of the experimental equipment by the paints during the experiments. An example of the stochastic pattern can be found in Figure 3.6. In order to obtain this high contrast stochastic pattern, a base paint (prime) is required first; it can be either white paint or black paint. Since the TWINTEX® sheet is originally white in colour, the white paint was chosen for the prime. Then the black paint was applied after the prime is reasonably dried. It was carefully applied by half pressing the nozzle and spraying towards directions other than the specimen surface to create small painting drops fallen on the specimen. It should be noted that matt paints are used to avoid data loss caused by reflections during the experiments.

Finally, during the experiments, lubrication is required especially between the specimen and the punch. Teflon film and lubrication oil are used together on the specimen and the punch. By applying the lubrication, the failures can be pushed towards the centre of the specimens, creating failures in different deformation modes.

3.4 EXPERIMENTAL SETUP

The experiments conducted in this study utilized a press machine and the custom-built blank holder and die. The set-up of the experiment and a schematic of the custom-built blank holder and die are shown in Figure 3.8. The press machine has a cylindrical punch with a 100-mm diameter hemispherical end. The open die design of the press machine enables the punch to press the specimens to a maximum depth of 70mm. During the experiments, the specimen was deformed by the punch until failure occurred in the specimen. During this process, the custom-built blank holder and die held the rim of the specimen. This press machine is powered by hydraulic pressure. A computer is connected to the press machine to control the speed of the punch. The speed of the punch can vary between 10mm/s and 40mm/s. In the experiments conducted in this study, the speed of the punch is set at 20mm/s.

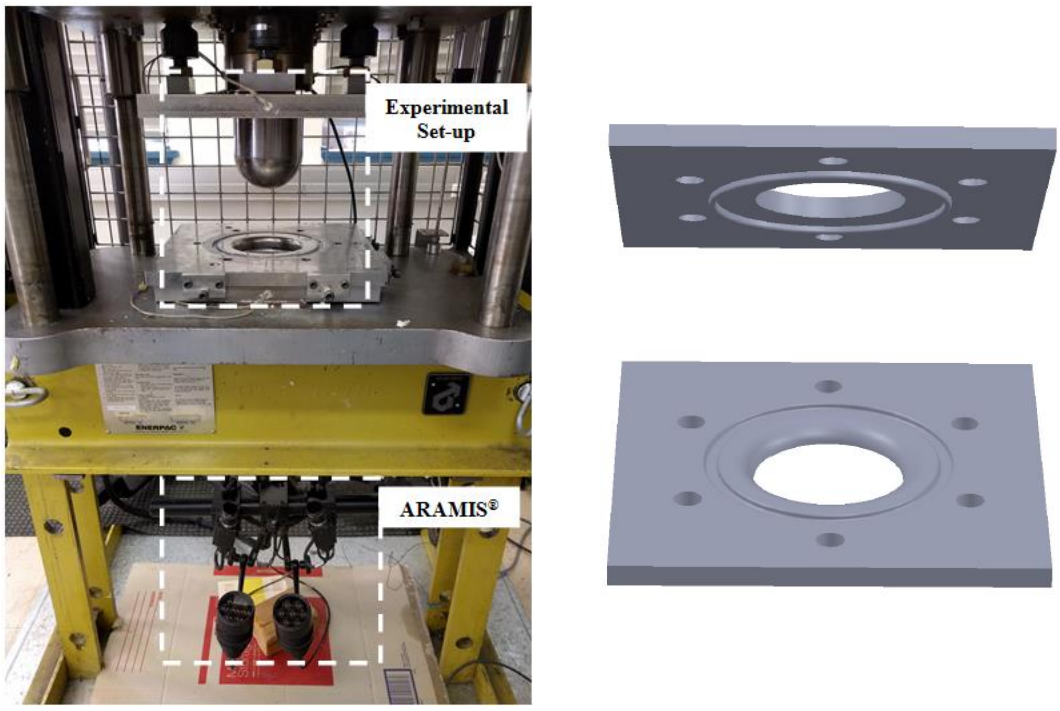

(a) (b)

Figure 3.8 (a) Set-up of the experiment and measurement system; (b) Custom-built blank holder and die

The custom-built blank holder and die utilized a special design called the lock ring design. This lock ring design includes a circular heave on the blank holder and a circular groove on the die. This heave and groove are matched and they clamp the specimen between them firmly by six symmetrically distributed screws applied on the blank holder and die. The geometries of the custom-built blank holder and the lock ring design are shown in Figure 3.9. The diameters of the opening in the press machine and the custom-built blank holder and die are 105mm. The diameter of the centre line of the lock ring is 165mm, which is 35mm smaller than the specimen diameter.

The groove on the die has a depth of 5mm and it is surrounded with fillets of 2mm radius. There are two sets of the custom-built blank holders with the same heave height of 5mm. The heave width for one blank holder is 5mm and for the other one is 6.8mm. The blank holder with the heave width of 5mm is for 2mm thick specimens and the other blank holder with the heave with of 6.8mm is for the 1mm thick specimens. For narrow specimens of F25 and O25, they can be fastened firmly in the lock ring without tabs. Hence the blank holder for 1mm thick specimen should be used in these two cases. For the other specimens, tabs should be attached onto the specimens on both sides to prevent localized failure at the lock ring region, so the blank holder for 2mm thick specimens should be used. The fastening between the custom-built blank holder and die is achieved by six M12 bolts placed symmetrically at the circle slightly larger than the specimen size. The applied torques range from 15kN·m to 60kN·m based on the specimen geometry, ensuring no slippage at the lock ring.

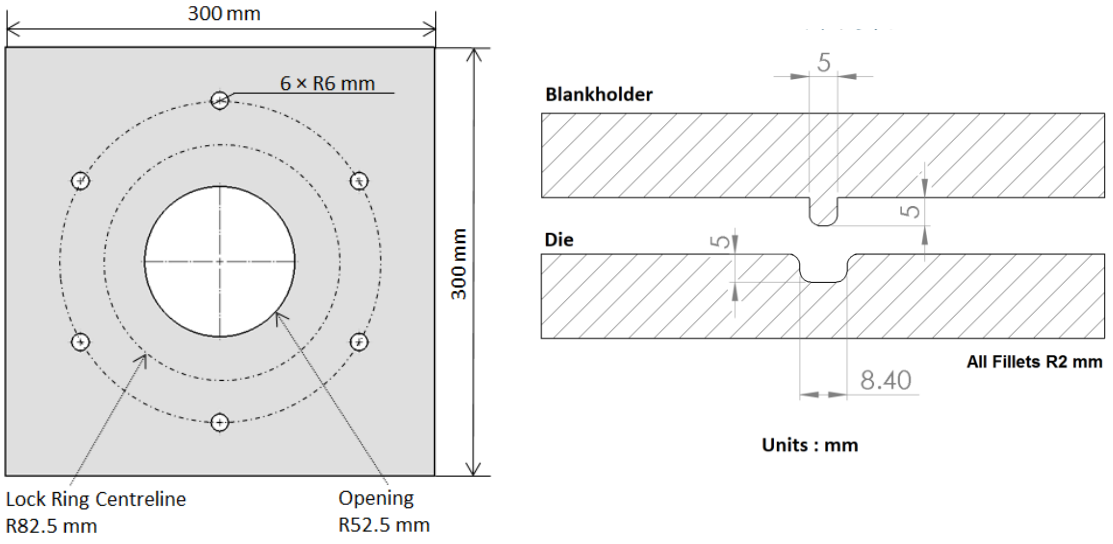

(a) (b)

Figure 3.9 (a) Schematic drawings of the custom-built blank holder; (b) Drawing of the lock ring design

3.5 STRAIN MEASUREMENT

During the experiment, the surface strain of the specimen is recorded by a 3D Digital Image Correlation (DIC) system named ARAMIS®. This DIC system is configured under the set-up of the experiment, as shown in Figure 3.10 [88]. With this configuration, the DIC system is able to capture the deformation of the lower surface of the specimen through the open die during the entire experiment. The two high-speed and high-resolution cameras take images of the specimen during the test. The surface strain information is then obtained by processing these images with photogrammetric techniques [89]. By correlating the two dimensional images provided by the two cameras at the same stage, the three dimensional strain contour can be obtained. The ARAMIS® DIC system provides many advantages over the conventional strain measurement methods and it is able to provide real-time and full-field information including displacement and strain fields.

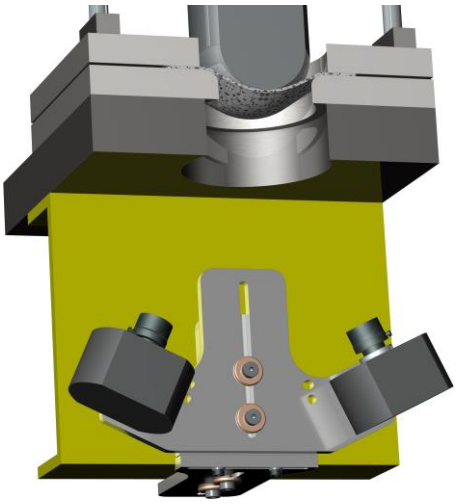

Figure 3.10 Schematic of the DIC system coupled with the experimental set-up [88]

The ARAMIS® system used in this study is model 5M, manufactured by GOM mbH. The configuration of the 3D sensor unit is shown in Figure 3.11 [90]. Based on different measuring distances, measuring areas (Length x Width) range from 10 x 8 mm^2 to 5000 x 4150 mm^2. The measuring height/depth varies and is normally equal to the measuring width. Since the recordable area through the open die is a circle of a diameter of 105mm and the forming depths of the specimens do not exceed 40mm, the measuring area of 175 x150 mm^2 is used for the experiments conducted in this work.

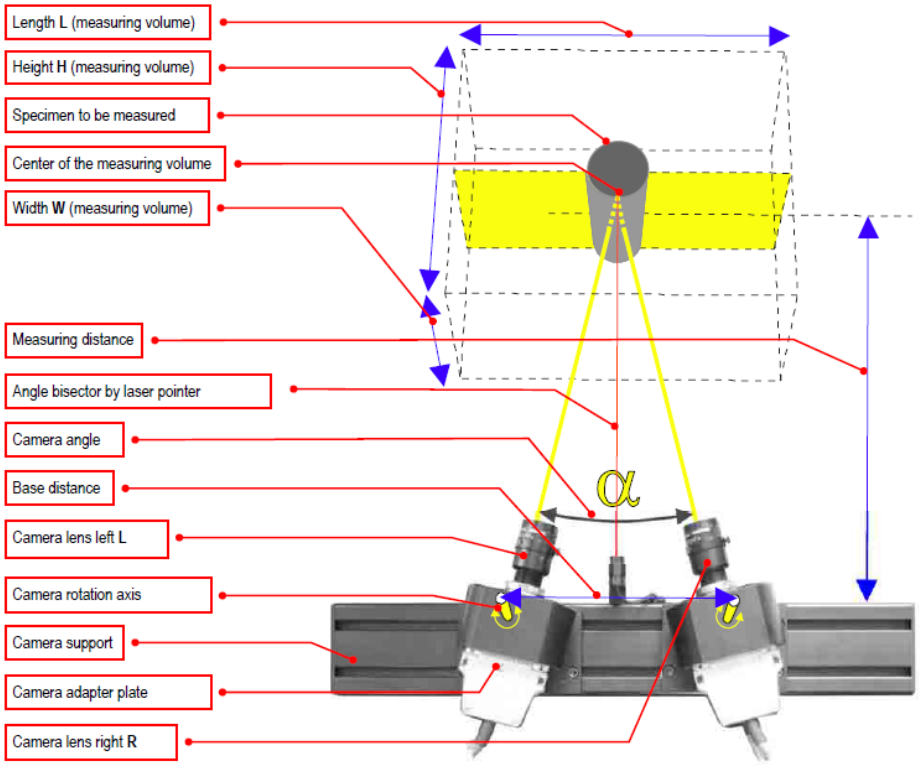

Figure 3.11 Configuration of ARAMIS® 3D Sensor Unit [90]

In the system of ARAMIS® 5M used in this study, high resolution images of 2448 x 2050 (pixels) are taken by both cameras at the same time. During the experiments, the maximum frame rate of 15 Hz was used, which means 15 images were taken per second. The shutter time can range from 0.0001s to 2s. During the experiments, the shutter time was adjusted for each trial based on the lighting conditions to avoid over exposure. The DIC system also has strain accuracy up to 0.01%. Specifications of the ARAMIS® 5M System are summarized in Table 3.2.

Table 3.2 Specifications of ARAMIS® 5M System

Parameter	Specifications
Measuring Area (Length x Width)	10 x 8 mm^2 up to 5000 x 4150 mm^2
Camera Resolution	2448 x 2050 pixels
Maximum Frame Rate	15 Hz
Shutter Time	0.0001s to 2s
Strain Range	0.01% up to >100%
Strain Accuracy	up to 0.01%

3.6 FINITE ELEMENT ANALYSIS

ABAQUS is one of the common FEA softwares and it is utilized in this study with the access provided by the supercomputing facilities at the National Computational Infrastructure (NCI) Australia. In this section, the analysis method is introduced first, followed by the details of the FEA model, including the boundary conditions, time steps and material modelling.

3.6.1 Analysis Method

In the systems of nonlinear problems, the commonly used integration methods are broadly characterized as explicit and implicit methods [91-93]. Explicit method is

conditionally stable and its stability limit is that the maximum time increment should be less than a critical value of the smallest transition time for an elastic wave to cross the smallest element dimension in the model. Implicit method, on the other hand, does not have this stability limit. It uses an automatic increment strategy based on the full Newton iterations [94]. In this thesis, the quasi-static nonlinear formulation is used and the implicit method is used to solve the nonlinear equations.

In implicit method, the discretised equilibrium equation [95] for the finite element model is:

$$P^N - I^N = M^{NM}\ddot{u}^M \qquad 3.6.1$$

where P^N is the external force vector; I^N is the internal force vector; M^{NM} is the mass matrix; and $\ddot{u}^M$ is the acceleration vector. $M^{NM}\ddot{\mu}^M$ is the force vector due to material inertia.

In static equilibrium, the d'Alembert forces are almost constant with time and hence the following equation can be obtained:

$$M^{NM}\ddot{u}^M \approx 0 \qquad 3.6.2$$

ABAQUS/Standard uses Newton's method to solve for static equilibrium. By applying the Taylor's series expansion, an estimated solution at iteration (i), $u^N_{(i)}$ is:

$$P^N - I^N + \left(\frac{\partial P^N}{\partial u^M} - \frac{\partial I^N}{\partial u^M}\right) c^M + \cdots = 0 \quad 3.6.3$$

This can be written as:

$$K^{NM} c^M = P^N - I^N \quad 3.6.4$$

where

$$K^{NM} = \frac{\partial I^N}{\partial u^M} - \frac{\partial P^N}{\partial u^M} \quad 3.6.5$$

is the system's tangent stiffness, or Jacobian matrix. The incremental displacements (Δu) are updates by:

$$\Delta u^N_{(i+1)} = \Delta u^N_i + c^N_i \quad 3.6.6$$

where $\Delta u^N_{(i+1)}$ is the incremental displacement at the increment of i+1; Δu^N_i is the incremental displacement at the increment of i; c^N_i is the correlation to the solution at the degree of freedom N at the increment of i.

3.6.2 FEA Model

The assembly of the FEA model simulating the set-up of the experiment is shown in Figure 3.12. The punch is modelled to have the same geometry as the punch in the press machine, which has a hemispherical end with a diameter of 100mm. The blank holder

and die are simulated to have the open geometry of 105mm diameter, but without the lock ring geometry. The effect of the lock ring design during the fastening process is simulated by applying boundary conditions in a separate step called pre-stretch step. The reason of applying boundary conditions instead of lock ring geometries to simulate the lock ring effect is to reduce simulation cost and avoid convergence issues. Since the boundary condition is applied to simulate the lock ring effect, the diameter of 165mm (the diameter of the centre line of the lock ring) is used for the specimen. The auxiliary tabs are not simulated in the FEA model because they would detach the specimen during the fastening process and their function is only to prevent failure in the lock ring region.

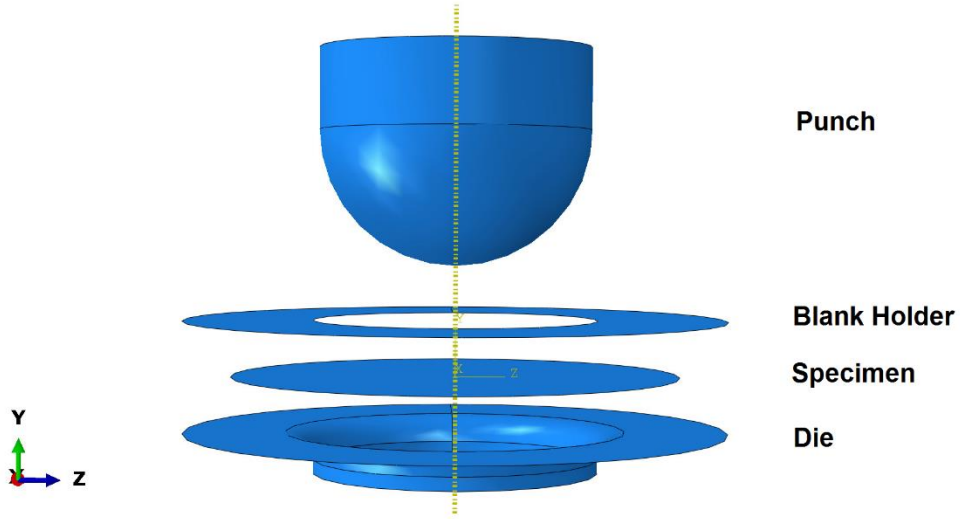

Figure 3.12 Explode view of the FEA model assembly

There are three steps involved in the simulation: the initial step, the pre-stretch step and the press step. The initial step is a default step created in the ABAQUS program. The other two steps are (Static, General) steps defined by the user. In the initial step, the boundary condition for the die is applied as fixed in all degrees of freedom. This boundary condition is propagated in the next two steps. In the pre-stretch step, the punch is held still with the original position as just in contact with the specimen. The blank holder is only allowed displacement in the y axis and is applied with a load acting in the negative y direction to simulate the fastening process between the blank holder and the die. In this pre-stretch step, a uniform edge load is applied on the edge of the specimen acting in the outwards direction, as shown in Figure 3.13. During the fastening process, the specimen is drawn outwards around the edge and experiences tensile loading. This process is simulated by applying the edge load during the pre-stretch stage. The magnitude of this edge load is adjusted for each specimen to have the same trend of strain path as the experiments. Finally, in the press step, a displacement of 30mm in the negative y direction is applied on the punch. During the press step, the specimen edge is fixed in all directions. In the user-defined two steps, the initial, minimum and maximum time increments are defined as 0.01s, 10^{-10}s and 0.1s. The total time period is set as 0.1s for the pre-stretch step and 1s for the press step. There are three interactions of surface contacts in the simulation: punch-specimen, blank holder-specimen and die-specimen. Due to the existence of unavoidable friction during the experiments, penalty contact conditions are used in all the contact conditions in the simulation.

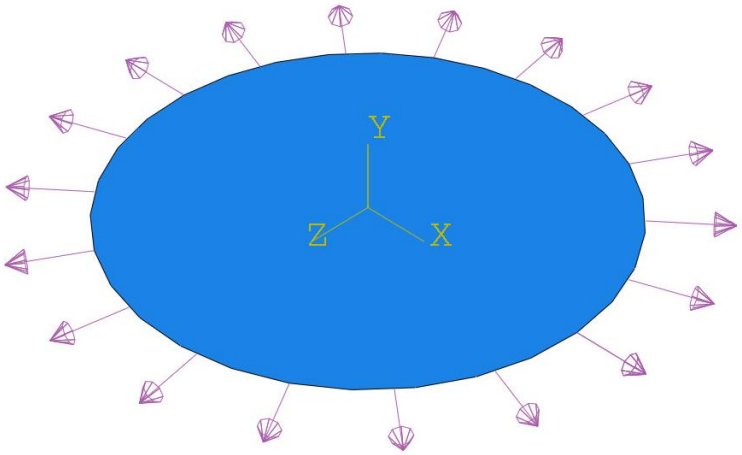

Figure 3.13 Schematic of the edge load applied on the specimen

For the punch, blank holder and die simulated in the FEA model, the surface type is defined as 3D Analytic rigid shell. In this surface type, meshing is not required and these surfaces will not deform during the simulation process. Due to the dimensions of the specimen, the specimen is modelled as thin shell elements. The element type used for the specimen is S4R, which is a 4-node doubly curved thin or thick shell with reduced integration [96]. This element type (S4R) is a robust and general-purpose element that is suitable for a wide range of applications. The uniformly reduced integration can avoid shear and membrane locking [97]. The approximate mesh size for a typical element is 3mm x 3mm, resulting in 1032 elements in the smallest specimen (F25) and around 3000 elements in the full circular specimen (F200). A model with fine mesh size of 1.5mm x 1.5mm for the F200 specimen is also solved for convergence test. The resulted element number is 11688, which is four times of the original model. The difference in the maximum principal strain is only 1.2% between the two models of

different mesh size. It is found that the mesh size of 3mm x 3mm can provide accurate predictions of the experiments with lower simulation cost.

The material properties for the specimen are determined by a user-defined subroutine file, which is attached in Appendix A. In this file, the GFRP material is characterized as an orthotropic material with the stress/strain relation as follows:

$$\begin{Bmatrix} \sigma_{11} \\ \sigma_{22} \\ \sigma_{33} \\ \tau_{23} \\ \tau_{13} \\ \tau_{12} \end{Bmatrix} = [\mathrm{C}][\varepsilon] = \begin{bmatrix} C_{11} & C_{12} & C_{13} & 0 & 0 & 0 \\ C_{12} & C_{22} & C_{23} & 0 & 0 & 0 \\ C_{13} & C_{23} & C_{33} & 0 & 0 & 0 \\ 0 & 0 & 0 & C_{44} & 0 & 0 \\ 0 & 0 & 0 & 0 & C_{55} & 0 \\ 0 & 0 & 0 & 0 & 0 & C_{66} \end{bmatrix} \times \begin{Bmatrix} \varepsilon_{11} \\ \varepsilon_{22} \\ \varepsilon_{33} \\ \gamma_{23} \\ \gamma_{13} \\ \gamma_{12} \end{Bmatrix} \quad 3.6.7$$

with

$$C_{11} = C_{22} = \frac{E}{1 - v^2} \quad 3.6.8$$

$$C_{12} = C_{21} = \frac{Ev}{1 - v^2} \quad 3.6.9$$

$$C_{66} = \frac{E}{2(1 + v)} \quad 3.6.10$$

$$C_{44} = C_{55} = \frac{5}{6} C_{66} \quad 3.6.11$$

where [C] is the stiffness matrix; E is the Young's Modulus and v is the Poisson's ratio. With this relation, the default direction of the composite material is in [0°/90°]. For the [±45°] direction specimens, the orientation can be directly applied on the simulated specimen, as shown in Figure 3.14. Since the set-up of the experiment is axisymmetric, different orientations for the full circular specimen will have the same results. For the hourglass specimens though, the orientation is significant in both experiments and simulations.

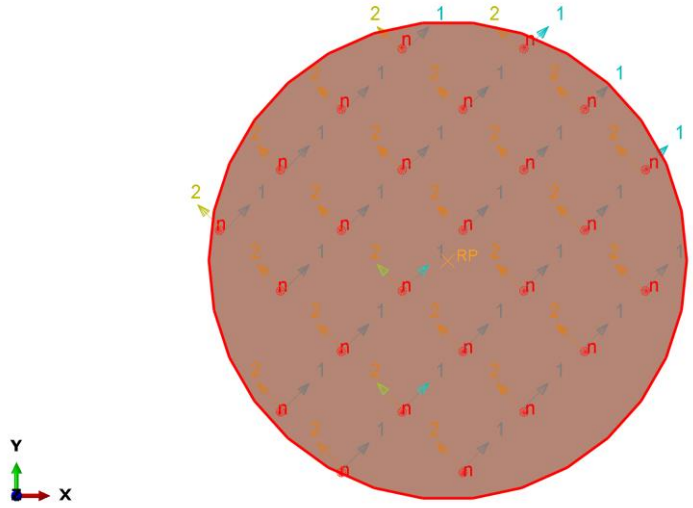

Figure 3.14 Off-fibre orientation specimen simulated in FEA

3.7 SUMMARY

This chapter discusses the GFRP composite material and the methodologies employed in this study. The characteristics of the constituent materials are discussed first, along with the composite material's manufacturing method, structural pattern and applications. Then the specimen design is elucidated and the preparations for the specimens are introduced. After the discussion of the specimens, the experimental set-up is described and details of the custom-built experimental tools are given. During the experiments, a 3D DIC system (ARAMIS®) is used to obtain real-time and full-field strain information. The characteristics of this DIC system are discussed as well. Finally, the FEA simulation is detailed, including the implicit analysis method and the development of the simulation model.

Chapter 4 Experimental and Simulation Results

4.1 INTRODUCTION

In this chapter, the experimental results are discussed, along with the simulation results. First, the approach used in analysing the experimental results is introduced. This is followed by the discussions of the experimental results for the [0°/90°] specimens and [±45°] specimens, respectively. In these discussions, the failure envelope based on the principal strains and the failure envelope based on the fibre strain are both illustrated. Finally, incorporations of failure models in FEA simulations are described.

4.2 ANALYSIS OF EXPERIMENTAL RESULTS

In this section, the principal strains and their relation to deformation modes are first elucidated. Then the evolution of surface strains in the 3D DIC system is described and a typical strain path is presented. Finally, the implementation of the strain experienced by the fibre bundle in the DIC system during loading is introduced.

4.2.1 Regional Divisions

During the experiments, different regions on the specimen surface offer different information. They are divided as pole region, mid region and flange region, as shown in Figure 4.1. The pole region is in the centre and the strain evolution in this region can be captured by the 3D DIC system. This region experiences the largest displacement during the experiments. The mid region is the region in between pole and flange regions. The strain evolution in this region is also recordable in the DIC system. Finally, the flange region is further away from the pole region and is covered by the attached tab

and the die. For some specimens, failure can occur in the flange region where strain information is not available. By changing the specimen geometry, it is possible to induce different deformation modes in the pole region and evaluate the influence of the deformation mode on the GFRP material system.

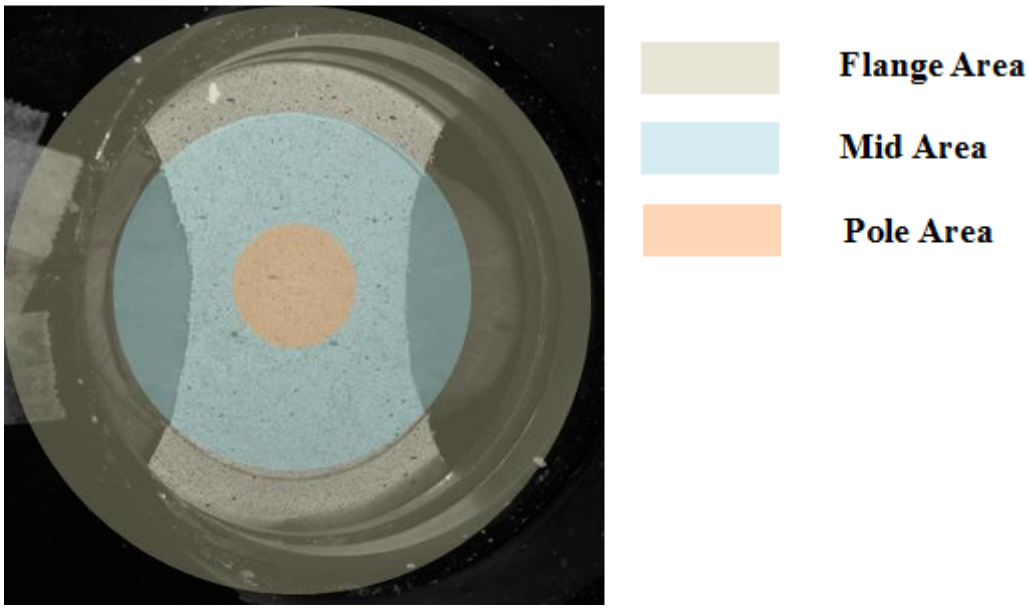

Figure 4.1 Region divisions of the specimens

4.2.2 Strain Tensors and Deformation Modes

Among the measures investigated to study failure of a material system, the states of stress and strain are the most common approaches. In this thesis, a strain based approach is utilized to elucidate the failure behaviour of the GFRP composite. The strain based failure envelope is often based on principal strains. For the specimens used in this work, the thickness is small compared to the other dimensions and the specimen experiences loading that are in plane and perpendicular to the specimen. The kinematics

of this loading condition can be described by thin shell behaviour. Hence two principal strains are sufficient to characterize the failure of this material system. The principal strains can be determined by the following equation:

$$\epsilon_{1,2} = \frac{\epsilon_x + \epsilon_y}{2} \pm \sqrt{(\frac{\epsilon_x - \epsilon_y}{2})^2 + (\frac{\gamma_{xy}}{2})^2} \quad 4.2.1$$

where $\epsilon_{1,2}$ are the major and minor principal strains, ϵ_x and ϵ_y are the strains in the global xy coordinate and γ_{xy} is the shear strain.

The principal strains can be visualized by an undeformed circular area being deformed into an ellipse, as shown in Figure 4.2. The magnitudes of the two principal strains are given by the following equations.

$$\epsilon_1 = \ln\left(\frac{d_1}{d_0}\right), \epsilon_2 = \ln\left(\frac{d_2}{d_0}\right) \quad 4.2.2$$

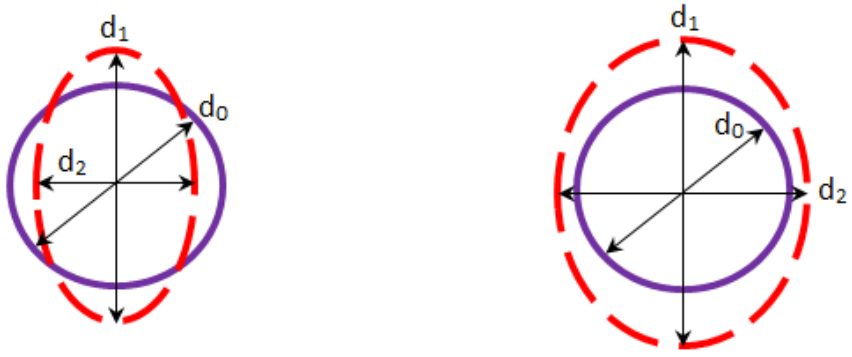

Figure 4.2 The visualization of an undeformed circular area being deformed into an ellipse

The relation between deformation modes and the principal strains are shown in Figure 4.3 [98]. When both major and minor strains are positive, the element is under biaxial tension deformation mode. In the case of equal positive principal strains, the deformation mode is named as equi-biaxial tension. When the minor strain equals to zero, this deformation mode is considered as plane strain mode. When the minor principal strain is negative, the possible deformation modes include uniaxial compression, pure shear and uniaxial tension.

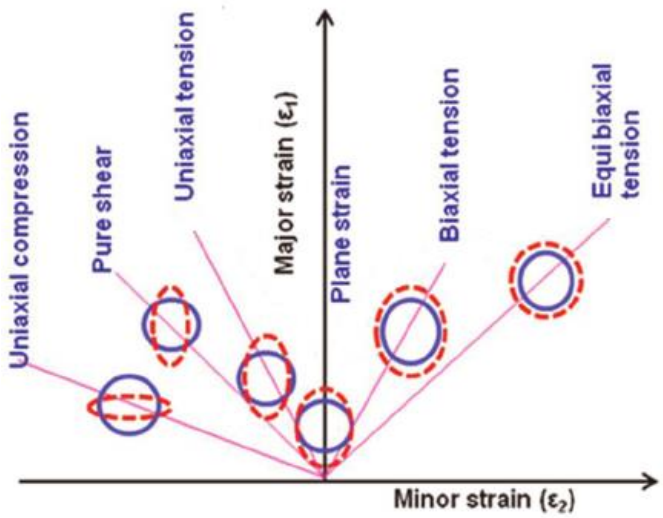

Figure 4.3 Relationship between principal strains and deformation modes [98]

To better illustrate the relationship between deformation modes and principal strains, the concept of strain ratio is introduced. Strain ratio (β) is the ratio of the minor principal strain divided by the major principal strain, as shown in Equation 4.2.3.

$$\beta = \frac{\epsilon_2}{\epsilon_1} \qquad 4.2.3$$

In this case, the deformation mode can be related to one value β. When β is positive, the element is under biaxial tension. When β equals to 1, the deformation mode is equi-biaxial tension. When β is zero, it is the plane strain state. For pure shear, the β value equals to -1. When β is below -1, the failure is often due to buckling. For the experiments performed in this study, the β value ranges between -1 and 1.

4.2.3 Evolution of Surface Strain

The major principal strain evolution of specimen F100 is shown in Figure 4.4. It represents a typical case of strain evolution of the GFRP specimens. The twill weave of the material induces the strain contour to have a pattern during loading. In the pole region where the deformation is expected to be large, a high strain region exists. The values of the major principal strain keep increasing with the increase in loading, until failure occurs in one of the high strain regions. The minor principal strain evolution of specimen F100 is shown in Figure 4.5. When comparing the major and minor principal strain contours, whilst some similarity in strain patterns is observed, the location of high values of strains can be different.

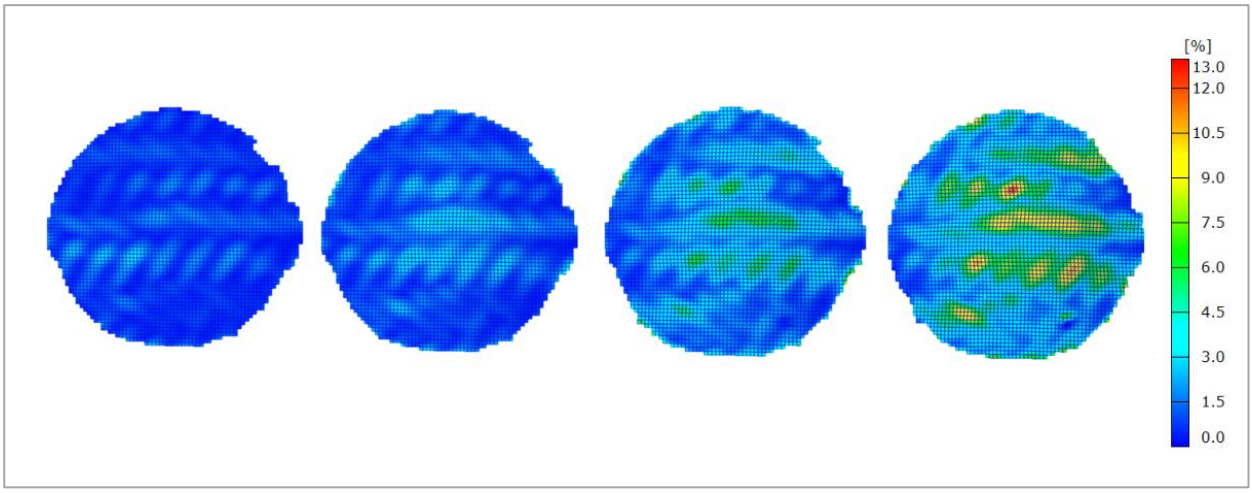

Figure 4.4 Evolution of major principal strain for specimen F100

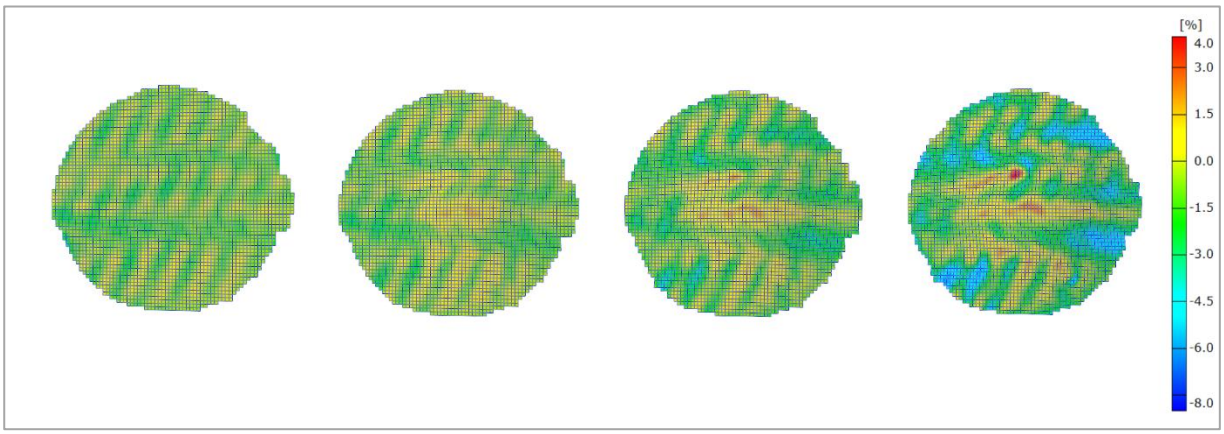

Figure 4.5 Evolution of minor principal strain for specimen F100

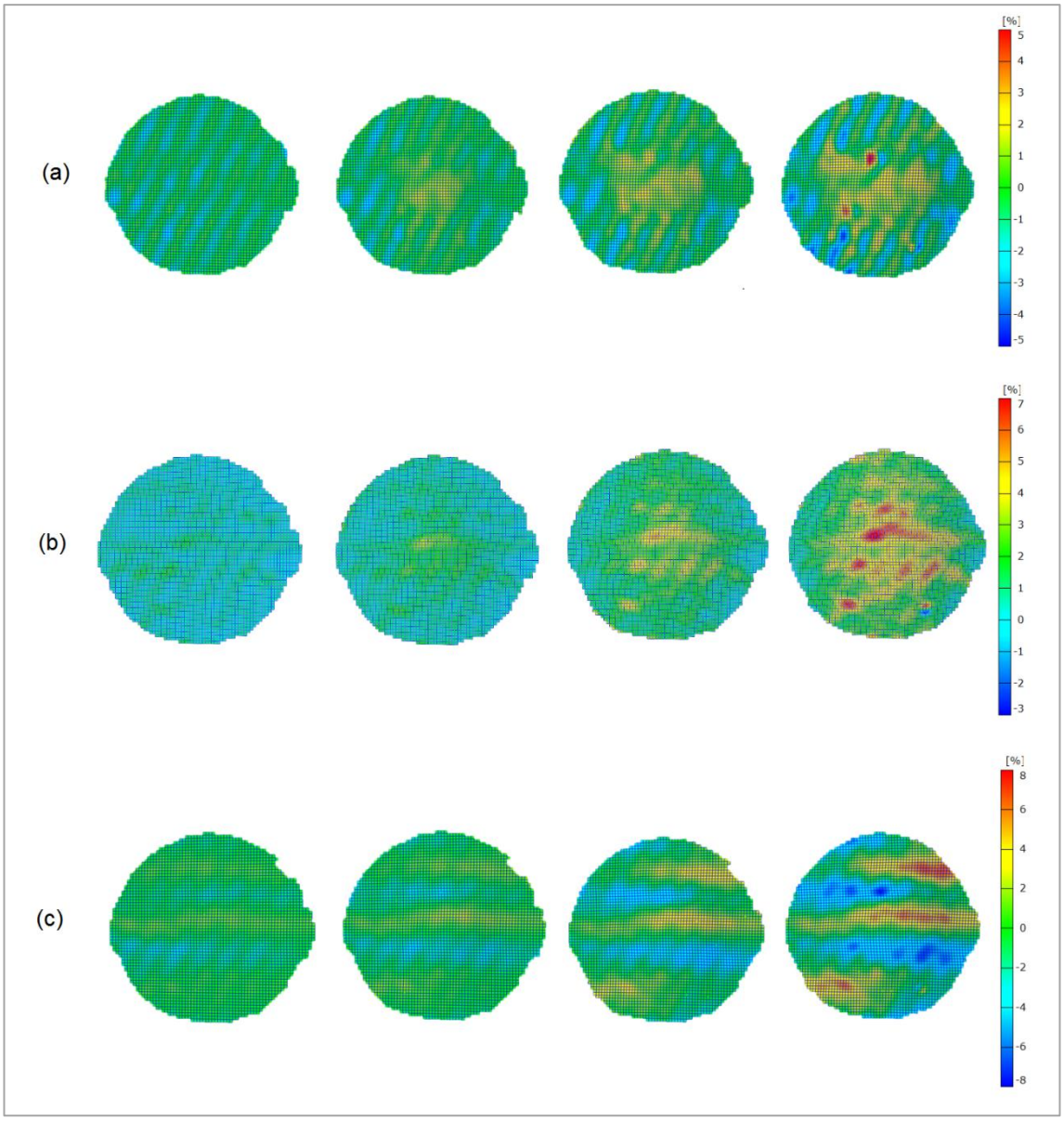

Figure 4.6 Evolution of strain contour for specimen F100 (a) ϵ_x; (b) ϵ_y; (c) ϵ_{xy}

In Figure 4.6 are the strain contour evolutions of specimen F100 in the global coordinate. In specimen F100, the global xy coordinate aligns with the orthogonal fibre directions. The hourglass geometry follows the y direction, which means fibres in the y direction were completely held at the edges during the experiments. From the strain evolution of ϵ_x, it is found that high strain areas gradually emerge in the pole region. The strain pattern caused by the twill weave of this material is observed. This pattern is also found in the evolution of ϵ_y strain. In the evolution of ϵ_y strain contour, large strains are also observed in the pole region. By comparing the strain values of the ϵ_x and ϵ_y, it is found that the strains in the y direction are slightly higher than strains in the x direction. From the strain contour evolution of ϵ_{xy}, both positive and negative shear strains are observed. The magnitudes of ϵ_{xy} keep increasing with the increase of loading.

4.2.4 Typical Strain Path

For most specimens, pole region has the highest strain level and failure initiation is expected to occur here. As shown in Figure 4.7 (a), a typical example of the strain path (history) at the pole region is illustrated. There are three stages of deformation modes in the strain path. Stage 1 is called pre-stretch stage. This stage is caused by fastening the custom-built blank holder and die, as mentioned in Chapter 3 Material and Methodology. Before the blank holder is placed and fastened, the zero strain state is recorded as the start point. After the blank holder is fastened on the die, due to the lock ring design, specimen would be stretched around its edge and this process is called pre-stretch. Since this stage is only based on the initial status and the end status for this stage. Stage 1 is not plotted in the strain path graph since it does not indicate the actual

strain path during this stage. Stage 2 and 3 both present the experimental process when the specimen is pressed by the punch. Stage 2 is in the initial stage of the experiment when the punch establishs initial contact with the specimen. At this stage, only the pole region deforms with punch and hence exhibits a deformation mode towards incremental biaxial tension for this short period. Stage 3 refers to the deformation mode where the failure of the specimen occurs. For specimens with different geometries, the strain paths in Stage 3 exihibit different deformation modes. The strain paths of the failed regions for the [0°/90°] specimens are given as examples and illustrated in Figure 4.7 (b).

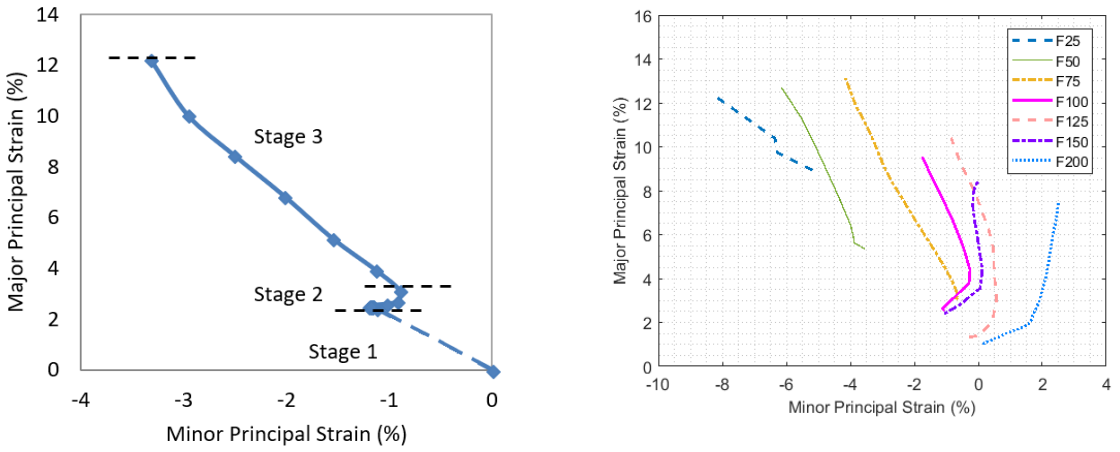

(a) (b)

Figure 4.7 (a) A typical strain path in the principal strains domain; (b) Examples of strain path for [0°/90°] specimens

4.2.5 Evolution of Fibre Strain and Implementation in the DIC system

The algorithm used to calculate the evolution of the fibre strain is developed by Wang [99]. This algorithm tracks the evolution of fibre movement with the matrix deformation and provides the strain values along the fibre directions. In this section, the kinematics

of the algorithm are introduced first. Then the implementation of this algorithm in the DIC system is discussed.

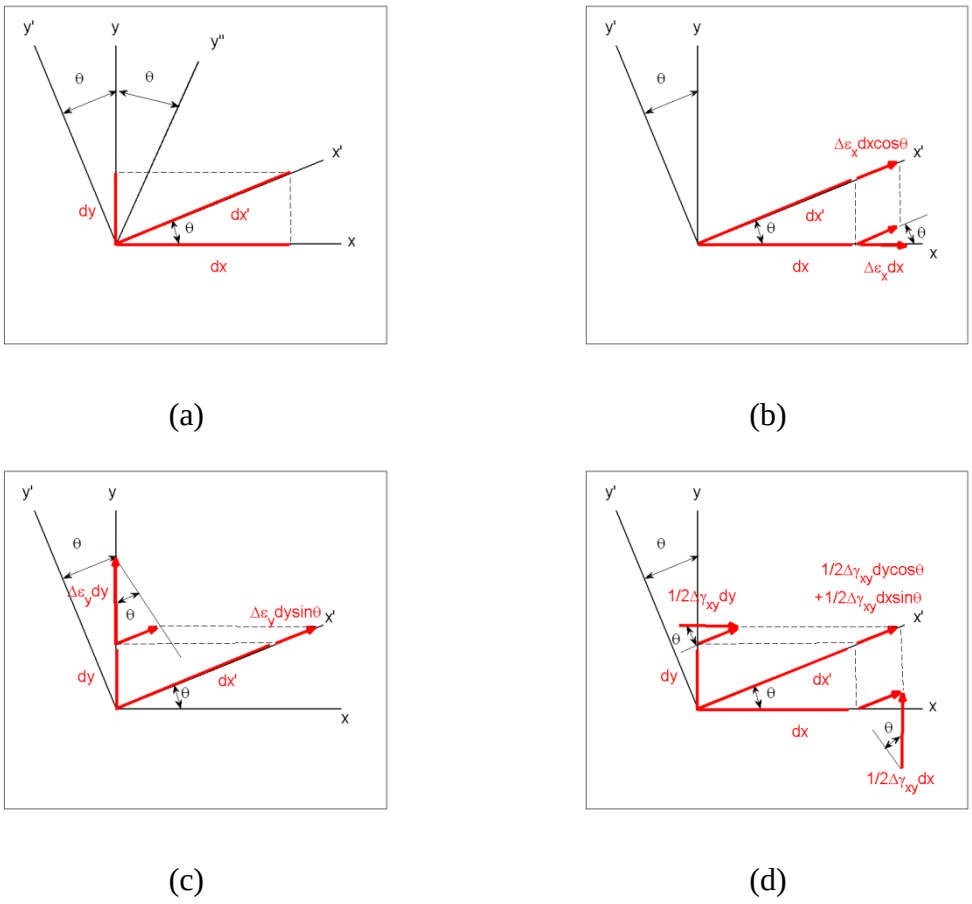

Figure 4.8 The kinematics of fibre strain calculation [99] (a) overview; (b) normal strain in the x direction; (c) normal strain in the y direction; and (d) shear strain

Figure 4.8 [99] illustrates the transformation of the strains from the global xy coordinate to the fibre orientations. Figure 4.8 (a) indicates that, due to the matrix shear deformation, the fibres are aligned with the x' and y'' directions during the experiment. The y' direction is perpendicular to the x' direction and is used for calculation of the fibre strain in the x' direction. In Figure 4.8 (b), the normal strain along the x direction ($dx + \Delta\varepsilon_x dx$) is transformed to the strain along the x' direction ($dx' + \Delta\varepsilon_x dx \cdot cos\theta$).

In Figure 4.8 (c), the normal strain along the y direction ($dy + \Delta\varepsilon_y dy$) is transformed to the strain along the x' direction ($dx' + \Delta\varepsilon_y dy \cdot sin\theta$). In Figure 4.8 (d), the shear strain in the global xy coordinate is also transferred to the x' direction, which is one of the fibre directions.

During the experiment, the incremental strains in the global coordinate system can be calculated as:

$$\Delta{\varepsilon_x}^i = {\varepsilon_x}^i - {\varepsilon_x}^{i-1}, \ \Delta{\varepsilon_y}^i = {\varepsilon_y}^i - {\varepsilon_y}^{i-1}, \Delta{\gamma_{xy}}^i = {\gamma_{xy}}^i - {\gamma_{xy}}^{i-1} \quad 4.2.4$$

where i represents the i[th] increment of the calculation, $\varepsilon_x, \varepsilon_y, \gamma_{xy}$ are the strains in global x, y and shear directions, and $\Delta\varepsilon_x, \Delta\varepsilon_y, \Delta\gamma_{xy}$ represent the incremental strains in the global x, y and shear directions.

The elongation along the x' direction is computed first, and its components along the x and y directions can be calculated as:

$$dx'^{,i} = dx/\cos\theta^i, \ \ dy'^{,i} = dy/\sin\theta^i \quad 4.2.5$$

where $dx, dy, dx'^{,i}$ correspond to the elongations along the x, y and x' directions, respectively, and θ^i represents the angle of rotation.

The resultant incremental elongation along the x' direction is the sum of components from the normal strain in the x direction, the normal strain in the y direction and shear

strain (as described in Figure 4.8 b-d). The equations for calculating the incremental strain along the x' direction are as follows:

$$\delta x'^{,i} = \Delta\varepsilon_x^i dx \cos\theta^i + \Delta\varepsilon_y^i dy \sin\theta^i + 1/2 * \Delta\gamma_{xy}{}^i \Delta\varepsilon_y^i \cos\theta^i + 1/2 * \Delta\gamma_{xy}{}^i \Delta\varepsilon_x^i \sin\theta^i \quad 4.2.6$$

$$\Delta\varepsilon_x'^{,i} = \delta\varepsilon_x'^{,i}/dx'^{,i} \quad 4.2.7$$

$$\Delta\,\varepsilon_x'^{,i} = \Delta\varepsilon_x^i \cos^2\theta^i + \Delta\varepsilon_y{}^i \sin^2\theta^i + \Delta\gamma_{xy}{}^i \sin\theta^i \cos\theta^i \quad 4.2.8$$

where $\delta x'^{,i}$ is the resultant incremental elongation along the x' direction, and $\Delta\,\varepsilon_x'^{,i}$ is the incremental strain along the x' direction.

The incremental strain along the x' direction in Equation 4.2.8 can be simplified to the expression shown in Equation 4.2.9 based on trigonometric identities.

$$\Delta\,\varepsilon_x'^{,i} = \frac{\Delta\varepsilon_x^i + \Delta\varepsilon_y{}^i}{2} + \frac{\Delta\varepsilon_x^i - \Delta\varepsilon_y{}^i}{2}\cos 2\theta^i + \frac{\Delta\gamma_{xy}{}^i}{2} sin2\theta^i \quad 4.2.9$$

The incremental elongation and incremental strain along the y' direction can be obtained by substituting (90+θ^i) for θ^i in Equation 4.2.6 and Equation 4.2.9.

$$\delta y'^{,i} = -\Delta\varepsilon_x^i dx\, sin\,\theta^i + \Delta\varepsilon_y^i dy \cos\theta^i - 1/2 * \Delta\gamma_{xy}{}^i \Delta\varepsilon_y^i\, sin\,\theta^i + 1/2 * \Delta\gamma_{xy}{}^i \Delta\varepsilon_x^i \cos\theta^i \quad 4.2.10$$

$$\Delta\varepsilon_y'^{,i} = \frac{\Delta\varepsilon_x^i + \Delta\varepsilon_y{}^i}{2} - \frac{\Delta\varepsilon_x^i - \Delta\varepsilon_y{}^i}{2}\cos 2\theta^i - \frac{\Delta\gamma_{xy}{}^i}{2} sin2\theta^i \quad 4.2.11$$

where $\delta y'^{,i}$ is the resultant incremental elongation along the y' direction, and $\Delta\ \varepsilon_y^{\prime,i}$ is the incremental strain along the y' direction.

Then the incremental angle of rotation is calculated:

$$\Delta\gamma_{xy}{}'^{,i} = \delta y'^{,i}/dx'^{,i} + \delta x'^{,i}/dy'^{,i} \quad 4.2.12$$

$$\delta y'^{,i}/dx'^{,i} = \left(-\Delta\varepsilon_x^i + \Delta\varepsilon_y{}^i\right)\sin\theta^i\cos\theta^i - \Delta\gamma_{xy}{}^i\sin^2\theta^i \quad 4.2.13$$

$$\delta x'^{,i}/dy'^{,i} = (-\Delta\varepsilon_x^i + -\Delta\varepsilon_y^i)\sin\theta^i\cos\theta^i + \Delta\gamma_{xy}{}^i\cos^2\theta^i \quad 4.2.14$$

$$\Delta\gamma_{xy}{}'^{,i} = -(\Delta\varepsilon_x{}^i - \Delta\varepsilon_y{}^i)sin2\theta^i + \Delta\gamma_{xy}{}^i cos2\theta^i \quad 4.2.15$$

where $\Delta\gamma_{xy}{}'^{,i}$ is the incremental angle of rotation.

Incremental strain along another fibre direction (the y'' direction) can be computed by substituting (90-θ^i) for θ^i in Equation 4.2.11:

$$\Delta\ \varepsilon_y^{\prime\prime,i} = \frac{\Delta\varepsilon_1^i + \Delta\varepsilon_2{}^i}{2} - \frac{\Delta\varepsilon_1^i - \Delta\varepsilon_2{}^i}{2}\cos 2\theta^i + \frac{\Delta\gamma_{12}{}^i}{2}sin2\theta^i \quad 4.2.16$$

where $\Delta\ \varepsilon_y^{\prime\prime,i}$ is the incremental strain along the y'' direction.

Now the fibre strains in both directions are obtained. The larger one between these two strain values is used to represent the fibre strain at this point when developing the fibre strain envelope.

$$\varepsilon_x{}'^{,i} = \varepsilon_x{}'^{,i-1} + \Delta\varepsilon_x'^{,i} \quad 4.2.17$$

$$\varepsilon_y{}''^{,i} = \varepsilon_y{}''^{,i-1} + \Delta\varepsilon_y''^{,i} \quad 4.2.18$$

$$\varepsilon_{fibre}{}^{i} = maximum(\varepsilon_x{}'^{,i}, \varepsilon_y{}''^{,i}) \quad 4.2.19$$

Where $\varepsilon_x{}'^{,i}$ and $\varepsilon_y{}''^{,i}$ represent the strain along the fibre directions, and $\varepsilon_{fibre}{}^{i}$ is the fibre strain used in developing the fibre strain envelope.

In each increment of calculation, the angle of fibre rotation is also updated and is given by:

$$\theta^{i+1} = \theta^{i} + \Delta\gamma_{xy}{}'^{,i} \quad 4.2.20$$

In analysis of the experimental results, the calculation of the fibre strain evolution is implemented in the ARAMIS® system via a user-defined script, the process of which is illustrated in Figure 4.9 [99]. Firstly, the DIC system (ARAMIS®) can provide incremental normal and shear strains in the global coordinate axes in each stage. The incremental strain information is then used to determine the incremental angle of the rotation through matrix transformation. With this incremental angle of rotation and the rotation information from the previous step, the total angle of rotation can be determined. Then the incremental fibre strain along warp or weft direction can be calculated by transferring the incremental strains in the global coordinate to the fibre directions. Fibre strains in both directions are updated in each stage and the larger of these two values will be used in predicting the failure.

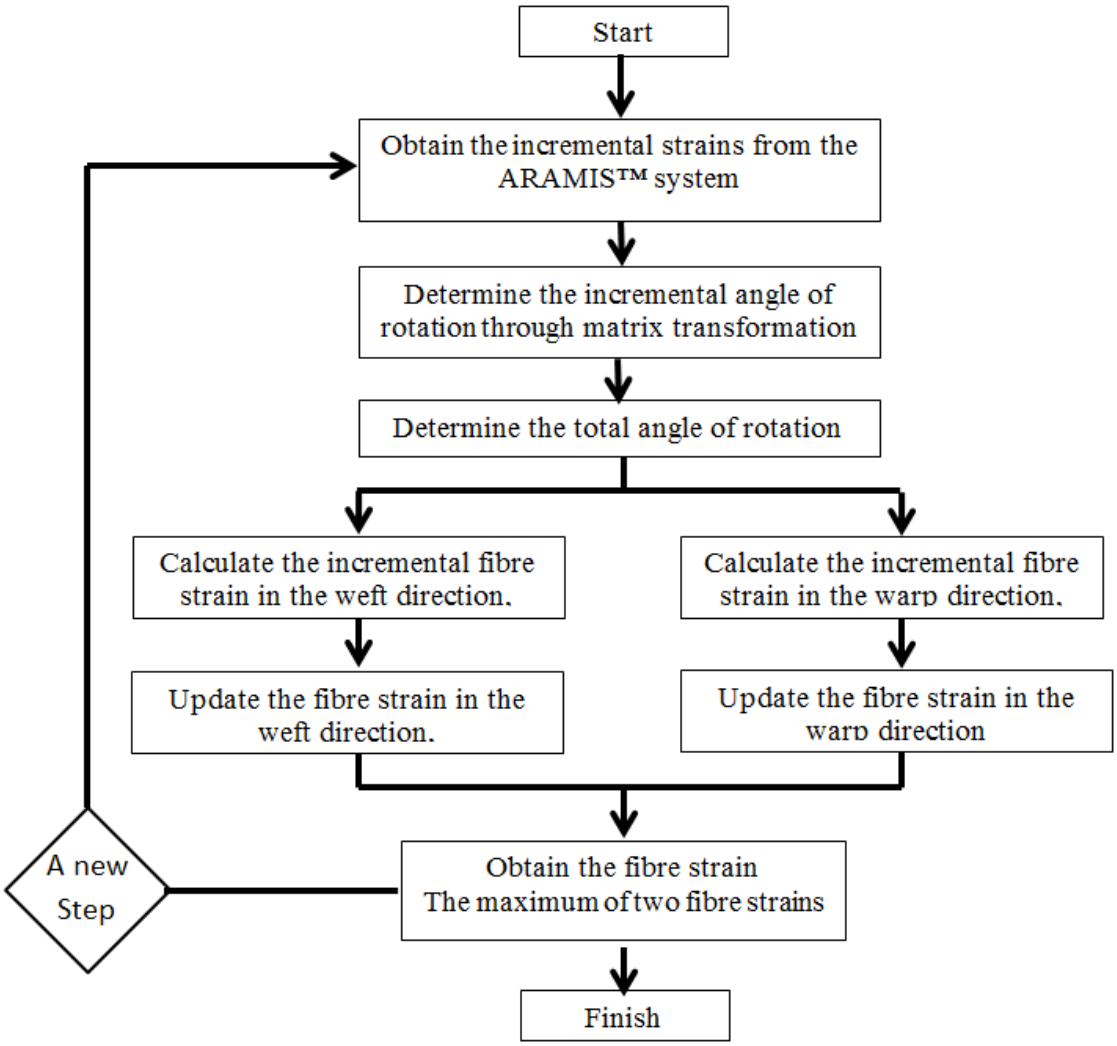

Figure 4.9 Flow chart for calculating fibre strain evolution in the ARAMIS® system [99]

4.3 Experimental Results for [0°/90°] Specimens

This section presents the detailed experimental results for the [0°/90°] specimens. Firstly, strain paths at failed regions are plotted for these specimens. This includes the strain paths that detail the evolution of principal strain and fibre strain. Then the failure

envelopes are presented for the [0°/90°] specimens. Finally, the morphology of the failures in the specimens is discussed.

As shown in Figure 4.10, the failure initiation regions for the [0°/90°] specimens are marked with red circles and are found mainly in the pole regions. Five points in the failure initiation region were picked for each specimen with different specimen widths. The strain paths of the five points were all found to be close to each other and hence the average strain path of the five points is plotted for indication of the strain history.

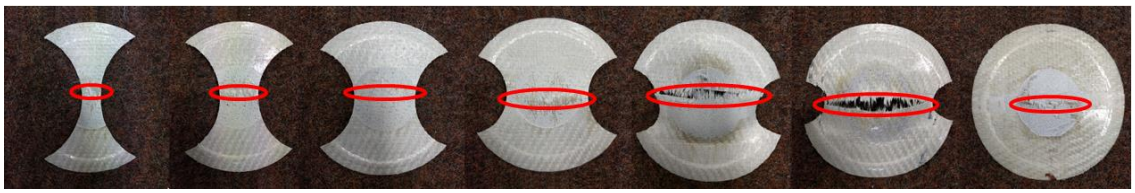

Figure 4.10 Failed [0°/90°] specimens with red circles marking the failed regions

4.3.1 Experimental Results in the Principal Strain Space

The evolution of strains in the principal strain space for the failed regions of the [0°/90°] specimens are plotted in Figure 4.11. This graph clearly illustrates the effect of deformation mode on the failure in the composite material system. As the width of the specimen reduces, the magnitude of the major principal strain increases. Most strain paths are located at negative minor strain region. Only the full circular specimen has strain path that has positive major and minor strains. During the entire experiment, the pole region of specimen F200 was experiencing biaxial tension.

It is also observed that the narrow specimens can experience high major principal strains at the end of stage 1, especially for specimen F25 and F50. Failures occurred shortly after the contact of the punch and the specimen. For wide specimens like F200, pre-stretch stage has minimal effect on the strain path.

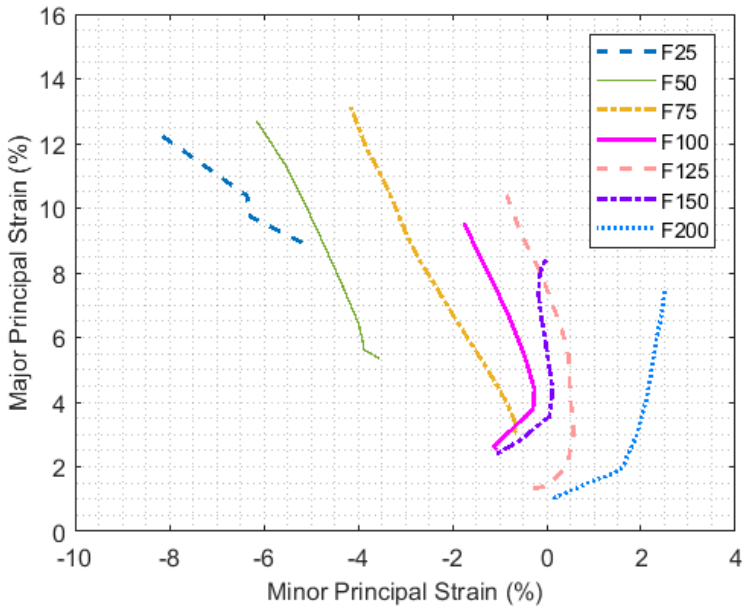

Figure 4.11 Principal strain paths for the [0°/90°] specimens at failed regions

Since the parameter of strain ratio can better depict deformation modes, the evolution of the major principal strain is plotted with strain ratio as the x axis. The original principal strain path and this modified strain path are shown together in Figure 4.12. The modified strain path graph clearly indicates the significant effect of deformation mode on the major principal strain evolution. ***In each strain path, more than one deformation modes are induced by the experimental methodology.*** The evolution of major principal strains is found to be highly sensitive to the history of loading. When the strain ratio is more positive, the major principal strain fails at a lower value. Based

on this rule, the specimens can be divided into three groups. Specimens F25, F50 and F75 all failed at a more negative strain ratio and their major principal strain limits are at a high value of around 13%. Specimens F100, F125 and F150 have strain ratios around 0 at failure. The major principal strains at failure for these specimens are around 9%. For the full circular specimen F200, the strain ratio at failure is the highest while the major strain limit is the lowest at approximately 8%.

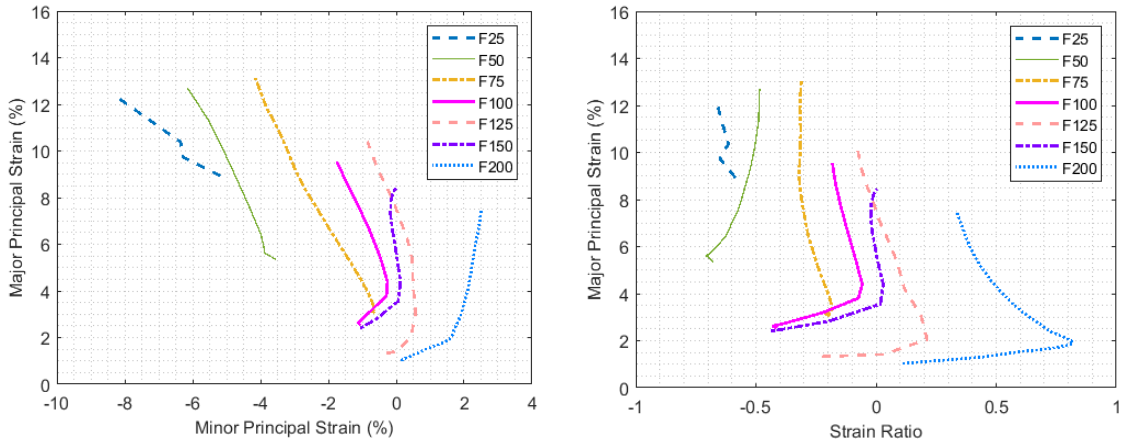

Figure 4.12 Comparison of strain paths for the [0°/90°] specimens at failed regions (a) principal strain path; (b) modified principal strain path

In order to predict failure for a composite material system, the failure envelope in the principal strain space is developed by correlating the strain information on different specimens at the stage just before failure. Based on the experiments performed on the [0°/90°] specimens, the failure envelope in the principal strain space is constructed and illustrated in Figure 4.13. It is found that the failure envelope in the principal strain space varies with the minor principal strain.

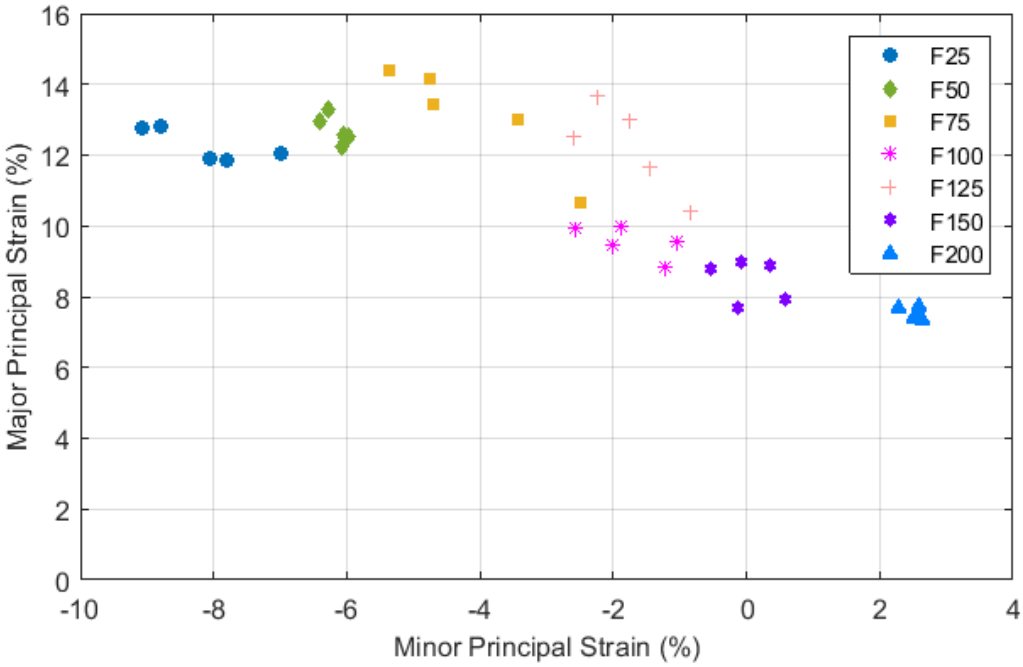

Figure 4.13 The failure envelope in the principal strain space for the [0°/90°] specimens

The modified failure envelope depicts the major principal strain limits in relation to the strain ratio. This modified failure envelope is shown in Figure 4.14. The modified failure envelope can help interpret failures associated with different deformation modes. From the modified failure envelope, it is found that the failures occurred in [0°/90°] specimens with SR ranging from -0.7 to 0.4, covering a wide range of deformation modes.

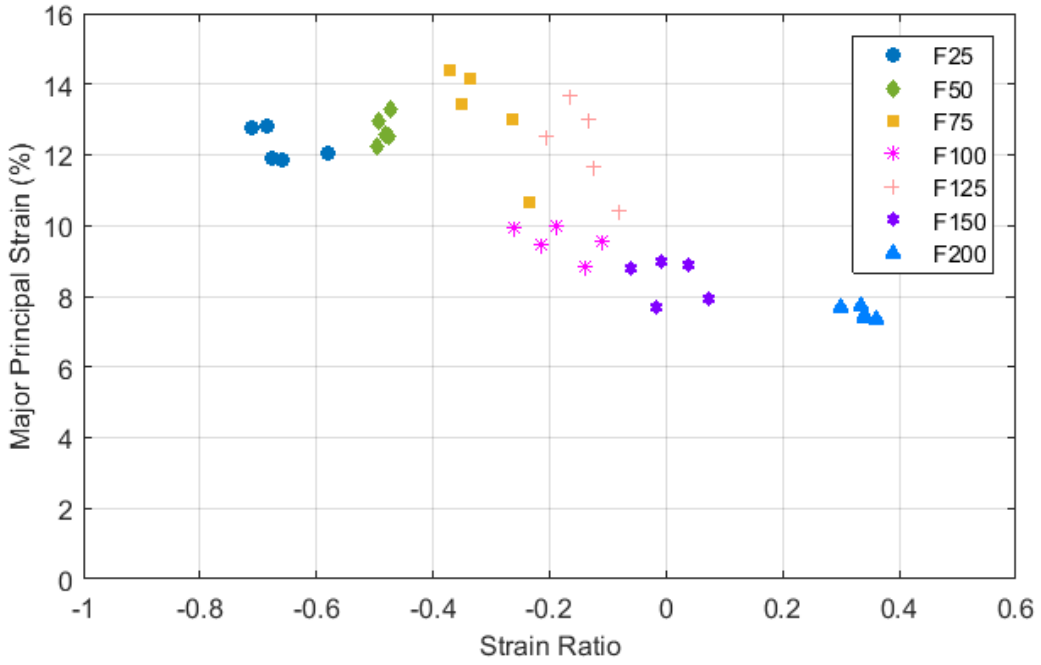

Figure 4.14 Modified failure envelope for the [0°/90°] specimens

It is also observed that specimens with different sectional widths have different major strain limits. Narrow specimens with width 25, 50 and 75 (mm) have large major strain limits between 12% to 14%. For the medium-width and wide specimens, F100, F150 and F200, the major strain limits are all below 10%. With the increase of the specimen width, the major strain limit becomes lower. However, specimen F125 does not follow this rule. It failed at SR similar to that of F100, but it has higher major strain limit.

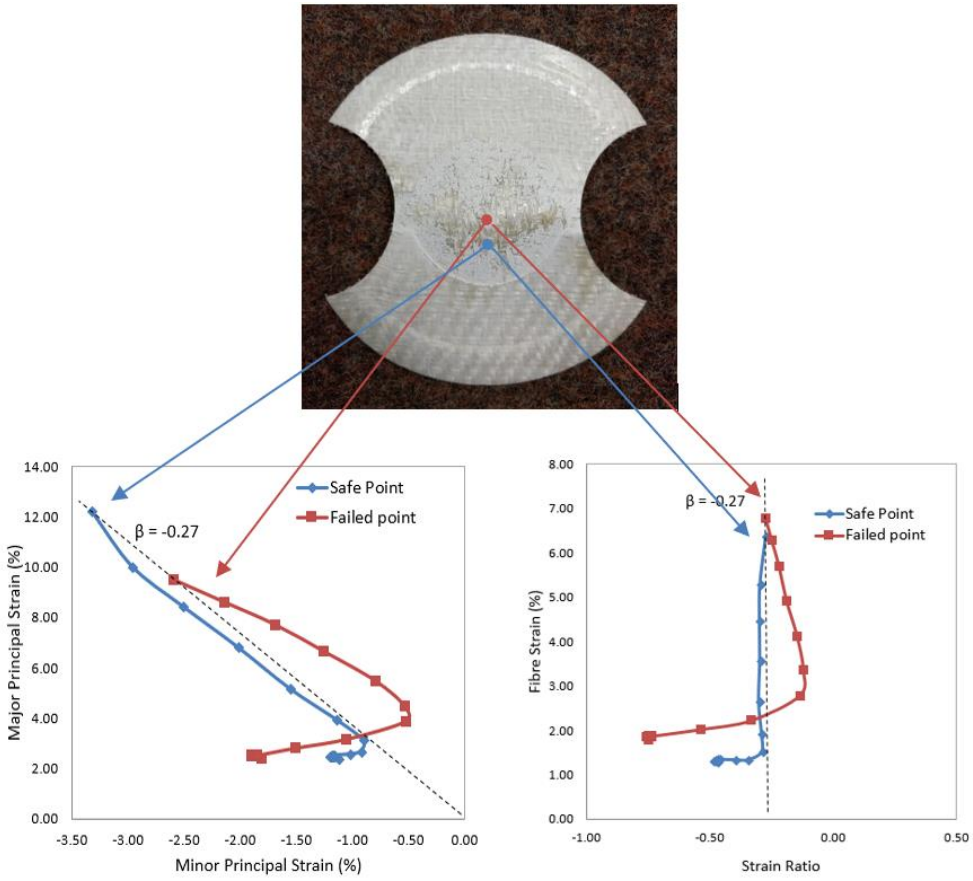

(a) (b)

Figure 4.15 Strain paths for two points of interest in specimen F100 (a) principal strain path ; (b) fibre strain path

In the principal strain space, an anomaly in the strain path is observed in specimen F100 and it is illustrated in Figure 4.15. In this specimen, two points of interest are highlighted on the specimen surface. The blue point indicates a safe location where failure is not observed. The red point indicates a failed location. From Figure 4.15 (a), it is found that these two points of interest reached the same deformation mode (indicated by the same strain ratio) at the end of their strain paths. The anomaly is that the safe point has larger major and minor principal strain magnitudes than the failed point at the last stage before failure. Similar observations were found in other specimens where

there were higher values of principal strains compared to the strains in the failed region. These observations indicate that a failure envelope based on principal strains that does not include path dependency of deformation is inadequate for accounting the failure of this class of composite material systems.

As discussed in 4.2.5, the calculation of fibre strain evolution is implemented in the ARAMIS® system. To evaluate fibre strain as a failure metric for this material system, the fibre stains experienced by the two points of interest in specimen F100 are plotted as a function of strain ratio β, as depicted in Figure 4.15 (b). In the fibre strain path graph, it is found that the safe point in specimen F100 exhibits a lower fibre strain than the failed point. *This result indicates that fibre strain can be a more robust failure metric than the principal strain.* The further examination of the fibre strain path is discussed in the following section.

4.3.2 Experimental Results in the Fibre Strain Space

In the fibre strain theory, it is assumed that the dominant failure in the composite material system is fibre fracture. Therefore, it is fibre strain instead of major principal strain that should be considered as the failure metric. The evolution of the fibre strain as a function of strain ratio of the failed region in [0°/90°] specimens are illustrated in Figure 4.16 (b). For better comparison of the fibre strain path and the principal strain path, the modified strain path graph is shown in Figure 4.16 (a).

By comparing Figure 4.16 (a) and (b), it is found that the fibre strain paths have the same trend as the major principal strain path. They also have three stages and in the last

stage the strain path is dependent on the specimen width. The modified strain path graph has different magnitudes of the major principal strain for different deformation modes. ***An important conclusion from Figure 4.16 is that using fibre strain as a metric for failure eliminates the path dependency effects.***

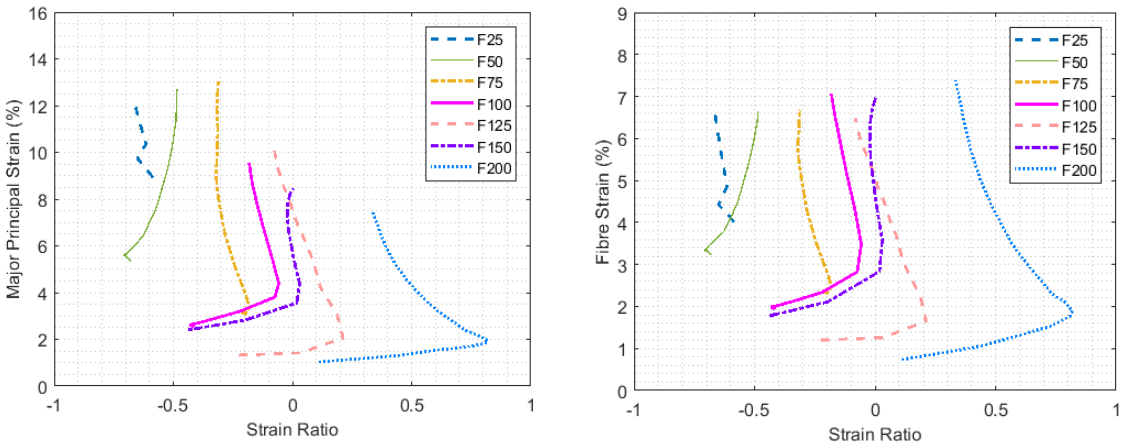

Figure 4.16 Comparison of strain paths for the [0°/90°] specimens at failed regions (a) modified principal strain path; (b) fibre strain path

Failure envelope using the fibre strain theory is developed for the [0°/90°] specimens. The results are shown in Figure 4.17. Unlike the failure envelope in the principal strain space, the fibre strain limits are all in the range between 6% and 8%, regardless of the specimen width. It demonstrates that the fibre strain limit does not vary with different deformation modes for the GFRP material employed in this study. This indicates that the same failure mechanism might exist in all the [0°/90°] specimens. Under the assumption of the fibre strain theory, if the failure mode in a composite material is dominated by fibre fracture, it is highly likely that the fibre strain limits are similar under different deformation modes.

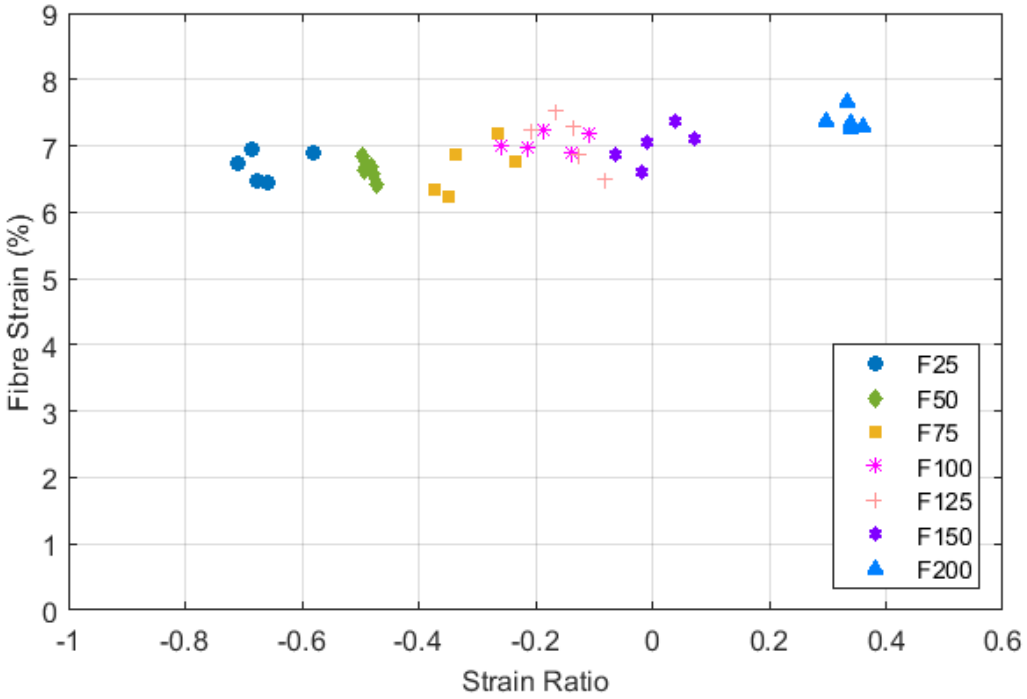

Figure 4.17 Fibre strain failure envelope for the [0°/90°] specimens

4.3.3 Failure Examination

For the [0°/90°] GFRP specimens, the morphology of the failure region based on the severity of the final failure can be classified in three groups, as shown in Table 4.1. The wide specimens in Group 1 exhibited large cracks at the time of failure. Catastrophic failure events occurred in the region that is in contact with the punch. Compared to the Group 1 specimens, the specimens in Group 2 have smaller region of fibre fracture visually. In the Group 3 specimens, the failures are confined in one side of the specimens. Though the different severities of failures were observed, the same failure morphology of fibre fracture is found.

Table 4.1 Groups of the [0°/90°] specimens based on the failure examination

Group Number	[0°/90°] Specimen(s)
1	F125, F150, F200
2	F75, F100
3	F25, F50

The failure examination of the specimens in Group 1 is shown in Figure 4.18. It can be found that the failure in these specimens is the fibre failure in the warp directions. For specimen F150 and F200, the fibre bundles in the warp direction failed almost at the same horizontal level between the weft fibre bundles. For the specimen F125, the warp fibre bundles failed along two or three weft fibre bundles. This can be attributed to the 2/2 twill pattern of the GFRP material system.

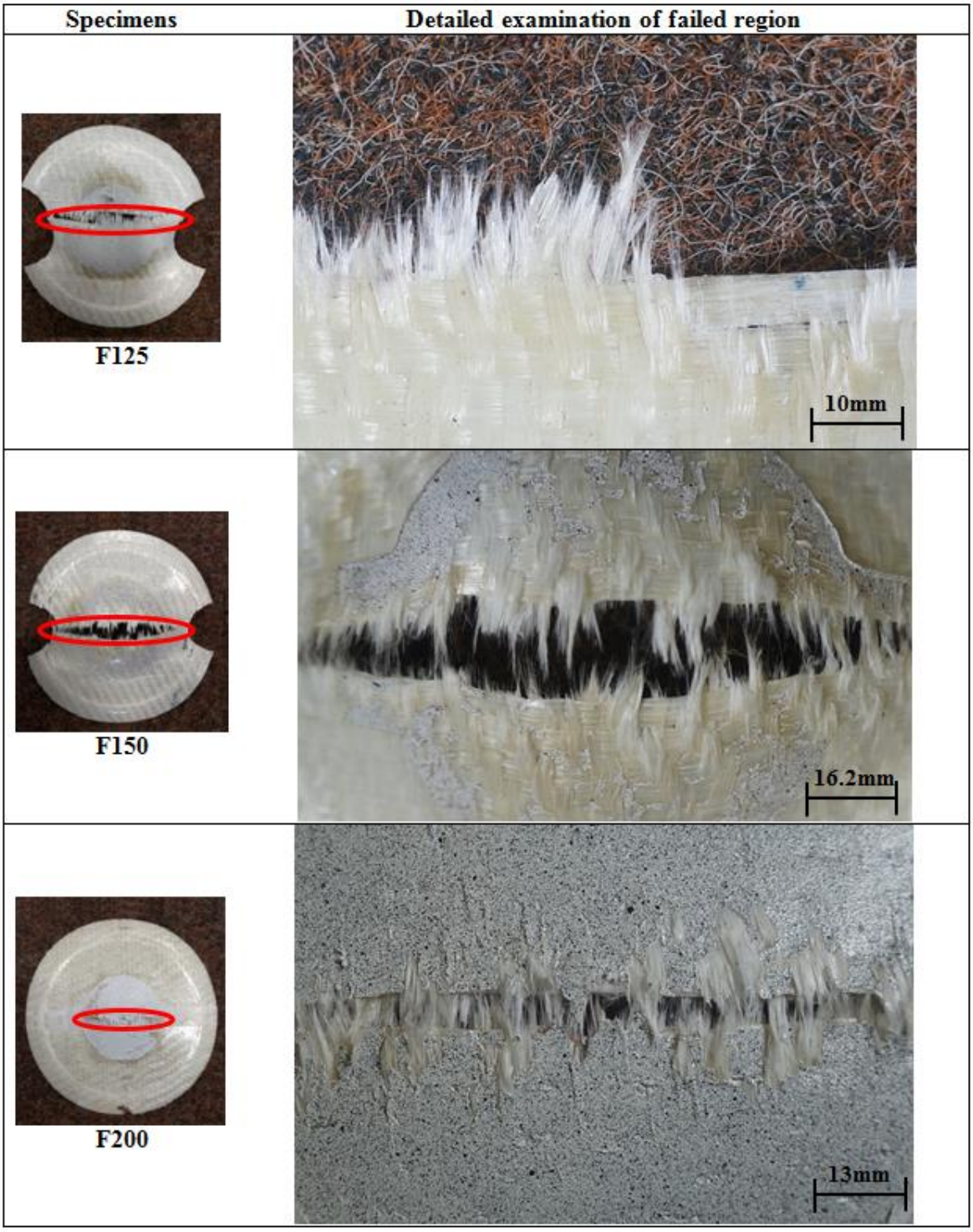

Figure 4.18 Detailed examination of the failed regions for Group 1 specimens

The detailed examination for the specimen F150 is shown in Figure 4.19. From these detailed examinations, it is observed that the dominant failure mode is fibre fracture of the warp fibre bundles.

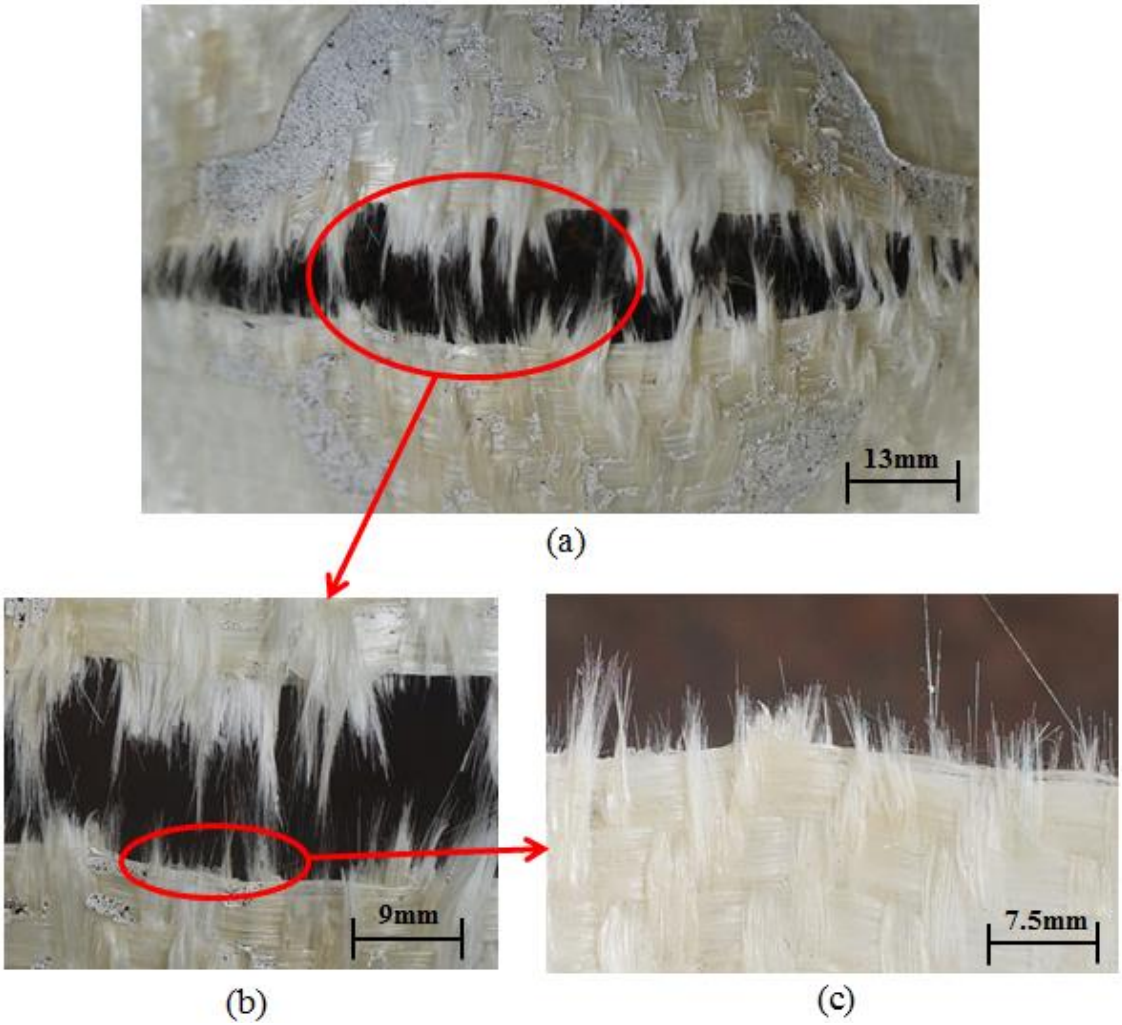

Figure 4.19 Detailed examination of the failed region for specimen F150

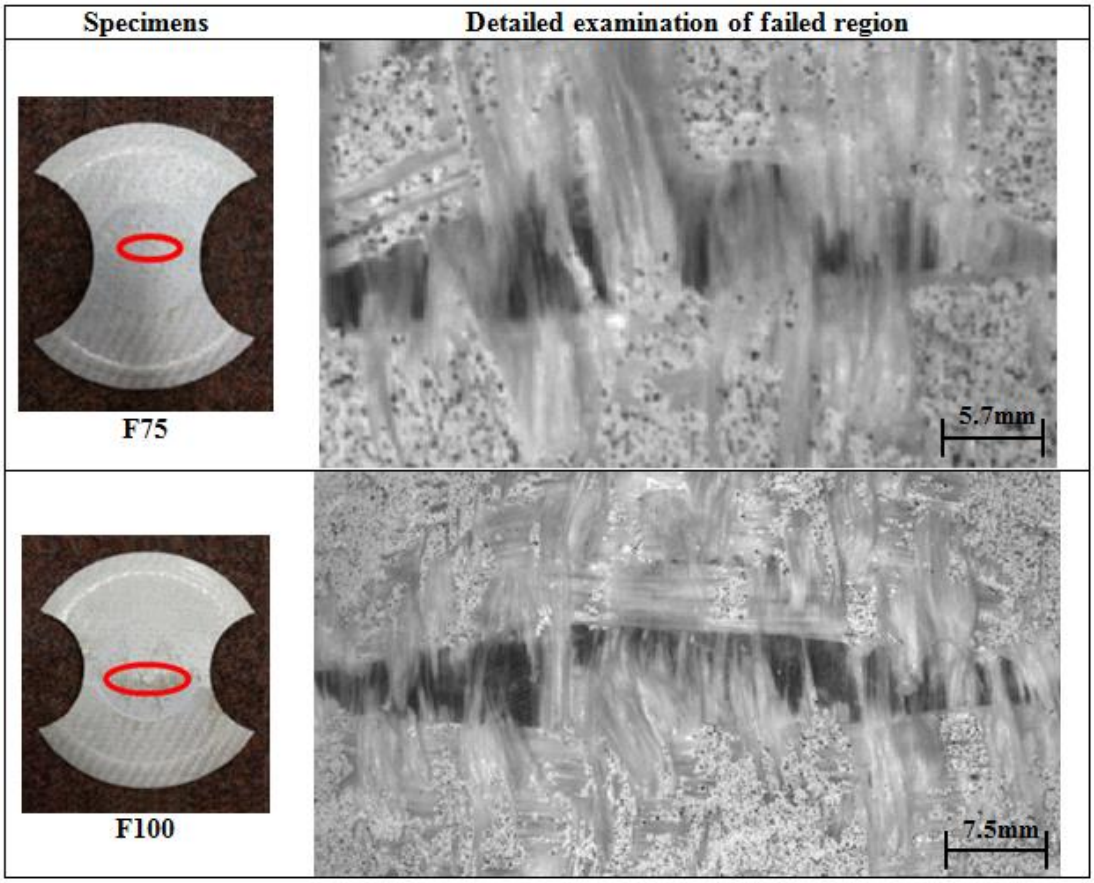

Figure 4.20 Detailed examination of the failed regions of specimen F75 and F100

In examinations of Group 2 specimens illustrated in Figure 4.20, it can be seen that fibre bundle failure is still the dominant failure mode for this group of specimens. Since the failed region is smaller compared to the Group 1 specimens, the failure of these specimens are examined from the images taken by the DIC system during the experiments. The failure behaviour of the Group 2 specimens is essentially the same as the failure behaviour observed in Group 1 specimens.

As shown in Figure 4.21, failures of the two narrow specimens are confined in one side of the specimens. The other side of the specimen is still intact. This observation can be

attributed to the small differences in torques applied to the screws that are used to mount the specimens in the lock ring. Since the two specimens in Group 1 are the two narrowest specimens, the pre-stretch process has the largest effect on these two specimens. Although the six screws on the blank holder and die were fastened with the procedure of applying uniform torques, it is impossible to ensure this uniformity during this process. This led to one side of the specimen experiencing more stretch than the other side. The failure of specimen F50 captured by the DIC system is shown in Figure 4.22. This image demonstrates that the fibre bundle failure is the dominant failure type in the narrow specimens as well.

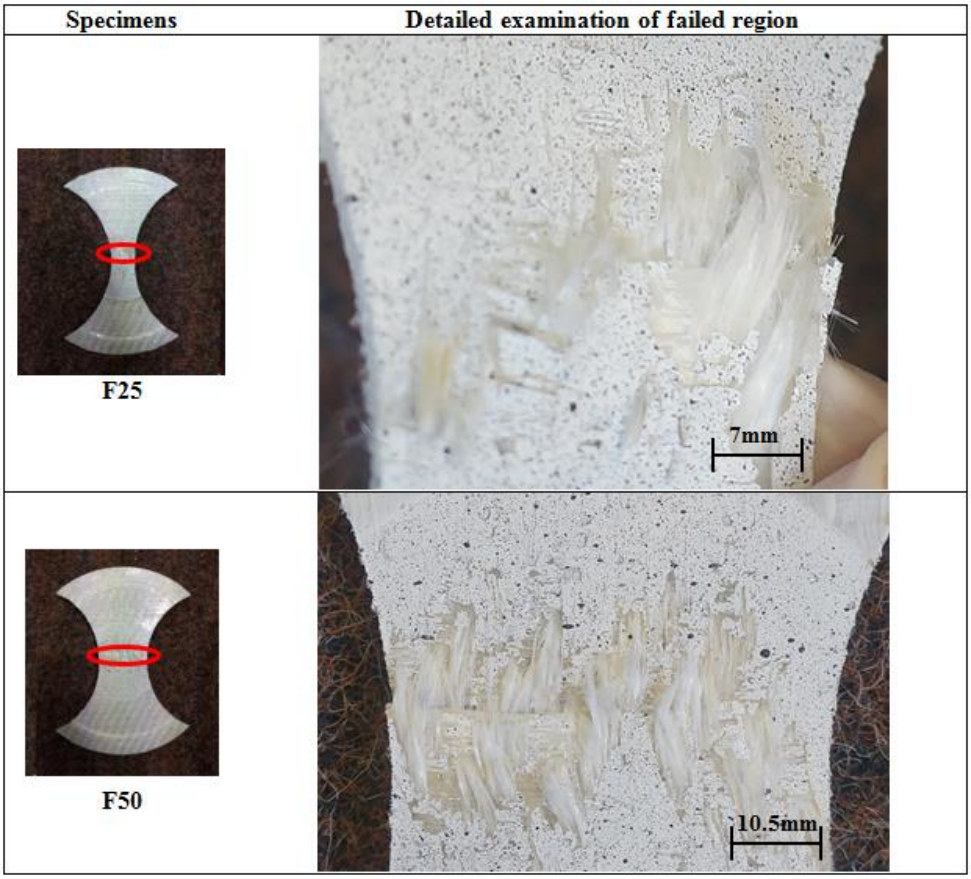

Figure 4.21 Detailed examination of the failed regions of specimen F25 and F50

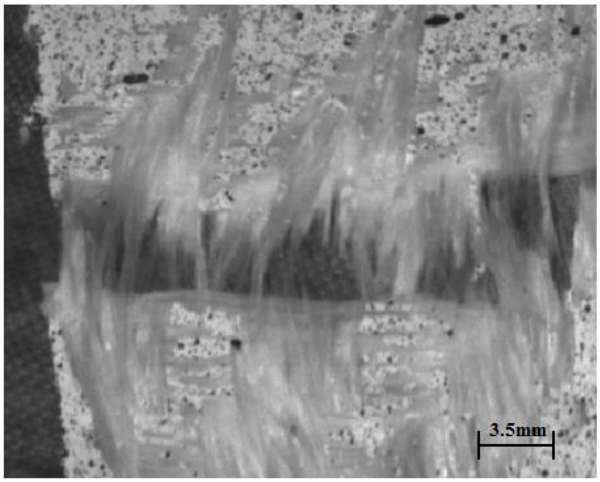

Figure 4.22 Failure of specimen F50 captured by the DIC system

4.4 EXPERIMENTAL RESULTS FOR [±45°] SPECIMENS

This section presents the detailed experimental results for the [±45°] specimens. Firstly, strain paths at failed regions are plotted for these specimens. This includes the strain paths that detail the evolution of principal strain and fibre strain. Then the failure envelopes for the [±45°] specimens are demonstrated, discussed and compared to the failure envelopes for the [0°/90°] specimens. Finally, the failure regions of the [±45°] specimens are examined in different groups based on the failure initiation region and the failure morphology.

As shown in Figure 4.23, the failure initiation regions for the [±45°] specimens vary based on the specimen geometry. Specimen O25, O100 and O200 failed at the pole region. Specimen O50 and O75 failed at the flange region and hence their failures were not captured by the strain measurement system. Failures in specimens O125 and O150 initiated in the mid region, where the strain information is still available. During the

experiment, specimen O25 exhibited large deformation and resulted in peeling of the paint. This phenomenon led to the loss of strain evolution during the final stages. Therefore, the strain paths plotted for the [±45°] specimens only include specimen O100, O125, O150 and O200.

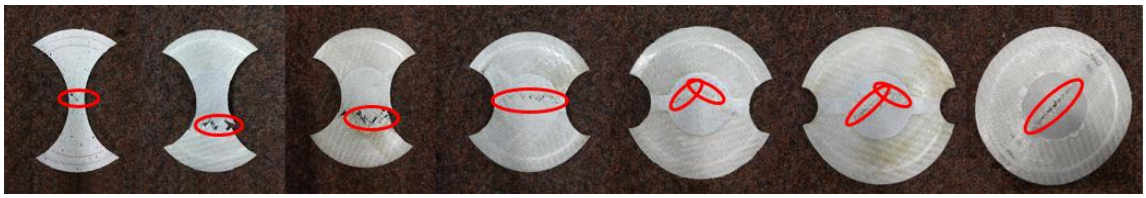

Figure 4.23 Failed [±45°] specimens with red circles marking the failed regions

4.4.1 Experimental results in the principal strain space

The evolution of strains in the principal strain space for the failed regions of the [±45°] specimens is shown in Figure 4.24. It is found that the major principal strain limits vary with the magnitude of the minor principal strain. This clearly demonstrates that the major principal strain limit is a function of the deformation mode. For specimens failed at the same region (pole or mid), the trend of the strain evolution is influenced by the sectional width of the specimens. Among the four [±45°] specimens, only the full circular specimen O200 has strain path in the positive minor strain region.

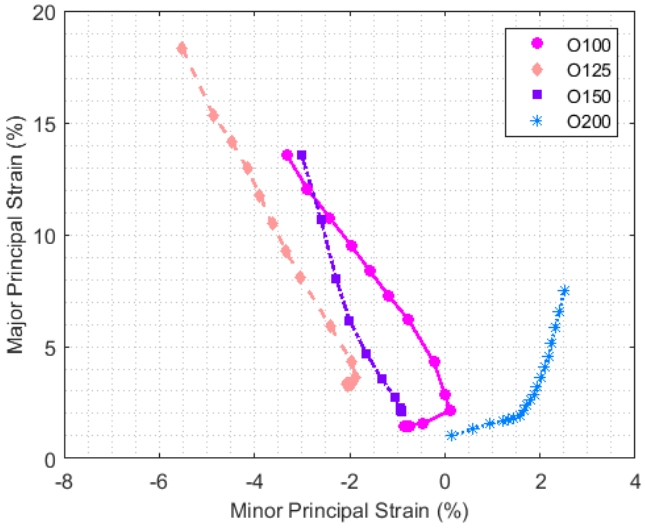

Figure 4.24 Principal strain paths for the [±45°] specimens at failed regions

The comparison of the strain paths of the [±45°] specimens and the [0°/90°] specimens is shown in Figure 4.25. The full circular specimen can be identified as either F200 or O200. From this comparison graph, it is found that the [±45°] specimens can induce failures in a more negative minor strain region, especially for the specimens that had failure in the mid region. It is also observed that the major principal limit reduces when the value of the minor principal strain becomes more positive.

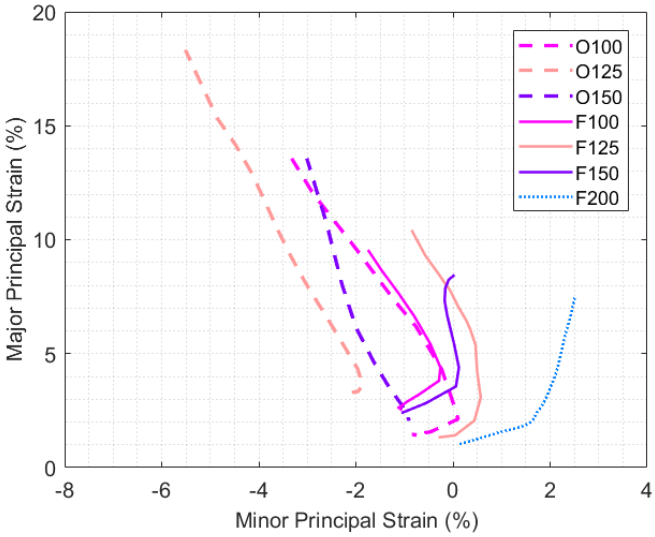

Figure 4.25 Comparison of [±45°] specimens and [0°/90°] specimens

The modified principal strain paths for the [±45°] specimens at failed regions are illustrated in Figure 4.26. It is found that failures initiated in the mid region have different strain paths from failures initiated in the pole region. Specimen O100 and O150 failed at similar strain ratios and also have similar failure limits in the major principal strain. However, they exhibited different strain paths during loading. This suggests that using major principal strain limit as a metric for failure may not account for path dependency effects.

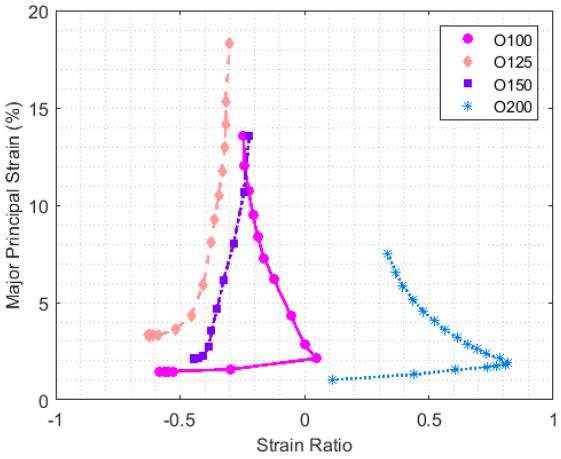

Figure 4.26 Modified strain paths for the [±45°] specimens at failed regions

The failure envelope in the principal strain space for the [±45°] specimens in the principal strain space is shown in Figure 4.27 (b). It is found that the failure limits in the major principal strain decrease with the minor principal strain becoming more positive. There is a large range of the major principal strain limits with the largest value at around 20% and the lowest value at only 8%.

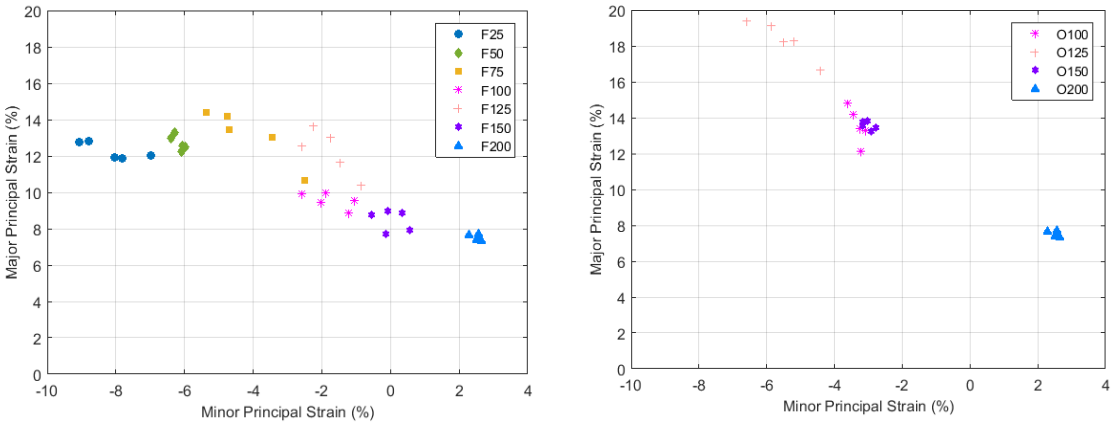

(a) (b)

Figure 4.27 The failure envelope in the principal strain space for (a) [0°/90°] specimens; (b) [±45°] specimens

Compared to the failure envelope in the principal strain space for the [0°/90°] specimens shown in Figure 4.27 (a), the failure envelope in the principal strain space for the [±45°] specimens covered a narrower range of deformation modes. This is due to the experimental difficulties in obtaining the strain evolution information for the narrow [±45°] specimens. A discrepancy between these two failure envelopes is observed. In the failure envelope for the [0°/90°] specimens, the major principal limit at minor principal strain around -6% is about 14%. However, in the failure envelope for the [±45°] specimens, the major principal limit at minor strain of -6% is nearly 20%. This indicates that the change of fibre orientation might influence the failure limits of the GFRP composite material in the principal strain metric.

The modified failure envelopes for the [0°/90°] specimens and for the [±45°] specimens are shown in Figure 4.28 (a) and (b). From the modified failure envelope for the [±45°] specimens, it is found that all the three hourglass specimens (O100, O125 and O150) failed at similar deformation mode of strain ratio between -0.4 to -0.2. Specimen O125 shows a higher major principal strain limit around 19% while specimen O100 and O150 both exhibit a lower major principal strain limit round 14%. The difference in the major principal strain limit between [0°/90°] and [±45°] sets of specimens is more noticeable.

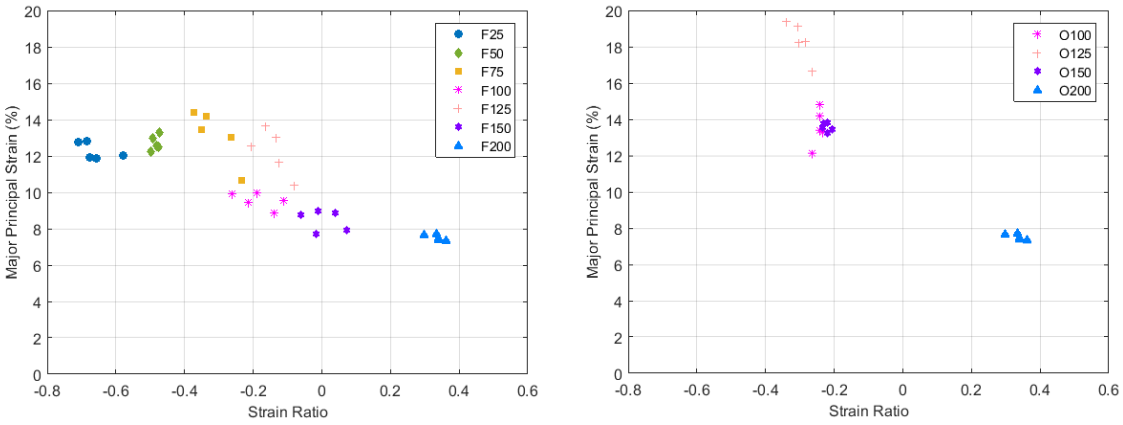

(a) (b)

Figure 4.28 Modified failure envelope for (a) [0°/90°] specimens; (b) [±45°] specimens

4.4.2 Experimental Results in the Fibre Strain Space

The evolution of fibre strains for the [±45°] specimens at failed regions is plotted in the Figure 4.29 (b). The corresponding modified strain path graph is shown in Figure 4.29 (a) for comparison. From the fibre strain path graph, it is found that the fibre strain of the three [±45°] hourglass shaped specimens (O100, O125 and O150) reached similar magnitudes and deformation modes, with similar or completely different strain paths. By comparing the modified principal strain graph and the fibre strain path graph, it is observed that the fibre strain paths have the same trend as the principal strain paths. In the modified principal strain path graph, the failure limits decrease with the increase of the strain ratio. In the fibre strain path graph, however, the fibre strain limits are similar at different strain ratios. The failure limit for the major principal strain varies from 8% to 18% for different deformation modes. This is nearly 100% in variation of the major strain limit. The fibre strain value varies from 7% to 8% and this is a narrow band of failure.

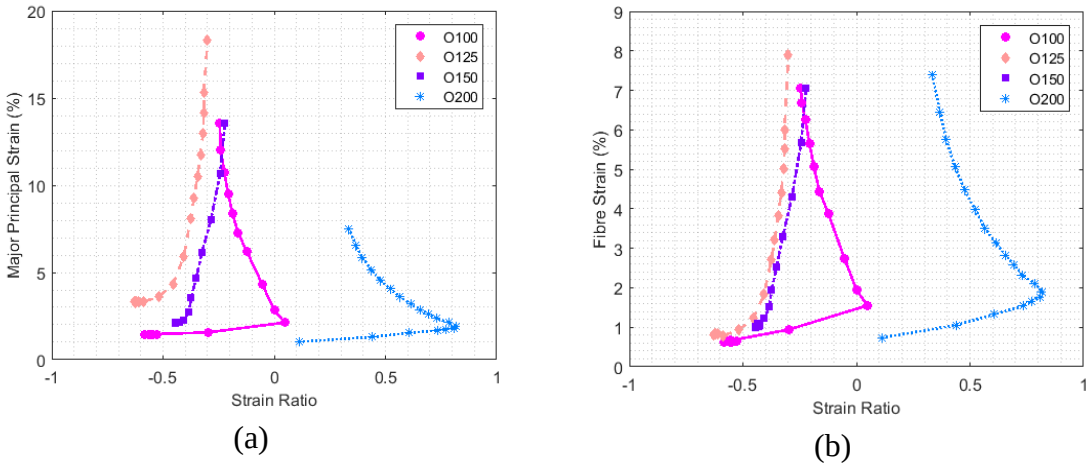

(a) (b)

Figure 4.29 Comparison of strain paths for the [±45°] specimens at failed regions (a) modified principal strain path;(b) fibre strain path

The fibre strain failure envelopes for the [0°/90°] specimens and for the [±45°] specimens are shown in Figure 4.30 (a) and (b). In the fibre strain failure envelopes, the failure limits are represented by the strain limits of the fibre bundle. The failure limits are plotted as a function of the deformation mode, which is represented by the strain ratio. For the [0°/90°] specimens, the fibre strain limits all fall between 6% and 8%. For the [±45°] specimens, although the fibre strain limits for specimen O125 is slightly higher, the failure limits in fibre strain are still around 6% to 8%. In the fibre strain failure envelope, the discrepancy between the failure limits for the specimens with different fibre orientations is almost eliminated. ***This observation strongly supports the hypothesis that fibre strain is a robust indicator for failures in the woven GFRP composite material, that is independent of the loading path and fibre orientation. These results are fundamental contributions in elucidating failure of woven thermoplastic GFRP materials.***

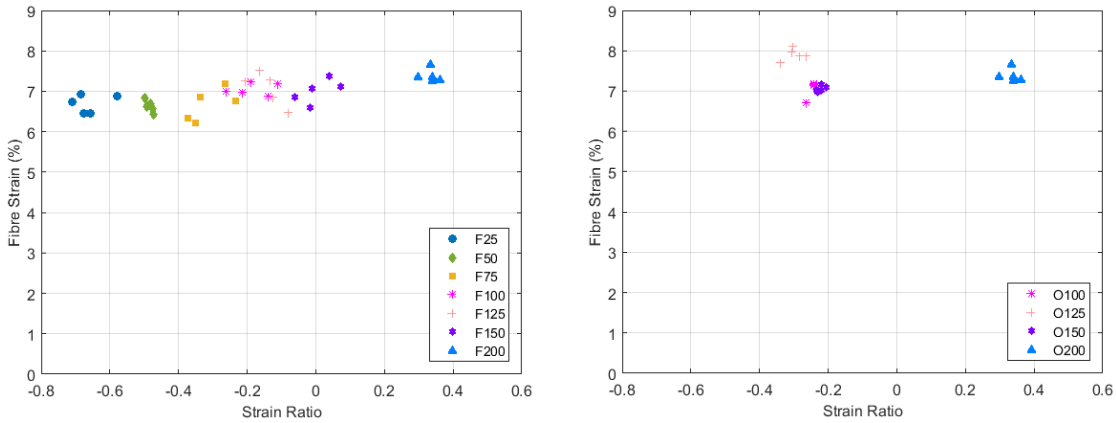

(a) (b)

Figure 4.30 Fibre strain failure envelope for (a) [0°/90°] specimens; (b) [±45°] specimens

4.4.3 Failure Examination

The discussion of the failures of the [±45°] specimens is based on three groups, as shown in Table 4.2. The failures of Group 1 specimens are recordable in the strain measurement system. Their strain paths and failure envelope are presented in the above sections. Group 2 specimens had failures occurring in the flange region and hence the strain evolution information at failure is not trackable. Group 3 has one specimen, O25. This specimen failed in the pole region, but the strain evolution information was lost due to the peeling of the paint.

Table 4.2 Groups of the [±45°] specimens based on the failure examination

Group Number	[±45°] Specimen(s)
1	O100, O125, O150, O200
2	O50, O75
3	O25

Although all the specimens in Group 1 have failures in the recordable area, the orientations of the failure zones are different. The failure of specimen O200 is shown in Figure 4.31. The major failure in this full circular specimen is fibre fracture in one fibre direction.

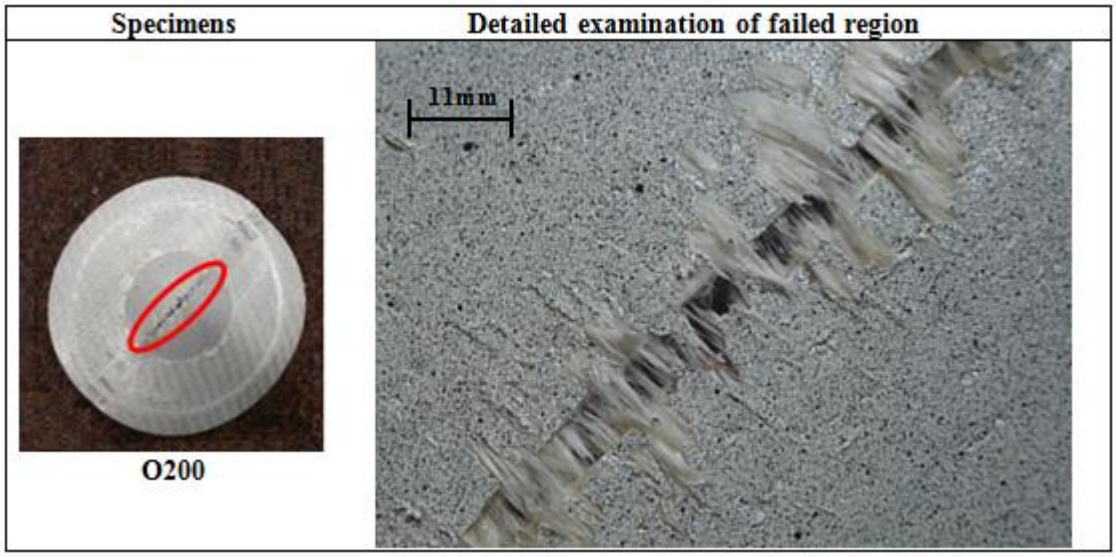

Figure 4.31 Detailed examination of the failed region for specimen O200

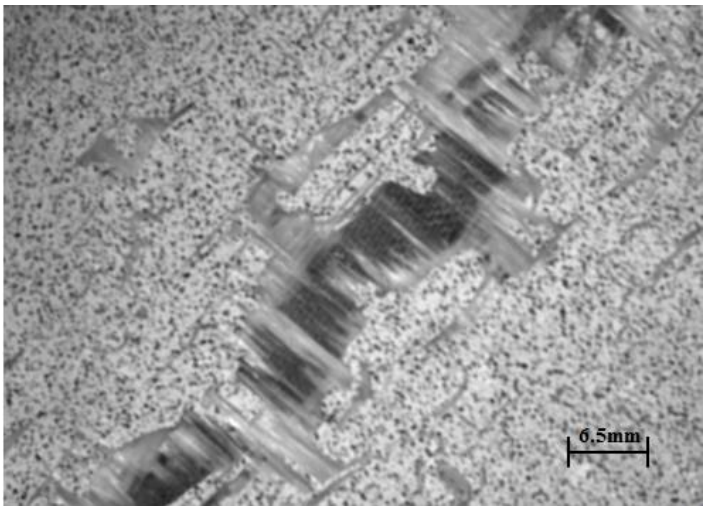

Figure 4.32 Failure of specimen O200 captured by the DIC system

The failure zone for the specimen O100 is shown in Figure 4.33. Although the fracture propagated horizontally, it is observed that the fracture is in a ‘zigzag’ type. Fibre fractures in both fibre directions are observed. This is a common fracture type in the [±45°] specimens. The failure image taken by the DIC system is shown in Figure 4.34. This image clearly demonstrates that fibre bundle failure is the dominating failure mechanism for the [±45°] specimens.

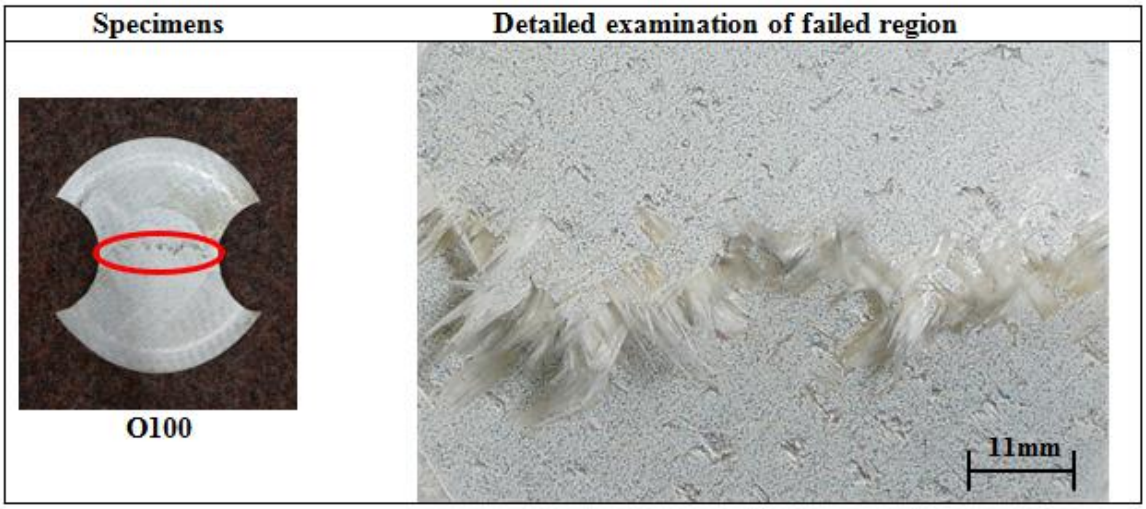

Figure 4.33 Detailed examination of the failed region for specimen O100

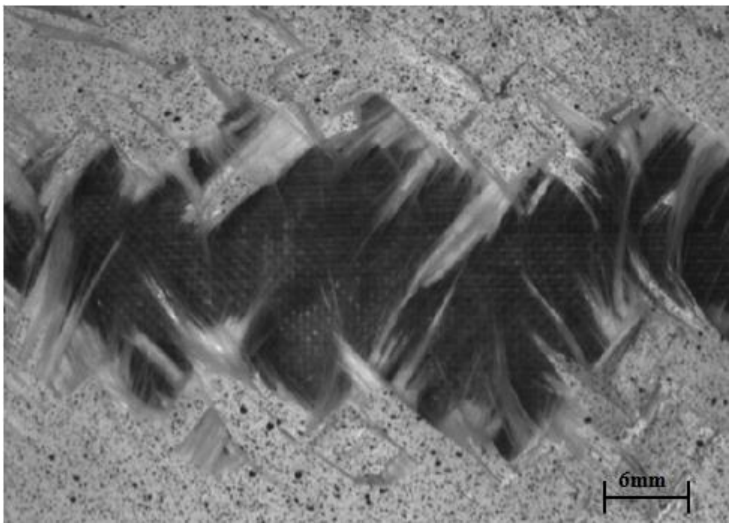

Figure 4.34 Failure of specimen O100 captured by the DIC system

In specimen O125 and O150, failure initiated in the mid region and the fracture propagated along both fibre directions. The detailed examination of the failed regions for these two specimens is shown in Figure 4.35. A large amount of fibre bundle fractures are observed in both fibre directions. A close examination of specimen O150 in Figure 4.36 clearly indicates that fibre bundle failure is the main failure mechanism.

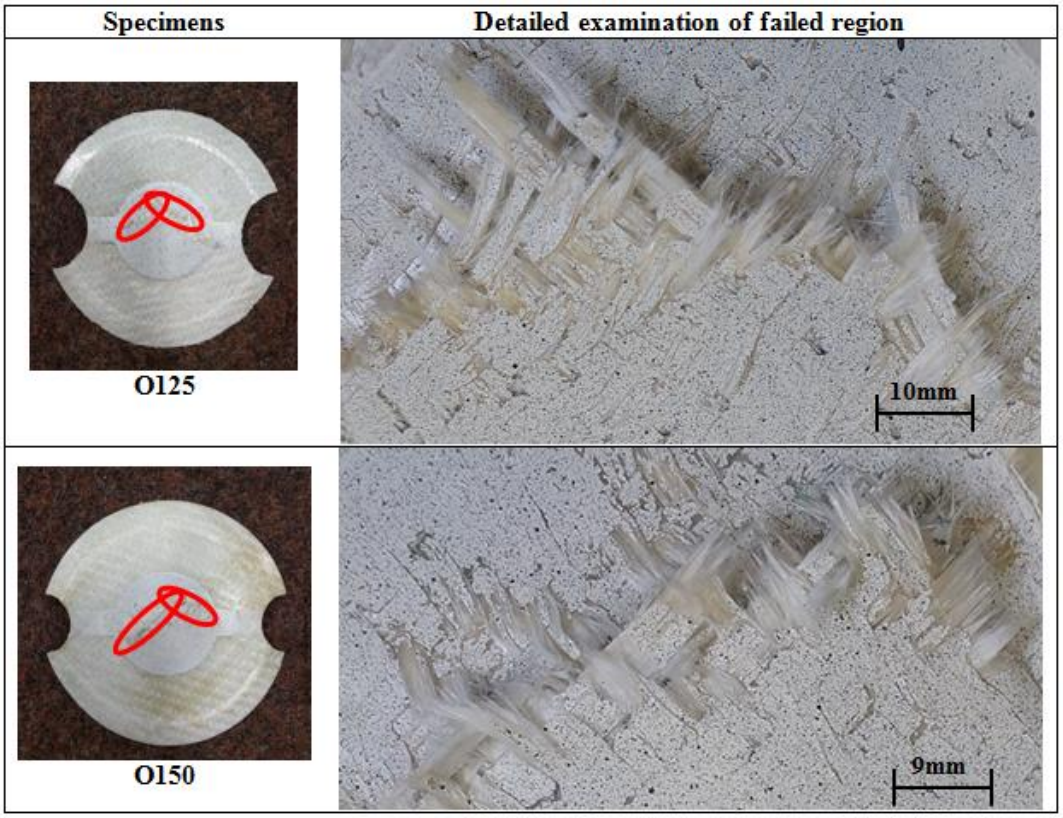

Figure 4.35 Detailed examination of the failed regions for specimen O125 and O150

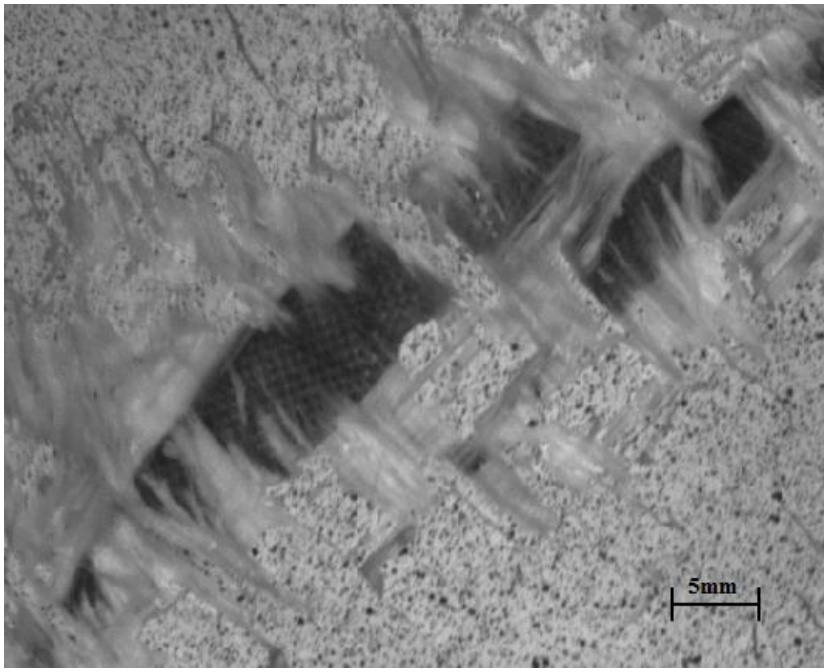

Figure 4.36 Failure of specimen O150 captured by the DIC system

The failures of Group 2 specimens are shown in Figure 4.37. Failures in these two specimens (O50 and O75) initiated at the flange region of one side of the specimen and propagated in a zigzag pattern. In these two specimens, fibre bundle fractures in both fibre directions are observed as well. In addition, small cracks at the crimps existed around the whole fracture region.

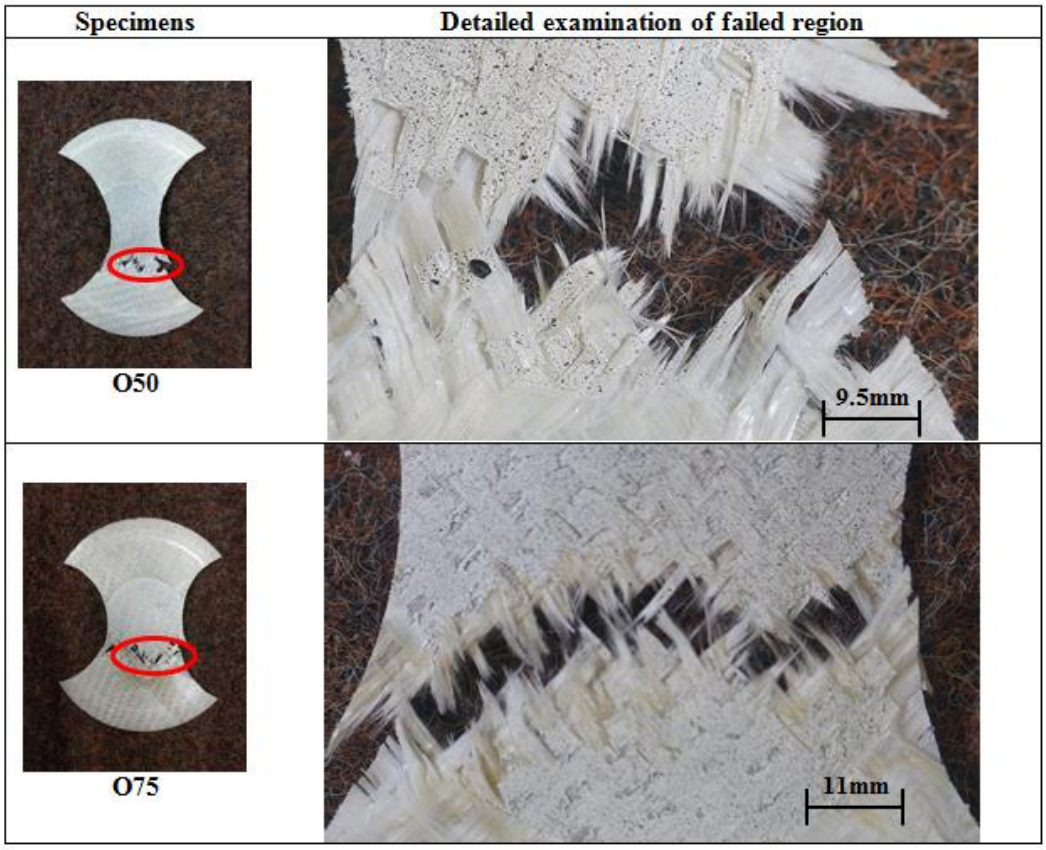

Figure 4.37 Detailed examination of the failed regions for specimen O50 and O75

Finally, the failure of the Group 3 specimen O25 is illustrated in Figure 4.38. The major failure mechanism is fracture of fibre bundles. In addition, it is found that large secondary cracks existed around the failure zone.

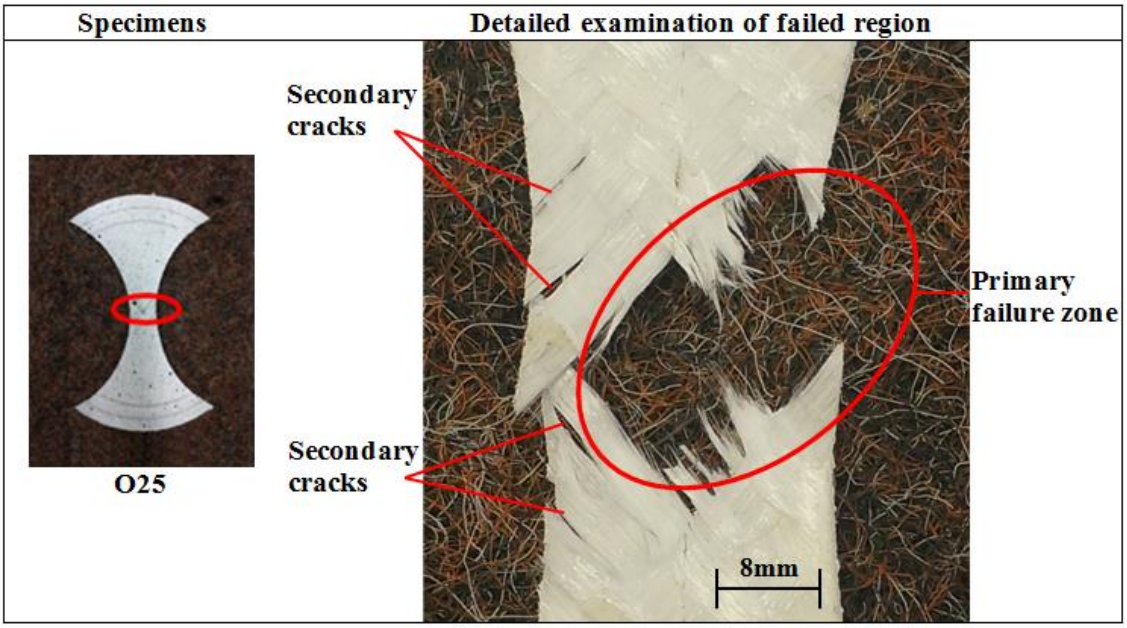

Figure 4.38 Detailed examination of the failed region for specimen O25

4.5 SIMULATION

The failure envelopes developed from the experimental results are implemented in the FEA models. Since the failure envelope developed from the [0°/90°] specimens cover a wider range of deformation modes, this envelope is used to predict failure in both [0°/90°] and [±45°] specimens in the simulation. The failure envelope is implemented in the simulation through the user-defined subroutine which also contains the material modelling. The failure envelope in the principal strain space and the fibre strain failure envelope are implemented separately. The predictions provided by both failure envelopes are compared in this section.

4.5.1 Implementation of Failure Envelope

The flow chart for the implementation of the failure envelopes in the FEA simulation is shown in Figure 4.39. The parameter ‘Flag’ indicates the status of an element. When flag equals to 0, the element is identified as safe. When the flag equals to 1, the element is considered as failed. At the start of the simulation, every element in the specimen is assigned with a flag value of 0. Then in each time increment, the incremental global strain information is obtained first and used for calculation of the strain ratio and fibre strain, which are the essential components in the failure envelope. With all the strain information, each element in the specimen is tested for failure. If this element already has a flag value of 1, it means this element is already failed and the flag value will remain at 1. If the flag equals to 0, it means this element is safe in the previous increments and it will be tested for failure. The strain status of this element will be compared with the failure envelope. If the strain of the element is below the failure envelope, this element is considered as safe. Otherwise, it is considered as failed. Corresponding values will be assigned to the flag of this element. After every element is checked in this increment, next increment will begin. When there is no next increment, the simulation is finished.

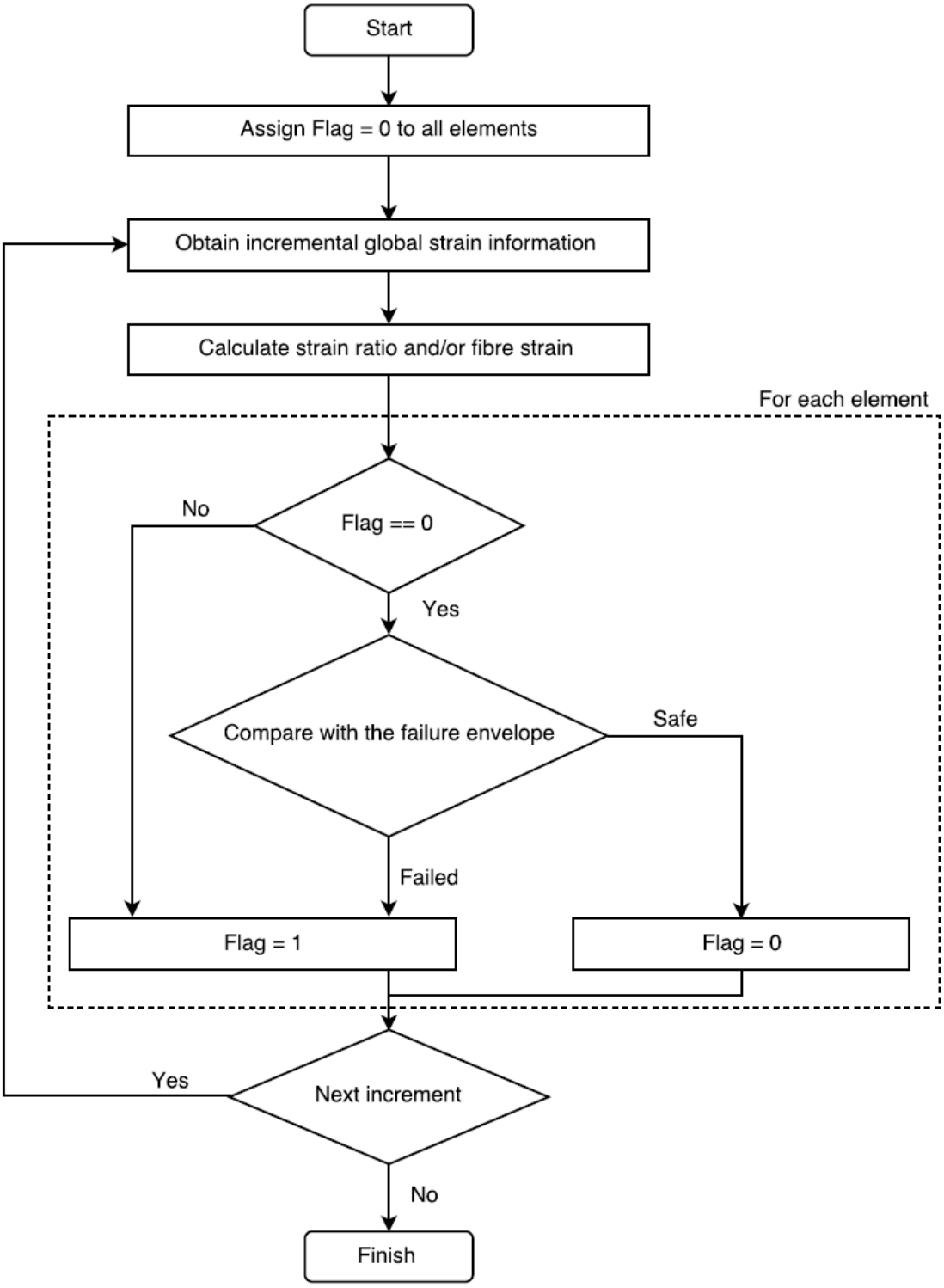

Figure 4.39 Flow chart of the implementation of failure envelope in the FEA model

4.5.2 Prediction Results

The failure predictions for the [0°/90°] specimens are shown in Figure 4.40. For narrow specimens F25 and F50, the failure envelope in the principal strain space predicts failure initiation in the mid region and to occur along the sides of the specimen. The fibre strain failure envelope predicts failure to initiate in the pole region. By comparing the simulation results with experimental results, the result indicates that the simulation incorporated with the fibre strain failure criteria gives better predictions of failure. For the other specimens (F75, F100, F125, F150 and F200), the simulation incorporated with the failure envelope in the principal strain space mainly predicts failures to occur in the mid region and some in the flange region as well (specimen F125 and F150). The simulation incorporated with the fibre strain failure envelope predicts failures to occur in the pole region for all of the [0°/90°] specimens. The experimental results agree with the predictions provided by the fibre strain envelope.

Specimen	Prediction by failure envelope in the principal strain space	Prediction by fibre strain failure envelope
 F25	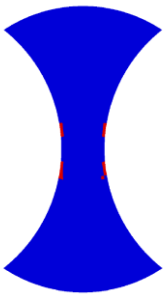	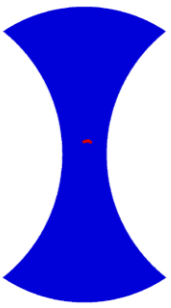

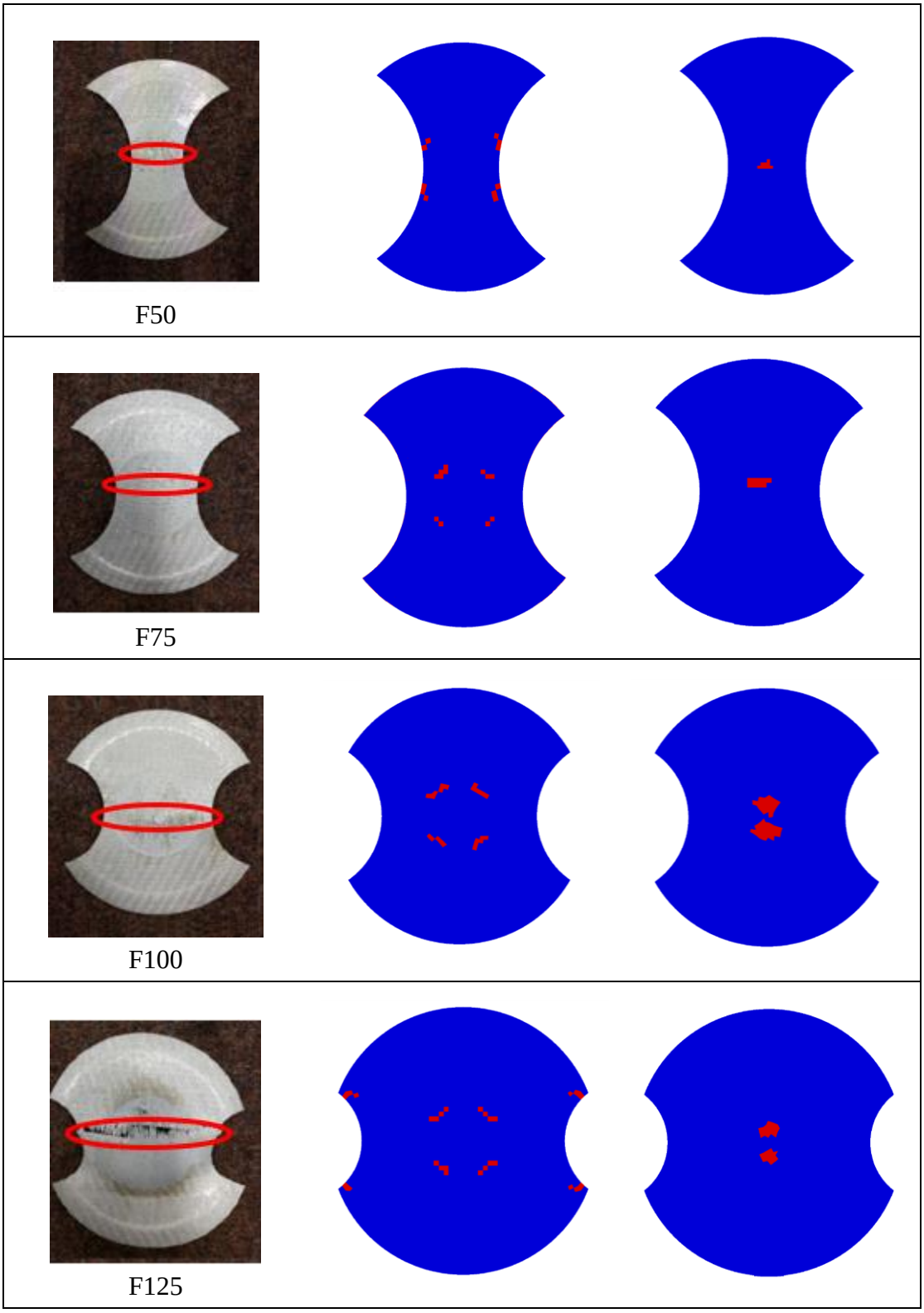
F50
F75
F100
F125

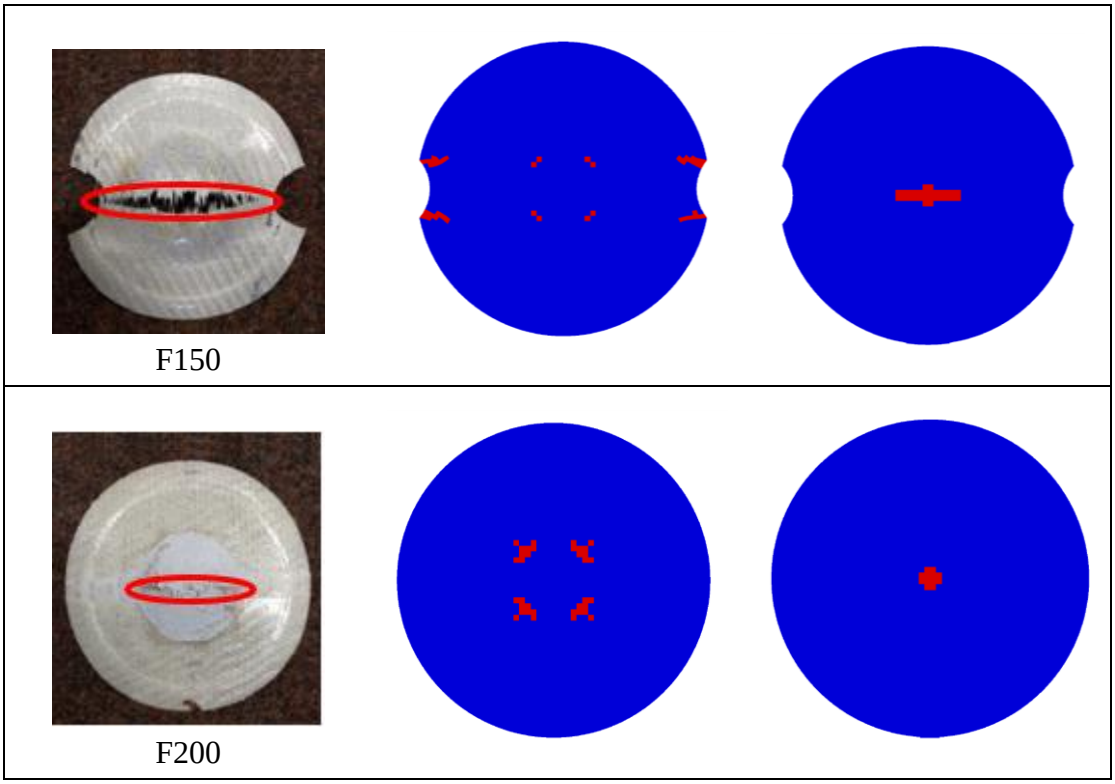

Figure 4.40 Prediction of failures for the [0°/90°] specimens

The failure predictions for the [±45°] specimens are shown in Figure 4.41. For specimen O25, both failure envelopes provide failure predictions in the pole region, in accordance with the experimental results. Specimen O50 and O75 both failed in the flange region. The simulation incorporated with the failure envelope in the principal strain space predicts failure to occur in the pole region for these two specimens. The simulation incorporated with the fibre strain failure envelope predicts failures to occur in the flange region for these two specimens. This matches with the experimental results. For specimen O100, the simulation incorporated with the failure envelope in the principal strain space predicts failure to occur in the mid region and the simulation incorporated with the fibre strain failure envelope predicts failure to occur in the pole region. The

experimental results are in accordance with the predictions provided by the simulation incorporated with the fibre strain failure envelope. For the two wide [±45°] specimens O125 and O150, failures occurred in the mid region and exhibited two oriented major cracks. The simulation incorporated with the failure envelope in the principal strain space can predict the failure initiation in the mid region, but the orientation of the failure zones was inaccurate. The simulation incorporated with the fibre strain failure envelope, on the other hand, is able to predict the location and orientation of the failure zones.

Specimen	Prediction by failure envelope in the principal strain space	Prediction by fibre strain failure envelope
 O25	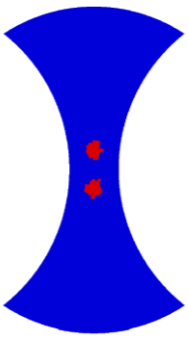	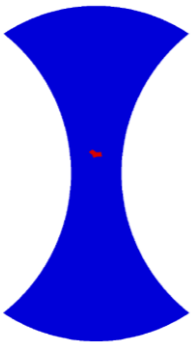
 O50	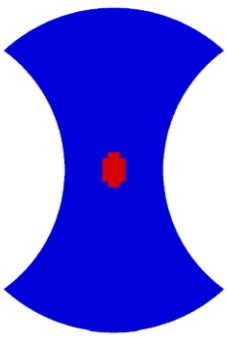	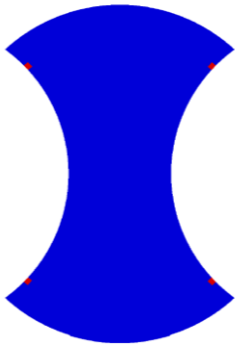

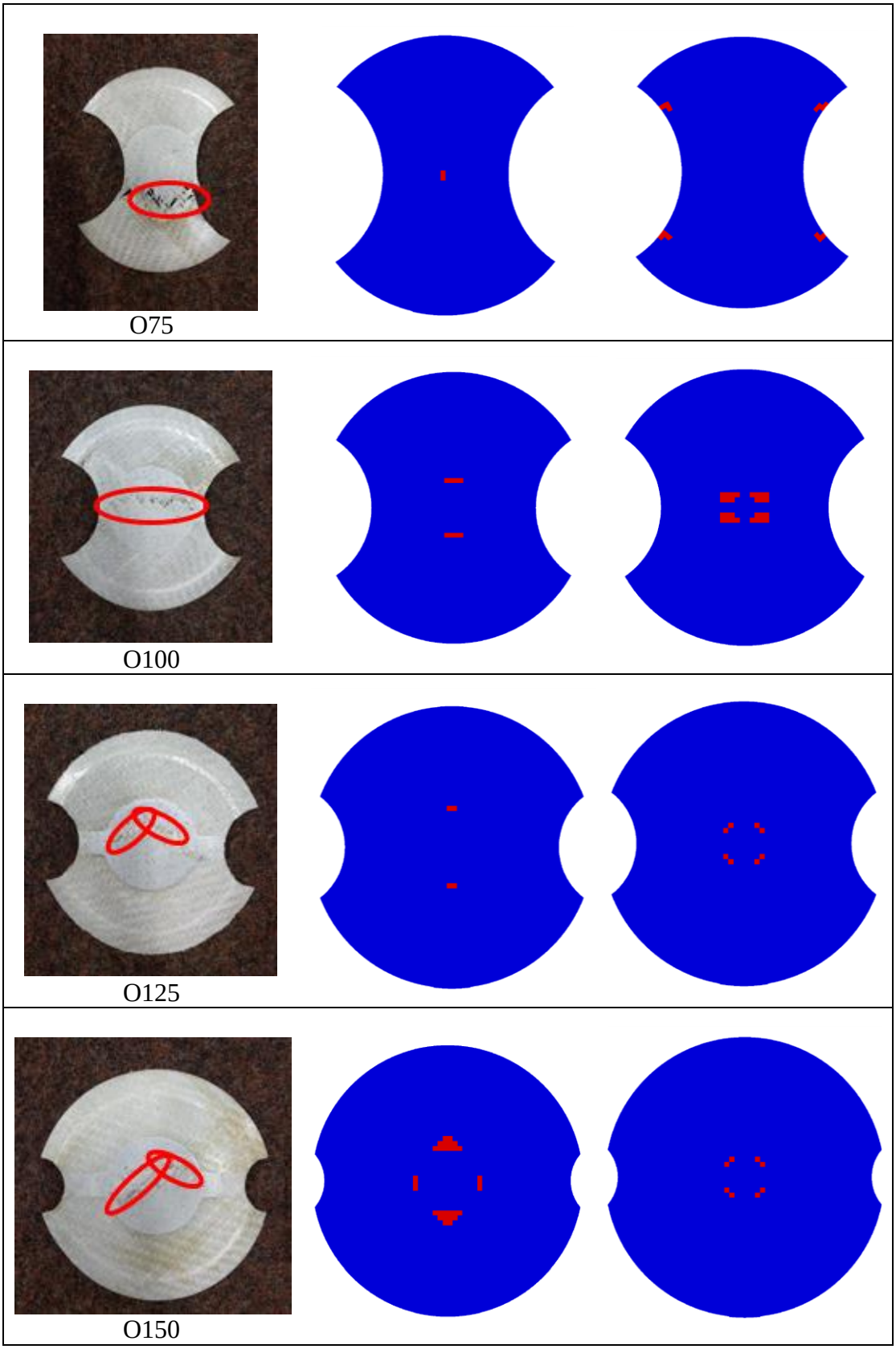

Figure 4.41 Prediction of failures for the [±45°] specimens

From the above discussions, it can be concluded that the simulation incorporated with the fibre strain failure envelope can give reasonable predictions for all the specimens employed in this study.

4.6 SUMMARY

This chapter discusses the experimental and simulation results for failure predictions of the GFRP composite material system. It was found that fibre fracture is the dominating failure mechanism for all the specimens studied. A novel failure metric tracking the evolution of strains along the fibre bundles has been proposed and found to be a robust indicator for failure of the GFRP composite material. The failure envelope in the principal strain space is found to be inaccurate in predicting failures in this material system. The failure envelopes developed from the experimental results are incorporated with the FEA simulations, to provide predictions of failures in the GFRP specimens. Compared to the failure envelope in the principal strain space, the simulation incorporated with the fibre strain failure envelope can provide predictions that have a better agreement with the experimental results.

Chapter 5 Conclusions and Future Work

5.1 CONCLUSIONS

The novel experimental approach in this study induced failures in a large range of deformation modes in the GFRP composite material system. The failure envelope based on the principal strains and the failure envelope based on the strains experienced by the fibre bundles are constructed from the experimental results. It is found that the failure envelope, which uses major principal strain as the failure metric, is path dependent and is influenced by the fibre orientation. The fibre strain failure envelope, which uses the fibre strain as the failure metric, on the other hand, is found to be independent of deformation modes and fibre orientations.

The morphology of the failures in the GFRP specimens is investigated and it is found that although the severity and region of failure vary from specimen to specimen, the dominant failure mode in all the specimens is fibre fracture.

Both failure envelopes are incorporated in the FEA simulations through the user-defined subroutine. Through this implementation, the failure predictions by the simulation incorporated with each failure envelope for different specimens can be obtained. These simulation results are compared with the experimental results. It is found that the simulation incorporated with the fibre strain failure envelope can provide reasonable predictions for all the specimens in this study. On the contrary, the predictions by the simulation incorporated with the failure envelope in the principal strain space agree with merely half of the experimental results. This suggests that the fibre strain failure theory

is more suitable for the woven thermoplastic fibre-reinforced composite, whose failure is dominated by fibre fracture.

5.2 FUTURE WORK

Although failures in a large range of deformation modes were induced by the novel experimental approach in this study, there are still deformation modes that are not covered, such as, the pure shear and equi-biaxial tension deformation modes. For the future work, it would be valuable to investigate the experimental approach to induce failures in a wider range of deformation modes. Different geometries of specimens and other fibre orientations can be considered in the experimental plan.

Temperature is an important parameter for thermoplastic composites. In this study, all the experiments were conducted under room temperature. For the future work, it would be useful to investigate the failure behaviour of the woven GFRP composite material for a range of temperatures.

The GFRP material system employed in this study is a single layer composite with fibres woven in 2/2 twill. For the future work, it would be meaningful to investigate the failure behaviour of composites with multiple layers and different woven patterns.

Bibliography

[1] E. Witten, T. Kraus, and M. Kühnel, "Composites Market Report 2014 -Market developments, trends, challenges and opportunities," 2014.

[2] Lucintel, "Growth Opportunities in the Global Thermoplastic Composites Market," 2016.

[3] M. S. Babu, S. Baksi, G. Srikant, and S. Biswas. (2009, Nov 11). *Thermoplastic Composites – A New Business Avenue* Available: http://tifac.org.in/index.php?option=com_content&view=article&id=533:thermoplastic-composites-a-new-business-avenue-&catid=85:publications&Itemid=952

[4] Quadrant Group. (2017, Nov 11). *Sports & Leisure*. Available: http://www.quadrantplastics.com/en/industries/sports-leisure.html

[5] Climate Change Authority. (2012, Nov 11). *Opportunities to reduce light vehicle emissions in Australia*. Available: http://www.climatechangeauthority.gov.au/reviews/light-vehicle-emissions-standards-australia/opportunities-reduce-light-vehicle-emissions

[6] Climate Change Authority. (2012, Nov 11). *Light vehicle emissions standards for Australia*. Available: http://climatechangeauthority.gov.au/reviews/light-vehicle-emissions-standards-australia

[7] Commonwealth of Australia. (2017, Nov 11). *Vehicle emissions*. Available: https://www.greenvehicleguide.gov.au/pages/Information/VehicleEmissions

[8] The Department of Infrastructure and Regional Development. (2017, Nov 11). *Vehicle Emission Standards*. Available: https://infrastructure.gov.au/roads/environment/emission/

[9] C. Red. (2014, Nov 11). *The Outlook for Thermoplastics in Aerospace Composites, 2014-2023*. Available: https://www.compositesworld.com/articles/the-outlook-for-thermoplastics-in-aerospace-composites-2014-2023

[10] G. Gardiner. (2009, Nov 11). *Thermoplastic composites: Inside story*. Available: https://www.compositesworld.com/articles/thermoplastic-composites-inside-story

[11] M. Golzar and M. P. Zeinolabedin, "Prototype fabrication of a composite automobile body based on integrated structure," *The International Journal of Advanced Manufacturing Technology,* vol. 49, pp. 1037-1045, 2010.

[12] B. Lu. (2010, Nov 11). *The Boeing 787 Dreamliner - Designing an Aircraft for the Future*. Available: http://www.jyi.org/issue/the-boeing-787-dreamliner-designing-an-aircraft-for-the-future/

[13] The Boeing Company. (2014). *A QUARTERLY PUBLICATION BROUGHT TO YOU BY THE BOEING EDGE*. Available: http://www.boeing.com/commercial/aeromagazine/articles/2014_q4/pdf/AERO_2014q4.pdf

[14] P. Brady and M. Brady, "Automotive composites: which way are we going?," *Journal of Reinforced Plastics*, vol. 51, pp. 32-35, 2007.

[15] R. Talreja and J. Varna, *Modeling Damage, Fatigue and Failure of Composite Materials*, 2015.

[16] J. Kies, "Maximum strains in the resin of fibreglass composites," 1962.

[17] B. Fiedler, M. Hojo, S. Ochiai, Schulte, K., and M. Ando, "Failure behavior of an epoxy matrix under different kinds of static loading," *Composites Science and Technology*, pp. 1615-1624, 2001.

[18] P. A, G. S, B. P, and V. J, "Interface debond crack growth in tension cyclic loading of single fiber polymer composites," *Composite Part A* pp. 86-94, 2013.

[19] E. Gamstedt and S. Andersen, "Fatigue degradation and failure of rotating composite structures - materials characterisation and underlying mechanisms," 2001.

[20] R. F. Gibson, *Principles of Composite Material Mechanics, Third Edition*: Taylor & Francis, 2011.

[21] S. W. Tsai and E. M. Wu, "A General Theory of Strength for Anisotropic Materials," *Journal of Composite Materials*, vol. 5, p. 58, 1971.

[22] Z. Hashin, "Failure Criteria for Unidirectional Fiber Composites," *Journal of Applied Mechanics*, vol. 47, pp. 329-334, 1980.

[23] Z. Hashin and A. Rotem, "A fatigue failure criterion for fiber reinforced materials," *Journal of Composite Materials*, vol. 7, pp. 448-464, 1973.

[24] R. B. Pipes and B. W. Cole, "On the off-axis strength test for anisotropic materials," *Journal of Composite Materials*, vol. 7, pp. 246-256, 1973.

[25] P. D. Soden, M. J. Hinton, and A. S. Kaddour, "A comparison of the predictive capabilities of current failure theories for composite laminates," *Composites Science and Technology*, vol. 58, pp. 1225-1254, 1998.

[26] M. J. Hinton, A. S. Kaddour, and P. D. Soden, "A comparison of the predictive capabilities of current failure theories for composite laminates, judged against

experimental evidence," *Composites Science and Technology,* vol. 62, pp. 1725-1797, 2002.

[27] M. J. Hinton, A. S. Kaddour, and P. D. Soden, *Failure criteria in fibre reinforced polymer composites: the world-wide failure exercise*: Elsevier, 2004.

[28] M. J. Hinton, A. S. Kaddour, and P. D. Soden, "Evaluation of failure prediction in composite laminates: background to 'part C' of the exercise," *Composites Science and Technology,* vol. 64, pp. 321-327, 2004.

[29] P. D. Soden, A. S. Kaddour, and M. J. Hinton, "Recommendations for designers and researchers resulting from the world-wide failure exercise," *Composites Science and Technology,* vol. 64, pp. 589-604, 2004.

[30] A. Kaddour and M. Hinton, "Benchmarking of triaxial failure criteria for composite laminates: comparison between models of 'Part (A)'of 'WWFE-II'," *Journal of Composite Materials,* vol. 46, pp. 2595-2634, 2012.

[31] A. S. Kaddour and M. J. Hinton, "Evaluation of theories for predicting failure in polymer composite laminates under 3-D states of stress: Part A of the second world-wide failure exercise " *Journal of Composite Materials (Special issue)* vol. 46, pp. 19-20, 2012.

[32] A. S. Kaddour and M. J. Hinton, "Maturity of 3D failure criteria for fibrereinforced composites: Comparison between theories and experiments: Part B of WWFE-II," *Journal of Composite Materials,* vol. 47, pp. 925-966, 2013.

[33] A. S. Kaddour, M. J. Hinton, P. Smith, and S. Li, "The background to the third world-wide failure exercise," *Journal of Composite Materials,* vol. 47, pp. 2417-2426, 2013.

[34] A. S. Kaddour, M. J. Hinton, P. Smith, and S. Li, "Mechanical properties and details of composite laminates for the test cases used in the third world-wide failure exercise," *Journal of Composite Materials,* vol. 47, pp. 2427-2442, 2013.

[35] A. S. Kaddour, M. J. Hinton, P. Smith, and S. Li, "A comparison between the predictive capability of matrix cracking, damage and failure criteria for fibre reinforced composite laminates: Part A of the third world-wide failure exercise," *Journal of Composite Materials,* vol. 47, pp. 2749-2779, 2013.

[36] A. S. Kaddour and M. J. Hinton, "Evaluation of theories for predicting failure in polymer composite laminates under 3-D states of stress: Part B of the second world-wide failure exercise " *Journal of Composite Materials (Special issue)* vol. 47, 2013.

[37] M. Hinton and A. Kaddour, "The background to Part B of the Second World-Wide Failure Exercise: Evaluation of theories for predicting failure in polymer composite laminates under three-dimensional states of stress," *Journal of Composite Materials,* vol. 47, pp. 643-652, 2013.

[38] A. S. Kaddour, M. J. Hinton, S. Li, and P. Smith, "The world-wide failure exercises: how can composites design and manufacture communities build their strength," presented at the 16th European Conference on Composite Materials, Seville, Spain, 2014.

[39] L. J. Hart-Smith, "Is there really no need to be able to predict matrix failures in fibre-polymer composite structures? Part 1: Explanation of fatal flaws in existing theories," *Australian Journal of Mechanical Engineering,* vol. 12, pp. 139-159, 2014.

[40] L. J. Hart-Smith, "Is there really no need to be able to predict matrix failures in fibre-polymer composite structures? Part 2: Examples of matrix failures preceding fibre failures," *Australian Journal of Mechanical Engineering,* vol. 12, pp. 160-178, 2014.

[41] S. W. Tsai and J. D. D. Melo, "An invariant-based theory of composites," *Composite Science and Technology,* vol. 100, pp. 237-243, 2014.

[42] E. J. Pineda and A. M. Waas, "Numerical implementation of a multiple-ISV thermodynamically-based work potential theory for modeling progressive damage and failure in fiber-reinforced laminates," *Int J Fract,* vol. 182, pp. 93-122, 2013.

[43] S. W. Tsai and J. D. D. Melo, "A unit circle failure criterion for carbon fiber reinforced polymer composites," *Composites Science and Technology,* vol. 123, pp. 71-78, 2016.

[44] L. Li, S. V. Lomov, and X. Yan, "Correlation of acoustic emission with optically observed damage in a glass/epoxy woven laminate under tensile loading," *Composite Structures* vol. 123, pp. 45-53, 2015.

[45] M. Kersani, S. V. Lomov, A. W. Van Vuure, A. Bouabdallah, and I. Verpoest, "Damage in flax/epoxy quasi unidirectional woven laminates under quasi-static tension," *Journal of Composite Materials,* vol. 49, pp. 403-413, 2015.

[46] N. De Greef, L. Gorbatikh, A. Godara, L. Mezzo, S. V. Lomov, and I. Verpoest, "The effect of carbon nanotubes on the damage development in carbon fiber/epoxy composites," *Carbon,* vol. 49, pp. 4650-4664, 2011.

[47] A. E. Bogdanovich, M. Karahan, S. V. Lomov, and I. Verpoest, "Quasi-static tensile behavior and progressive damage in carbon/epoxy composite reinforced with 3D non-crimp orthogonal woven fabric," *Mechanics of Materials* vol. 62, pp. 14-31, 2013.

[48] N. De Greef, L. Gorbatikh, S. V. Lomov, and I. Verpoest, "Damage development in woven carbon fiber/epoxy composites modified with carbon nanotubes under tension in the bias direction," *Composites Part A* vol. 42, pp. 1635-1644, 2011.

[49] S. V. Lomov, A. E. Bogdanovich, D. S. Ivanov, D. Mungalov, M. Karahan, and I. Verpoest, "A comparative study of tensile properties of non-crimp 3D orthogonal weave and multilayer plain weave E-glass composites. Part 1: materials, methods and principal results," *Composite Part A,* vol. 40, pp. 1134-1143, 2009.

[50] D. S. Ivanov, S. V. Lomov, A. E. Bogdanovich, M. Karahan, and I. Verpoest, "A comparative study of tensile properties of non-crimp 3D orthogonal weave and multi-layer plain weave E-glass composites. Part 2: Comprehensive experimental results," *Composite Part A: Applied Science and Manufacturing,* vol. 40, pp. 1144-1157, 2009.

[51] D. S. Ivanov, S. V. Lomov, F. Baudry, H. Xie, B. Van Den Broucke, and I. Verpoest, "Failure analysis of triaxial braided composite," *Composites Science and Technology* vol. 69, pp. 1372-1380, 2009.

[52] J. R. Lee, J. Molimard, A. Vautrin, and Y. Surrel, "Digital phase-shifting grating shearography for experimental analysis of fabric composites under tension," *Composite Part A,* vol. 35, pp. 849-859, 2004.

[53] S. V. Lomov, D. S. Ivanov, I. Verpoest, M. Zako, T. Kurashiki, H. Nakai, *et al.*, "Full field strain measurements for validation of meso-FE analysis of textile composites," *Composite Part A,* vol. 39, pp. 1218-1231, 2008.

[54] S. Daggumati, E. Voet, W. Van Paepegem, J. Degrieck, J. Xu, S. V. Lomov, *et al.*, "Local strain in a 5-harness satin weave composite under static tension: part I - experimental analysis," *Composites Science and Technology* vol. 71, pp. 1171-1179, 2011.

[55] V. Koissin, J. Kustermans, S. V. Lomov, I. Verpoest, B. Van Den Broucke, and V. Witzel, "Structurally stitched NCF preforms: quasi-static response," *Composites Science and Technology* vol. 69, pp. 2701-2710, 2009.

[56] G. M. Newaz, *Advances in thermoplastic matrix composite materials* vol. 1044: ASTM International, 1989.

[57] O. Olabisi and k. adewale, *Handbook of thermoplastics* 2ed. vol. 41: CRC Press, 2016.

[58] Y. Ma, Y. Yang, T. Sugahara, and H. Hamada, "A study on the failure behavior and mechanical properties of unidirectional fiber reinforced thermosetting and thermoplastic composites," *Composites Part B: Engineering,* vol. 99, pp. 162-172, 2016.

[59] W. Albouy and B. Vieille, "Determination of the damage threshold in woven-ply thermoplastic laminates at T> Tg: Acoustic emission and microscopic damage analysis," *Composites Part B: Engineering,* vol. 64, pp. 138-146, 2014.

[60] M. Hou and K. Friedrich, "3-D stamp forming of thermoplastic matrix composites," *Applied Composite Materials,* vol. 1, pp. 135-153, 1994.

[61] J. H. Lee, J. H. Vogel, and K. Y. Rhee, "An analysis of stretch forming of thermoplastic composites," *Polymer Composites,* vol. 23, pp. 442-453, 2002.

[62] N. A. Zanjani, W. Wang, and S. Kalyanasundaram, "The effect of fiber orientation on the formability and failure behavior of a woven self-reinforced composite," *Journal of Manufacturing Science and Engineering,* vol. 137, p. 051012, 2015.

[63] N. A. Zanjani and S. Kalyanasundaram, "A comparison between forming behaviours of two pre-consolidated woven thermoplastic composites," *Journal of Materials Science and Chemical Engineering,* vol. 3, p. 180, 2015.

[64] M. A. Kabir, M. M. Huque, M. R. Islam, and A. K. Bledzki, "MECHANICAL PROPERTIES OF JUTE FIBER REINFORCED POLYPROPYLENE COMPOSITE; EFFECT OF CHEMICAL TREATMENT BY BENZENEDIAZONIUM SALT IN ALKALINE MEDIUM," *BioResources,* vol. 5, pp. 1618-1625, 2010.

[65] W. Wang, A. Lowe, and S. Kalyanasundaram, "Effect of chemical treatments on flax fibre reinforced polypropylene composites on tensile and dome forming behaviour," *International Journal of Molecular Sciences,* vol. 16, pp. 6202-6216, 2015.

[66] W. Hufenbach, M. Gude, R. Böhm, and M. Zscheyge, "The effect of temperature on mechanical properties and failure behaviour of hybrid yarn textile-reinforced thermoplastics," *Materials & Design,* vol. 32, pp. 4278-4288, 2011.

[67] A. Izer, A. Stocchi, T. Bárány, V. Pettarin, C. Bernal, and T. Czigány, "Effect of the consolidation degree on the fracture and failure behavior of self‐reinforced polypropylene composites as assessed by acoustic emission," *Polymer Engineering & Science,* vol. 50, pp. 2106-2113, 2010.

[68] W. Hufenbach, M. Gude, R. Böhm, and M. Thieme, "Failure behaviour of textile reinforced thermoplastic composites made of hybrid yarns-I: Probabilistically based damage models," presented at the ICF 12, Ottawa, 2009.

[69] W. Hufenbach, M. Gude, M. Thieme, and R. Böhm, "Failure behaviour of textile reinforced thermoplastic composites made of hybrid yarns-II: Experimental and numerical studies," presented at the ICF12, Ottawa, 2009.

[70] R. Böhm and W. Hufenbach, "Experimentally based strategy for damage analysis of textile-reinforced composites under static loading," *Composite Science and Technology,* vol. 70, pp. 1330-1337, 2010.

[71] J. P. BÖHLER, "Failure criteria for glass-fibre reinforced composites under confining pressure," *Journal of Structural Mechanics*, vol. 13, pp. 371-378, 1985.

[72] R. Böhm, M. Gude, and W. Hufenbach, "A phenomenologically based damage model for textile composites with crimped reinforcement," *Composites Science and Technology*, vol. 70, pp. 81-87, 2010.

[73] S. Baste and B. Audoin, "On internal variables in anisotropic damage," *European journal of mechanics. A. Solids*, vol. 10, pp. 587-606, 1991.

[74] R. G. Cuntze, "Strength failure conditions of the various structural materials: is there some common basis existing," *SDHM*, vol. 74, pp. 1-19, 2008.

[75] N. A. Zanjani, A. Sexton, and S. Kalyanasundaram, "Induced forming modes in a pre-consolidated woven polypropylene composite during stretch forming process at room temperature: I. Experimental studies," *Composites Part A: Applied Science and Manufacturing*, vol. 68, pp. 251-263, 2015.

[76] W. Wang, A. Lowe, S. Davey, N. A. Zanjani, and S. Kalyanasundaram, "Establishing a new Forming Limit Curve for a flax fibre reinforced polypropylene composite through stretch forming experiments," *Composites Part A: Applied Science and Manufacturing*, vol. 77, pp. 114-123, 2015.

[77] W. Wang, A. Lowe, and S. Kalyanasundaram, "Investigating the forming limits of a flax fibre-reinforced polypropylene composite in different water treatment conditions," *The International Journal of Advanced Manufacturing Technology*, vol. 87, pp. 103-113, 2016.

[78] Owens Corning. (n.d.). *Twintex® Co-Mingled Glass and Thermoplastic Reinforcements*. Available: http://www.composites.owenscorning.com/pdf/rft-guide/Composite_Solutions_Guide_page15.pdf

[79] J. Karger-Kocsis, *Polypropylene structure, blends and composites: Volume 3 composites*: Springer Science & Business Media, 2012.

[80] C. Stern, *On the performance of polypropylene: between synthesis and end-use properties*: University of Twente, 2005.

[81] L. MatWeb. Overview of materials for Polypropylene [Online]. Available: http://www.matweb.com/search/DataSheet.aspx?MatGUID=0b9e41983fd54215971bcaabb7111300&ckck=1

[82] Creative Mechanisms. (2016, Nov 12). *Everything You Need To Know About Polypropylene (PP) Plastic*. Available: https://www.creativemechanisms.com/blog/all-about-polypropylene-pp-plastic

[83] Owens Corning, "TWINTEX® T PP - PP Glass Fabrics," ed, 2008.

[84] B. Choi, O. Diestel, and O. P., "Commingled CF/PEEK hybrid yarns for use in textile reinforced high performance rotors," in *12th International conference on composite materials (ICCM)*, Paris, 1999, pp. 796-806.

[85] N. Cabrera, "Recyclable all-polypropylene composites: Concept, properties and manufacturing," PhD, Technische Universiteit Eindhoven, 2004.

[86] ACP Composites. (2011). *Weave Patterns*. Available: https://commercecontent.azureedge.net/0012-content/Weave-Patterns.pdf

[87] NetComposites Ltd. (2008, Nov 12). *Twintex Chosen for Vacuum Bag Moulded Thermoplastic Composite Canoe*. Available: https://netcomposites.com/news/2008/april/8/twintex-chosen-for-vacuum-bag-moulded-thermoplastic-composite-canoe/

[88] J. Gresham, "Influence of temperature on the stamp forming of fibre-metal laminate systems," Master of Philosophy, Australian National University, 2006.

[89] GOM Optical Measuring Techniques, "Aramis v5.4.1 user manual," ed: GOM mbH, 2005.

[90] GOM Optical Measuring Techniques, "Aramis v6. 1 user manual," ed: GOM mbH, 2009.

[91] Hibbitt, Karlsson, and Sorensen. ABAQUS: Theory Manual [Online].

[92] T. J. R. Hughes, "The Finite Element Method -- Linear Static and Dynamic Finite Element Analysis," Prentice-Hall, Englewood Cliffs1987.

[93] H. M. Hilber and T. J. R. Hughes, "Collocation, dissipation and 'overshoot' for time integration schemes in structural dynamics," *Earthquake Eng. Struct. Dyn.* , vol. 6, pp. 99-117, 1978.

[94] J. S. Sun, K. H. Lee, and H. P. Lee, "Comparison of implicit and explicit finite element methods for dynamic problems," *Journal of Materials Processing Technology*, vol. 105, pp. 110-118, 1999.

[95] M. Mashayekhi. (n.d.). *Comparison of implicit and explicit procedures* [PowerPoint slides]. Available: http://mashayekhi.iut.ac.ir/sites/mashayekhi.iut.ac.ir/files//u32/presentation4.pdf

[96] Hibbitt, Karlsson, and Sorensen, *ABAQUS/standard User's Manual* vol. 1: Hibbitt, Karlsson & Sorensen, 2001.

[97] iMechanica. (n.d.). *ABAQUS Elements* [PowerPoint slides]. Available: http://imechanica.org/files/l2-elements.pdf

[98] S. K. Paul, G. Manikandan, and R. K. Verma, "Prediction of entire forming limit diagram from simple tensile material properties," *The Journal of Strain Analysis for Engineering Design*, vol. 48, pp. 386-394, 2013.

[99] W. Wang, "Forming Analysis of Natural Fibre Composites," Doctor of Philosophy, Australian National University, 2015.

Appendix A

```
*USER SUBROUTINE
      SUBROUTINE UMAT(STRESS,STATEV,DDSDDE,SSE,SPD,SCD,
     1 RPL,DDSDDT,DRPLDE,DRPLDT,
     2 STRAN,DSTRAN,TIME,DTIME,TEMP,DTEMP,PREDEF,DPRED,CMNAME,
     3 NDI,NSHR,NTENS,NSTATV,PROPS,NPROPS,COORDS,DROT,PNEWDT,
     4 CELENT,DFGRD0,DFGRD1,NOEL,NPT,LAYER,KSPT,KSTEP,KINC)

      INCLUDE 'ABA_PARAM.INC'

      CHARACTER*80 CMNAME
      DIMENSION STRESS(NTENS),STATEV(NSTATV),
     1 DDSDDE(NTENS,NTENS),DDSDDT(NTENS),DRPLDE(NTENS),
     2 STRAN(NTENS),DSTRAN(NTENS),TIME(2),PREDEF(1),DPRED(1),
     3 PROPS(NPROPS),COORDS(3),DROT(3,3),DFGRD0(3,3),DFGRD1(3,3),
     4 D(3,3), DF(3,3), DE1(3,3), DE2(3,3)

      real*8  E1, E1F, E2, E2F, XU12, XU21, XU12F, XU21F, G, GF

     ------------------------------------------------------------


    MATERIAL PROPERTIES

   MATERIAL PROPERTIES AT START AND END OF INCREMENT


         XU12 = 0.45


         XU21 = 0.45


  stran (3) use /2 value so 28.35 should be sth divided by 2


          EF=FAILURE MA=MAJOR MI=MINOR FG=FLAG SR=STRAIN RATIO
FS=FIBRE STRAIN
     EPX=EPSILONX EPY=EPSILONY DEX=DELTA EPX DEY=DELTA EPY

      EF=STATEV(1)
      MA=STATEV(2)
```

```
      MI=STATEV(3)
      FG=STATEV(4)
      SR=STATEV(5)
      FS=STATEV(8)


      STATEV(2)=(STRAN(1)+DSTRAN(1)+STRAN(2)+DSTRAN(2))/2+SQRT((
     1     (STRAN(1)-STRAN(2)+DSTRAN(1)-DSTRAN(2))/2)**2+((STRAN(3)
     2   +DSTRAN(3))/2)**2)

      STATEV(3)=(STRAN(1)+DSTRAN(1)+STRAN(2)+DSTRAN(2))/2-SQRT((
     1   (STRAN(1)-STRAN(2)+DSTRAN(1)-DSTRAN(2))/2)**2+((STRAN(3)
     2   +DSTRAN(3))/2)**2)


      IF(STATEV(2).NE.0) THEN
      SR=STATEV(3)/STATEV(2)
      ELSE
      SR=0
      END IF

      STATEV(5)=SR

      SHEAR=-(DSTRAN(1)-DSTRAN(2))*SIN(2*ANGLE)+DSTRAN(3)/2*
     1      COS(2*ANGLE)

      ANGLE=ANGLE+SHEAR

      DEX=(DSTRAN(1)+DSTRAN(2))/2+(DSTRAN(1)-DSTRAN(2))
     1      /2*COS(2*ANGLE)+DSTRAN(3)/2*SIN(2*ANGLE)

            EPX=STATEV(6)+DEX
            STATEV(6)=EPX

      DEY=(DSTRAN(1)+DSTRAN(2))/2-(DSTRAN(1)-DSTRAN(2))
     1      /2*COS(2*ANGLE)+DSTRAN(3)/2*SIN(2*ANGLE)

            EPY=STATEV(7)+DEY
            STATEV(7)=EPY


      FS=MAX(EPX,EPY)
      STATEV(8)=FS
```

STRESS/STRAIN RELATIONS

E1= 7866

E2= 7866

STRESS/STRAIN RELATIONS

SHEAR MODULUS

G = (117.8 + 328.7 * EXP (-28.35*ABS(STRAN(3))))

DETERMINE LAMINAR STIFFNESS AND STRESS

D(1,1) = E1/(1 - XU12 * XU21)
D(1,2) = (E1 * XU21)/(1 - XU12 * XU21)
D(1,3) = 0.0D0
D(2,1) = (E2 * XU12)/(1 - XU12 * XU21)
D(2,2) = E2/(1 - XU12 * XU21)
D(2,3) = 0.0D0
D(3,1) = 0.0D0
D(3,2) = 0.0D0
D(3,3) = G

JACOBIAN DEFINITION

DDSDDE(1,1) = D(1,1)
DDSDDE(2,2) = D(2,2)
DDSDDE(1,2) = D(1,2)
DDSDDE(2,1) = D(2,1)
DDSDDE(3,3) = D(3,3)
DDSDDE(1,3) = 0
DDSDDE(2,3) = 0
DDSDDE(3,1) = 0
DDSDDE(3,2) = 0

UPDATE STRESS

```
DO K1 = 1,NTENS
   DO K2 = 1,NTENS
STRESS(K2) = STRESS(K2) + (D(K2,K1)* DSTRAN(K1))
   END DO
END DO



RETURN
END
```